Rapid and Reliable Quantitative MRI of Central Nervous System (CNS) at Ultra-High Field MRI (7T)

by

Seyedeh Nasim Adnani

A dissertation submitted to the Graduate Faculty of
Auburn University
in partial fulfillment of the
requirements for the Degree of
Doctor of Philosophy

Auburn, Alabama
August 9, 2025

Keywords: quantitative MRI, brain, spinal cord
ultra-high field

Approved by

Adil Bashir, Chair, Professor of Electrical and Computer Engineering
Thomas S. Denney Jr., Professor of Electrical and Computer Engineering
Shiwen Mao, Professor of Electrical and Computer Engineering
Meredith Reid, Assistant Professor of Electrical and Computer Engineering
Michael Roberts, Professor of Kinesiology

Abstract

Quantitative Magnetic Resonance Imaging (qMRI) surpasses traditional MRI, which primarily focuses on local image contrast. It reveals specific physical parameters related to the nuclear spin of protons in water and macromolecules. Parameters from qMRI, including longitudinal and transverse relaxation rates, magnetic susceptibility, proton density, and magnetization transfer, provide key insights into myelination, iron content, and cell membranes in the living central nervous system (CNS). qMRI has identified crucial, highly sensitive biomarkers in both health and disease, continually aiding longitudinal clinical trials as a non-invasive means to monitor changes in tissue. It offers insights into disease mechanisms that may precede visible changes in anatomical or structural images. Given the complementary nature of qMRI methods- such as T2* relaxometry, myelin imaging, magnetization transfer, and quantitative susceptibility mapping- to traditional contrast-weighted MRI, developing and implementing reliable acquisition and processing qMRI methods tailored to ultra-high field (7T) MR settings is vital for reliably assessing biophysical measures within a clinically feasible timeframe.

The specific goals of this work were: (i) to implement a protocol to accurately quantify T2*, QSM, qMT and MWF in-vivo at 7T ; (ii) to assess the reproducibility of the quantified values using scan-rescan experiments; (iii) to develop a robust technique for fast imaging of the human CNS; and (iv) to use the developed custom sequence to quantify myelin content with an increased acquisition speed by Compressed Sensing (CS). The primary aim of this work is to develop time-efficient, innovative, and non-invasive techniques capable of delivering quantitative insights into pathology, assisting in the monitoring of disease progression, and evaluating treatment effectiveness.

Acknowledgments

I would like to extend my sincerest gratitude to my advisor, Dr. Adil Bashir, for his unwavering guidance and support. This journey would not have been as meaningful without his supervision. I would also like to express my deep appreciation to the other committee members —Dr. Tom Denney, Dr. Shiwen Mao, Dr. Meredith Reid, and Dr. Michael Roberts — for their invaluable support and insightful recommendations. I am profoundly grateful to Dr. Ron Beyers and Ms. Julie Rodiek for their assistance throughout this remarkable experience. Last but not least, this dissertation is dedicated to my father, Seyed Esmaeil, who may no longer be with me, but remains in my heart and with me in every step I take. His love and his belief in me shaped who I am, and I hope this work makes him proud.

Table of Contents

List of Tables

List of Figures

List of Abbreviations

CS	Compressed Sensing
CSF	Cerebrospinal Fluid
FOV	Field of View
GM	Gray Matter
GRE	Gradient Recalled Echo
IRB	Institutional Review Board
MRI	Magnetic Resonance Imaging
MRS	Magnetic Resonance Spectroscopy
MRSI	Magnetic Resonance Spectroscopic Imaging
MT	Magnetization Transfer
MTR	Magnetization Transfer Ratio
MWF	Myelin Water Fraction
PSR	Pool Size Ratio
QSM	Quantitative Susceptibility Mapping
SNR	Signal to Noise Ratio
SoS	Stack-of-Stars
VSF	Voxel Spread Function
WM	White Matter
qMRI	Quantitative Magnetic Resonance Imaging

Chapter 1: Introduction

Conventional magnetic resonance imaging (MRI) offers critical insights essential for diagnosing, prognosis, and monitoring therapeutic efficacy in patients with underlying neurodegenerative disease [1, 2]. The designation' conventional MRI' refers to the methodologies employed in clinical practice to characterize pathological conditions based on contrasting changes observed in weighted images. These imaging modalities primarily, but not exclusively, demonstrate a biophysical contrast mechanism, such as T1- and T2-weighted scans [3] . The diagnostic utility of conventional magnetic resonance imaging (MRI) in numerous neurological disorders is indisputable; however, the scope of traditional MRI is confined to the identification of either prominent morphological abnormalities or localized irregularities, leading to regional variations in signal intensities within any given tissue [4]. Traditional MRI operates based on the differences in contrast between affected and unaffected areas to identify pathology. Moreover, conventional MRI is inherently insensitive to subtle global changes that may impact the entire brain and central nervous system (CNS) [5].

Conventional MRI cannot visualize the extent of damage to varying components of CNS tissues, such as myelin, axons, and glial cells [6]. A more refined quantification of the extent, classification, spatial distribution, and temporal evolution of CNS tissue damage in individuals could significantly enhance our comprehension of the underlying disease mechanisms [7-9].

Quantitative MRI possesses the capacity to fulfill these requirements by delivering more sensitive assessments of pathology and providing explicit information regarding the specific

tissue components that have sustained damage. Unlike conventional MRI, which collects datasets that encompass a mixture of weightings and therefore cannot yield a definitive quantitative map, quantitative MRI relies exclusively on imaging acquisitions that facilitate the disambiguation of signal variation sources. Moreover, through the application of computational or mathematical modeling, quantitative MRI can produce quantitative maps wherein intensities are quantified in physical units. Consequently, quantitative MRI techniques exhibit superiority over conventional MRI in terms of sensitivity to subtle changes within both lesions and normal-appearing tissue, as well as in their enhanced specificity regarding the damage inflicted upon various CNS tissue components, including myelin, axons, glial cells, iron, and blood flow and volume.

The SAR limitation of Spin Echo (SE) sequences at 7T for quantitative imaging, specifically T2 maps, makes T2*-weighted Gradient Echo (GRE) sequences popular in CNS studies. T2* relaxation refers to the decay of transverse magnetization caused by a combination of spin-spin relaxation and magnetic field inhomogeneity. T2* maps have been widely used for assessing pathology in patients suffering from Multiple Sclerosis, Alzheimer's Disease, Schizophrenia, etc. [10-12]. Sensitive to susceptibility in the tissue, it can help identify iron accumulation, blood oxygen levels, and hemorrhages [13-15]. T2* is shorter than T2 alone due to the presence of magnetic field inhomogeneity and other susceptibility effects. By removing the background field inhomogeneity, which manifests as shortened T2* and signal loss, reliable tissue-specific T2* values can be achieved. One of the comprehensive techniques for removing background field inhomogeneity is the voxel spread function (VSF) method, which was successfully implemented at 3T [16-18]. Imaging at ultra-high field MR (7T and above) increased this background field inhomogeneity, which heavily penalizes the

signal and the resulting T2* values. Therefore, it is of importance to implement the VSf method at 7T and assess the reliability of the background field inhomogeneity-corrected T2* maps.

Quantitative susceptibility mapping of the human brain has been intensively used in clinical research due to its sensitivity to magnetic susceptibility of tissue, making it a potent candidate to assess important tissue functions and diseases [19]. The susceptibility contrast is driven primarily by iron (paramagnetic) and myelin, whose lipids and proteins render their layers more diamagnetic than water [20]. Quantitative Susceptibility Maps (QSM) can retrieve the susceptibility information by acquiring mGRE data [21]. Since T2* mapping is achieved through an mGRE acquisition, generating QSM maps will not increase the scanning time or cost. Nonetheless, interpreting QSM with T2* enhances the overall knowledge of the status of the tissue [22].

Myelin is a lipid-rich material that surrounds nerve cell axons (the nervous system's "wires") to insulate them and increase the rate at which electrical impulses (called action potentials) are passed along the axon [23]. MRI can help quantify the myelin content [24]. Changes in myelin can indicate various tissue changes, such as aging, and have been shown to be altered in several pathologies like leukodystrophies, multiple sclerosis, and schizophrenia [25]. MWF mapping with multi-component T2/T2* fitting with non-negative least squares, non-linear least squares is a measure of myelin content that separates short T2/T2* components (myelin) from longer components (intracellular and extracellular water-IEX) [26, 27]. The T2 or T2* spectrum from the MR signal decay curve is divided into two compartments based on the T2/T2* range: (myelin T2<40 ms at 3T, T2*<25 ms at 7T), (IEX: 40<T2<200 at 3T and 25<T2*<100 ms at 7T) [27-29]. MWF is the ratio of the signal coming

from the water trapped between myelin bilayers (short T2s) to the total water in the voxel. MWF maps have found profound application in clinical studies, particularly in myelin-damaging pathologies such as multiple sclerosis (MS), schizophrenia (SZ), aging, etc. [30-33]

Magnetization transfer (MT) is the shifting of energy between different water pools, specifically between macromolecular (myelin) and free water pools, which is known as magnetization transfer. Quantitative magnetization transfer (qMT) quantifies pool size ratio (PSR), that is, the ratio of bound to free water pools, based on quantitative modeling of the magnetization transfer effect [34]. It has been proven that PSR is strongly correlated with the myelin content in the brain [35].

Interpreting qMT, MWF, QSM, and T2* will increase the sensitivity of the observed tissue changes to the underlying pathology. MRI enables this comprehensive characterization non-invasively, both in the brain and the spinal cord.

Given that the advantages of more quantitative approaches in neuroimaging seem obvious, why does clinical neuroradiology still rely almost completely on qualitative techniques? The current rate of progress in qMR methodology is hindered by several factors, including longer scan times, limited sequences available, artifacts like motion and field inhomogeneity, and post-processing complexities. Addressing these limitations requires fast imaging techniques, particularly non-Cartesian sequences that sequence programming experts customize to reduce scan time, correct for artifacts, and minimize fitting errors. In what follows, I have taken these objectives to facilitate the clinical translation of qMR techniques by acquiring multiple reliable quantitative MR maps, including T2*, QSM, MWF, and qMT, in clinically feasible times.

Therefore, targeting the CNS, the main objectives of this work is to demonstrate: (i)

Feasibility of T2* mapping at 7T using Voxel Spread Function (VSF) method for background field inhomogeneity correction and multi-contrast imaging, (ii) Multi-parametric quantitative QSM, MWF, and MT mapping at 7T, (iii) Reproducibility of multi-parametric quantitative T1, T2*, QSM, qMT, and MWF mapping at 7T, and (iv) Fast measurement of the T2* and magnetization transfer with pulse train saturation and under-sampled segmented radial stack-of-stars acquisition at 7T.

Chapter 2: Feasibility of T2* mapping at 7T using Voxel Spread Function (VSF) method for background field inhomogeneity correction and multi-contrast imaging

2.1 Background

Ultra-high-field (7T and above) MRI scanners are gaining popularity, offering higher signal-to-noise ratio (SNR) and improved resolution compared to lower field strength imaging [36, 37]. Not only does the high-resolution imaging improve the image appearance and quality, but it also helps in extracting physiological information by reducing the partial volume effects. Gradient-recalled echo (GRE) pulse sequences and T2* contrast are important tools in high field MR imaging because of the SAR limitations of the spin-echo pulse sequence [38]. Another advantage of the GRE sequence over the spin echo (SE) sequence is that it allows for faster acquisitions by enabling shorter echo times (TE) and shorter repetition times (TR) [39], and it is suitable for breath-hold and real-time imaging. It can be implemented in 2D or 3D with low flip angles that result in better slice profiles. Furthermore, the GRE sequence is sensitive to T2* effects and can detect sources of susceptibility such as hemorrhages or iron deposition in the tissue. GRE images have been shown to detect the paramagnetic effect of blood-breakdown products, allowing visualization of clinically silent microbleeds that are often not detected with head CT [40-42]. The T2*-weighted GRE sequences have also been shown to be able to detect cerebral venous thrombosis [43]. Hypointensities on T2*-weighted GRE images are an indicator of the presence of hemosiderin, deoxyhemoglobin, ferritin, calcium, other metals, and air [44]. Quantitative T2* mapping has the potential to reflect changes in the biochemical components of several pathological conditions such as cerebral

hemorrhage, arteriovenous malformation, cavernoma, tumor hemorrhage, punctate foci of hemorrhage in diffuse axonal injury, superficial siderosis, old intraventricular hemorrhage, and thrombosed aneurysm [44, 45]. A limitation of the T2* -weighted GRE sequences compared to the SE sequences is that the GRE images suffer from background field inhomogeneity artifacts affecting T2* quantification. This can potentially confound the changes in T2* caused by pathology [46]. This problem worsens when imaging at ultra-high-field MRI due to increased macroscopic susceptibility, and these susceptibility artifacts must be accounted for when quantifying T2* [47]. Numerous methods have been proposed to deal with this problem [48-51]. Through slice field inhomogeneity has been modeled as a sinc or quadratic function in 2D multi-slice imaging [28, 52-56]. These 2D approaches assume no field inhomogeneity in the readout and phase encoding directions, which can still lead to inter-voxel signal contamination and artifacts. Other methods address the problem of background field inhomogeneity by optimizing the sequence design [48, 57-59], or by modeling and correcting the effects of macroscopic field variations during post-processing [60-62]. Another approach is to use a B0 field map self-derived from 3D multiple-echo GRE images in the chemical shift encoding direction for field correction [52]. However, this approach still does not address the inter-voxel signal leakage, which is an important factor affecting the field distribution in a voxel. The voxel spread function (VSF) method has improved on these techniques and reformulated the GRE signal equation in the presence of background field inhomogeneity [16, 17]. This newly formulated equation enables the correction of background field inhomogeneity and provides quantitative T2* maps. A modification of the VSF method for z-shimmed multi-gradient echo (mGRE) images has been demonstrated; however, this requires additional scans, resulting in increased scan time [63].

In this study, we demonstrate the application of the VSF post-processing technique at ultra-high field (7 T) MRI setting. The VSF method is implemented for 3D multi-echo gradient-echo (mGRE) data, which allows for isotropic high-resolution images of the brain. In addition to quantitative T2* maps, the method also generates other contrast images such as T1-weighted, tissue frequency maps, and susceptibility-weighted contrast images from the same dataset, i.e., the Gradient Echo Plural Contrast Imaging (GEPCI) [64]. This approach has been shown to identify abnormalities that are not visible on standard clinical MRI images [64]. Implementation of this approach at ultra-high-field MRI settings is necessary because it will increase the detection sensitivity to magnetic susceptibility differences caused by pathology [65].

2.2 Materials and Methods

2.2.1 Theory

T2* relaxation, a combination of spin-spin relaxation and magnetic field inhomogeneity, is observed in gradient-echo (GRE) imaging. It is a key determinant of image contrast in GRE sequences and forms the basis for various magnetic resonance (MR) applications. T2*-based imaging, achieved by manipulating GRE sequence parameters, enables the detection and characterization of lesions and structures through signal intensity changes caused by magnetic field inhomogeneities. The main advantages of using T(2)* relaxation are (1) a low specific absorption rate (SAR), which is especially beneficial for imaging at high field strengths, (2) a short first-echo time (approximately 2 ms), and short echo spacing (approximately 1 ms) [66]. As there is no 180-degree refocusing pulse available to cancel the effects of magnetic field inhomogeneity, T2* is shorter than T2 (Figure 2.1).

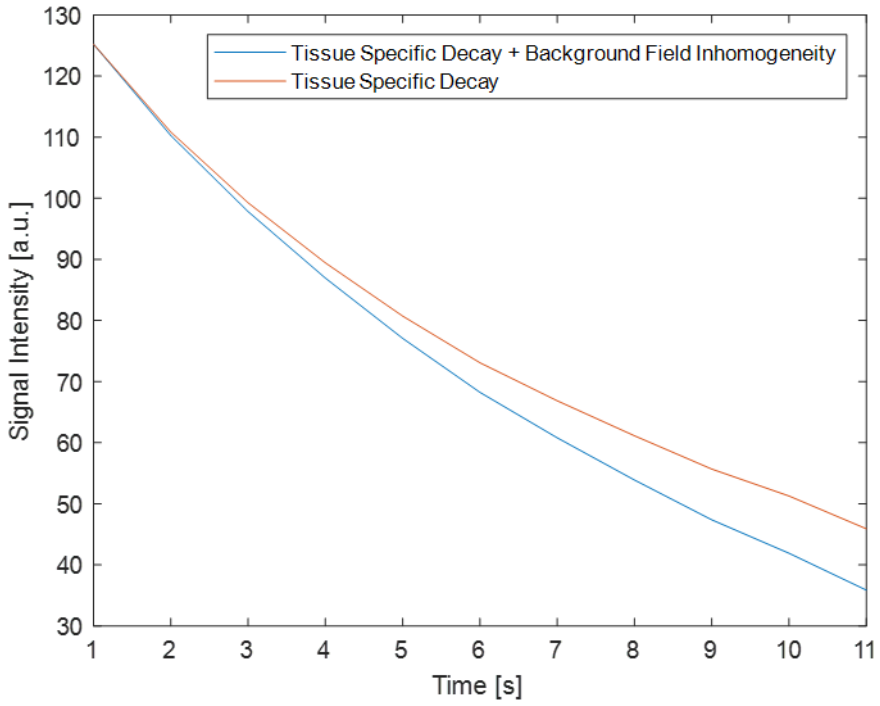

Figure 2.1: Simulation showing the comparison between T2 and T2* decay curves. Signal with T2* relaxation time decays faster and is influenced by the susceptibility effects.

T2* mapping can be achieved by exponentially fitting the TE-dependent signal intensities of gradient-echo images and gradient-echo EPI.

$$S(TE) = S_0 . \exp\left(\frac{-TE}{T_2^*}\right) \qquad 2.1$$

Reliable quantification of T2* values requires implementing an appropriate background field inhomogeneity correction. Some of the most common methods for removing the contributions of the background field inhomogeneity in the resulting T2* maps and generating reliable T2* values are outlined in the following subsections.

2.2.1.1 Background field inhomogeneity correction techniques

The contribution of the macroscopic background inhomogeneity can be modeled as a $sinc$ function assuming that the pixel is a rectangle in the direction of the gradient G and the background field over the voxel is linear [67].

$$S(TE) = S_0(t).\exp\left(\frac{-TE}{T_2^*}\right).\left[\frac{\sin\left(\frac{\gamma(\Delta B_0)}{2}TE\right)}{\frac{\gamma(\Delta B_0)}{2}TE}\right] \quad 2.2$$

$$S(TE) = S_0(t).\exp\left(\frac{-TE}{T_2^*}\right).sinc\left(\frac{\gamma(\Delta B_0)}{2}TE\right) \quad 2.3$$

where $S(TE)$ is the measurement at echo time TE, $S_0(t)$ is the decay signal without background field inhomogeneity, γ is the gyromagnetic ratio, and $\Delta B_0 = G_z\,.\Delta z$ where G_z is the local field gradient along the slice direction and Δz is the slice thickness.

The sinc-function approach, which assumes that the through-plane magnetic field inhomogeneity can be described in terms of a constant magnetic field gradient, is one of the most common approaches used in the literature to describe the contribution of the background field. This method completely ignores the correction along the x and y directions, and the constant field assumption is not valid for all acquisitions, especially at higher field strengths. This can be demonstrated by simulating the signal model in the presence of background field inhomogeneity at higher field strengths.

2.2.1.1.1 Simulation

The synthetic one-dimensional signal with 16 voxels (Figure 2.2) was simulated in MATLAB using the parameters in Table 2.1, following the signal equation Eq 2.4:

$$S(\boldsymbol{k}, TE) = S_0(\boldsymbol{k}, t).F(TE) \qquad 2.4$$

Where $F(TE)$ is the MR signal that would exist in the absence of macroscopic magnetic field inhomogeneity and $\boldsymbol{k}$ is the spatial frequency**.** The proton density in voxel number 9 was set to 1 and 0 otherwise.

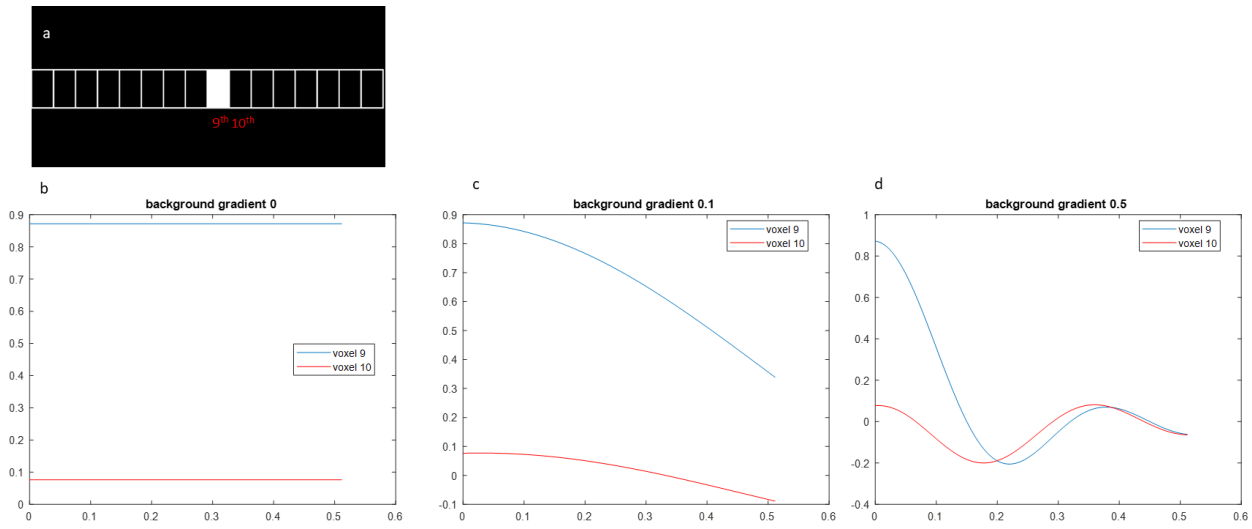

Figure 2.2: a) 16 voxels of the simulated MR signal with a non-zero proton density in voxel number 9. 16 phase encoding steps are required to localize these 16 voxels spatially. **B**) Signal simulation in the absence of the background field inhomogeneity, **c**) signal affected by 0.1 background field inhomogeneity, and **d)** severe background field inhomogeneity (0.5), which is the case at ultra-high field MRI.

Table 2.1: Parameters used for simulating an MR signal in the presence of the background field inhomogeneity.

FOV	Phase Encoding (PE) steps	Number of voxels	T2 relaxation time	Time interval [s]
256	16	16	∞	[0 0.512]

The simulation results shown in Figure 2.2 b-d show that by increasing the contribution of

the background field inhomogeneity, which is the case at ultra-high MR field settings, a constant through-plane background field inhomogeneity leading to the $sinc$ model does not generate the expected signal. Furthermore, evaluation of the contribution of field inhomogeneities to the F-function in Eq. 2.4 in the readout and phase encoding directions is different due to the well-known Gibbs ringing artifacts, which lead to intervoxel signal leakage [68]. These effects are dramatically enhanced in the presence of B_0 inhomogeneities. More sophisticated approaches need to be implemented for accurate T2* quantification.

2.2.1.2 Voxel Spread Function (VSF) Correction

The Voxel Spread Function (VSF) correction method, introduced by Yablonskiy et al. (2013), addresses the challenge of macroscopic magnetic field inhomogeneities in gradient-echo MRI, which can distort quantitative measurements such as R2* and susceptibility maps. These inhomogeneities cause signal dephasing and voxel bleeding, leading to inaccuracies in tissue property assessments [16]. By analyzing both magnitude and phase data from multi-echo GRE sequences, it quantifies the "spread" of signal contributions due to field gradients. This enables the correction of artifacts without the need for additional scans or complex post-processing. The method introduces the F-function, representing the influence of neighboring voxels' signals on a given voxel due to field inhomogeneities, Eq 2.5 – 2.7.

$$S(\boldsymbol{k}, TE) = \int d\boldsymbol{r}.\, \rho(\boldsymbol{r}, TE)\, exp(-2\pi i \boldsymbol{k}\boldsymbol{r})\,.\, exp\,(i\gamma b(\boldsymbol{r})TE + i\varphi_0(\boldsymbol{r})) \qquad 2.5$$

Eq 2.5 encodes the background field gradients into the signal model in k-space. $\rho(\boldsymbol{r}, TE)$ is the "ideal" signal evolution that would exist in the absence of magnetic field inhomogeneities, and the integral is over the object volume. γ is the gyromagnetic ratio, $\varphi_0(\boldsymbol{r})$ is the signal phase shift at $TE = 0$ mainly resulted from RF field inhomogeneities and

$\boldsymbol{k}$-space is defined in a standard manner as

$$2\pi \boldsymbol{k}_x = \gamma G_x t_x \ ; \ 2\pi \boldsymbol{k}_y = \gamma G_y t_y \ ; \ 2\pi \boldsymbol{k}_z = \gamma G_z t \qquad 2.6$$

Where G_x, G_y, and G_z are phase encoding (x and y) and read-out (z) gradients, t_x and t_y are durations of x and y gradients, and t is the time during the gradient echo acquisition t is zero at the center of the gradient echo.

Eq 2.7 is the image-domain signal model with VSF correction. Fitting this signal model to a multi-echo gradient echo (mGRE) data yields the corrected $T2^* = 1/R2^*$ along with the magnitude $S(0)$ and frequency (f) maps.

$$S(TE) = S(0).exp\left(-\frac{TE}{T2^*}\right).exp(-i2\pi f.TE + i\varphi).F(TE) \qquad 2.7$$

VSF has been successfully implemented for 3T MR settings [16, 17]. However, considering the more severe field perturbations at higher fields, the feasibility of the VSF technique at ultra-high-field MRI (7T and above) has not been previously addressed. In the following analysis, the feasibility of the VSF method is examined through a series of phantom and in vivo experiments conducted in the human central nervous system (CNS) at 7 T.

2.2.2 Data Acquisition

2.2.2.1 Phantom

The phantom experiment was done on a 7T Siemens Magnetom MRI scanner (Siemens, Erlangen, Germany) with a 32-channel head coil and a 3D multi-echo gradient-echo sequence. The feasibility of the VSF technique was first validated on a phantom designed to create a magnetic field perturbation. The phantom consisted of a large cylindrical bottle (15

cm long and 10.5 cm in diameter) containing nickel chloride-doped saline solution (see Figure 2.3). Three smaller tubes (12 cm long and 3 cm in diameter) were fixed to the larger phantom, consisting of 4% and 2% agarose solution in saline. This arrangement creates magnetic field inhomogeneities within the tubes and phantoms. The experiment was conducted using the following parameters: the isotropic 3D resolution of 1×1×1 mm^3, TR = 30 ms, 11 gradient echo images with $TE(0) = 1.95$ ms, and echo spacing of 2.63 ms, flip angle = 30°.

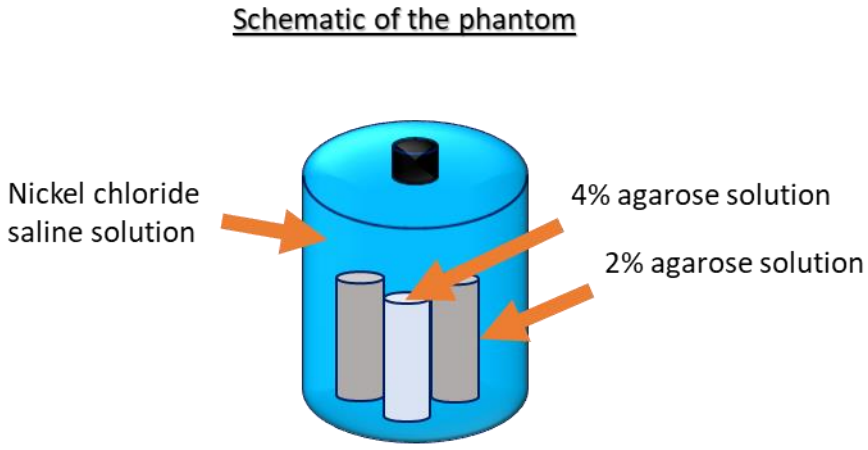

Figure 2.3: The schematic of the phantom created for VSF-corrected T2* mapping. The phantom consisted of a large cylindrical bottle (15 cm long and 10.5 cm in diameter) containing nickel chloride-doped saline solution. Three smaller tubes (12 cm long and 3 cm in diameter) were fixed to the larger phantom, consisting of 4% and 2% agarose solution in saline.

Before the in vivo study, all subjects provided written informed consent approved by Institutional Review Board.

2.2.2.2 Brain

A brain experiment was done on a 7T Siemens Magnetom MRI scanner (Siemens, Erlangen, Germany) with 32-channel head coils. Eleven healthy volunteers were recruited for the study. T1-weighted or proton density-weighted 3D GRE Images were obtained with the

following parameters: the isotropic 3D resolution of 1×1×1 mm^3, number of slices: 30, Flip angle 30˚ for T1 weighting and 6° for proton density weighted. TE (0) = 1.96 ms, number of echoes 11, echo spacing: 2.64 ms, and TR: 30 ms. The raw data was then transformed into a workstation and analyzed using MATLAB (MathWorks, Natick, MA) software.

2.2.2.3 Spinal Cord (SC)

Spine Imaging data was acquired on the Siemens 7T Magnetom with an 8-channel surface coil. The 3D mGRE Images were acquired from a healthy subject with the following parameters: 22 slices with the resolution of 0.5 × 0.5 × 3 mm^3, TR = 40 ms, flip angle 45˚, and nine gradient echo images with TE (0) = 2.42 ms and echo spacing of 3.6 ms. Raw data was transferred to a workstation and analyzed with the Spinal Cord Processing Toolbox (SCT)[69] and MATLAB (MathWorks, Natick, MA).

2.2.3 Data Processing

Data from all receiver channels were combined using the following formula to remove the channel phase dependence, as described in [16].

$$S_{comb}(TE_n) = 1/M \cdot \sum_{m=1}^{M} \eta_m \cdot S_m^*(TE_1) \cdot S_m(TE_n), \quad 2.8$$

$$\eta_m = \frac{1}{M\sigma_m^2} \cdot \sum_{m=1}^{M} \sigma_m^2 \quad 2.9$$

M is the number of channels, $S(TE)$ is the signal at a given TE, $S^*(TE_1)$ is the complex conjugated signal at echo "1", and σ_m is the noise level at channel m. Phase unwrapping was performed in the time domain with the method described in [64] followed by 3D phase unwrapping in the spatial domain [70] . To determine the average phase and the magnetic field

in each pixel, unwrapped phase data of the surrounding pixels are fit to a first-order polynomial. The estimated field map was then used to calculate the background field gradients in all three directions (readout, phase, and slice), and the Voxel Spread Function ($F(TE)$) was determined. The theory has been previously described in detail [16, 17]. Finally, the complex multi-echo GRE data were then fit to the following equation that includes the F-term to compensate for the field inhomogeneity contribution to Eq. 2.7. Least-squares fitting was performed on the complex data using the Levenberg-Marquardt algorithm in MATLAB. T2*-maps were also generated without field inhomogeneity correction.

2.2.3.1 Brain

For the brain experiment, along with the T2*, frequency, and magnitude images, susceptibility contrast weighted images from multi-echo GRE data were generated as described previously using TE = 17 ms echo time image [64]. In particular, local frequency maps obtained from Eq. 2.7 was used to generate complementary GEPCI images: T1f, SWI-like, and GEPCI-SWI [64]. To create complementary GEPCI images, we used 2-3 frequency mask multiplications. This number was determined empirically. GEPCI images have the following properties: T1f enhances the GM/WM T1 contrast, SWI-like image has similar susceptibility contrast as the standard SWI, and GEPCI_SWI image has enhanced susceptibility contrast, free of T1 contamination and RF field inhomogeneity.

In addition to standard GEPCI, which relies on T1-weighted images, we also demonstrate application with proton density-weighted images. This is helpful while interpreting proton density correlation with the venous information. We fit the proton density-weighted data to the signal model in Eq. 2.7. The estimated T_2^* map is then used in Eq. 2.10 to generate the GEPCI-SWI image:

$$GEPCI - SWI(TE) = exp\left(\frac{-TE}{T2^*}\right).FM^n \quad 2.10$$

Where FM is the frequency mask obtained by setting negative frequency values in the frequency map to zero and normalizing the positive frequency values to the values between 0 and 1 so that the brighter looking frequency values are mapped to darker values close to zero. In this way, veins that are bright on the frequency map are mapped to smaller values close to zero. The WM region appears dark on the frequency map and, therefore, is mapped to brighter values in the frequency mask (FM). Multiplying this frequency mask (FM) helps enhance the GM/WM contrast as well as accentuate the venous structure (n is the number of multiplications).

2.2.3.2 Spinal Cord

The magnitude image from the first echo (Figure 2.4a) was used for SC segmentation. The SC was segmented using the deep learning-based algorithm in the SCT toolbox (Figure 2.4b). Vertebral labeling was performed manually on the segmented SC by selecting the posterior tip of each of the imaged intervertebral discs (Figure 2.4c). The resulting segmented, labeled MR image was then registered to the PAM50 SC Template [71], and the SC GM and WM masks were generated (Figure 2.4d-f). The VSF method was then applied to the segmented regions. The VSF approach calculates the F-function ($F(.)$) from multi-gradient echo phase images to determine the contribution of the magnetic field inhomogeneity on the signal decay. This F-function is then used to eliminate/reduce the effect of the magnetic field inhomogeneity in T2* calculations by using Eq. 2.7.

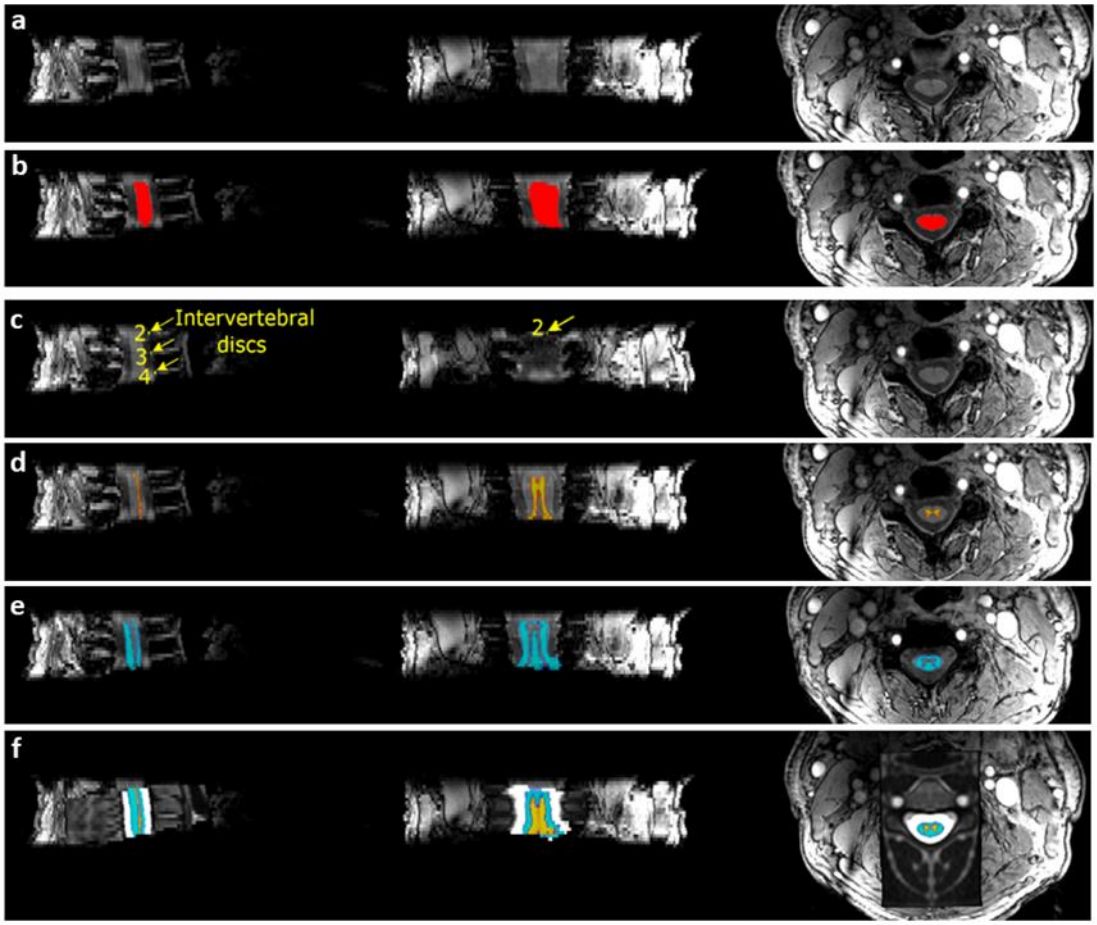

Figure 2.4: SCT analysis on the mGRE magnitude image. **(a)** the magnitude image from the first echo that was used for segmentation. **(b)** deep-learning-based segmentation results in red overlaid on the anatomical image. **(c)** intervertebral disc labels 2,3 and 4 of the imaged regions shown with arrows, **(d)** the GM and **(e)** the WM segmentation results, and **(f)** an overlay of the mGRE magnitude image (backmost image), GM mask (yellow), WM mask (blue), and PAM50 template.

2.3 Results

2.3.1 Phantom

The Results for the phantom experiment are shown in Figure 2.5. Macroscopic background field inhomogeneity due to this layout of the phantom creates additional signal decay, causing T2*-shortening (Figure 2.3a). T2* in the middle tube without accounting for background field correction is 41.6 ± 6.5 ms and changed to 53.2 ± 2.1 ms with F-term

correction. The outer tube T2* changed from 21.3 ± 2.0 ms (without) to 26.1 ± 0.7 ms (with) *F*-term correction. In all tubes, the standard deviation of the T2* values are decreased after field inhomogeneity correction. This shows more uniform T2* maps inside each tube after background field inhomogeneity correction.

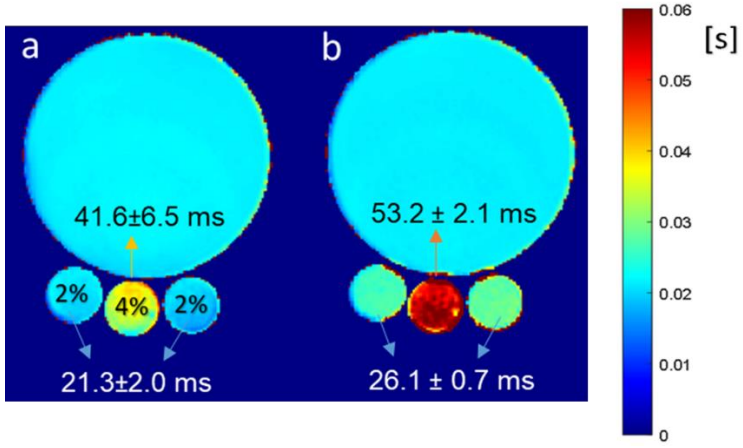

Figure 2.5: T2* -maps from the phantom study, **a)** without and **b)** with correction for the macroscopic magnetic field inhomogeneities. The bar is in seconds. The arrangement causes magnetic field inhomogeneities in the tubes. Without accounting for the magnetic field inhomogeneity, the middle smaller tube (2% agarose) has a T2* = 41.6 ± 6.5 ms, and the outside tube (4 % agarose) has T2* = 21.3 ± 2.0 ms. Accounting for the background field (VSF approach), the T2* is 53.2 ± 2.1 ms and 26.1 ± 0.7 ms in the middle and outside tubes, respectively.

2.3.2 Brain

Figure 2.6 shows several examples of vivo results. The T2* values in general increased after background field inhomogeneity correction and enhanced T2* differences between the gray matter (GM) and white matter (WM). Signal losses in the regions with severe background field inhomogeneity (air-tissue boundaries, frontal, and temporal lobes) are also corrected (red arrows and circles). Quantitative T2* values in human brain GM and WM are summarized in Table 2.2 after FSL FAST segmentation [72, 73].

Table 2.2: T2* values in brain GM and WM before and after VSF correction at 7T.

	T2* before background field inhomogeneity correction [ms]	T2* after background field inhomogeneity correction [ms]
WM	26.9	29.1
GM	28.7	31.9

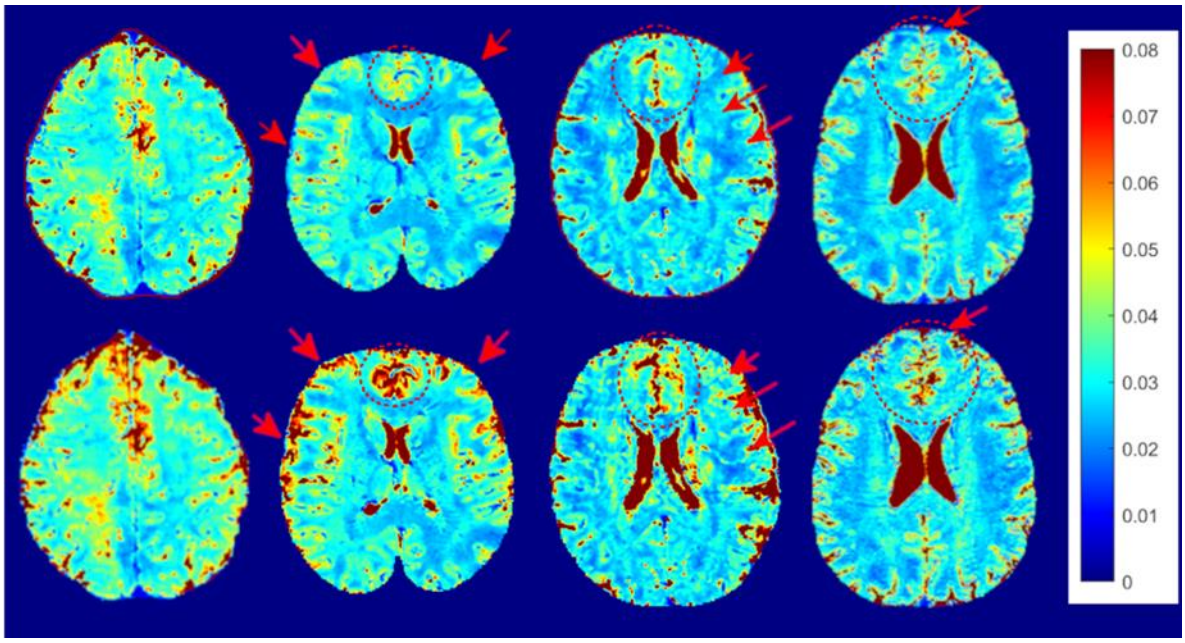

Figure 2.6: T2* maps from the in vivo experiment before field inhomogeneity correction (top row) and after field inhomogeneity correction (bottom row). The average increase in T2* values in both gray matter (GM) and white matter (WM) is evident. The corrected signal losses in the regions suffering from the severe background field inhomogeneity (air-tissue boundaries) are indicated by the red arrows and circles.

Additional complimentary contrast images are shown in Figure 2.7. Minimum intensity projected (mIP) images were created by taking projections over 5 slices. SWI-like images (Figures 2.7a, e) convey the same susceptibility information as standard SWI images; however, our approach offers flexibility in choosing the echo time during post-processing

and can be helpful for a more accurate evaluation of pathology via post-processing. GEPCI-SWI images (Figure 2.7b, f) correct for T1-contamination and keep the CSF bright and hence enhance susceptibility contrast, especially for the veins around ventricles (see white arrows in Figure 2.7f). These veins are covered with the dark CSF in standard SWI images, resulting in reduced visibility (see white arrows in Figure 2.7e. In Figure 2.7a, we used TE=1.95 ms to generate the SWI-like image. This is significantly shorter than the recommended echo time for SWI imaging at 7T (~ 15 ms [74]). Figure 2.7b shows the GEPCI-SWI image using the TE= 17 ms and 3 mask multiplications. This image is free from T1 contamination and has enhanced vein visibility. Figures 2.7c, d. show the frequency map and the maximum intensity projected frequency map across 5 projected slices, respectively.

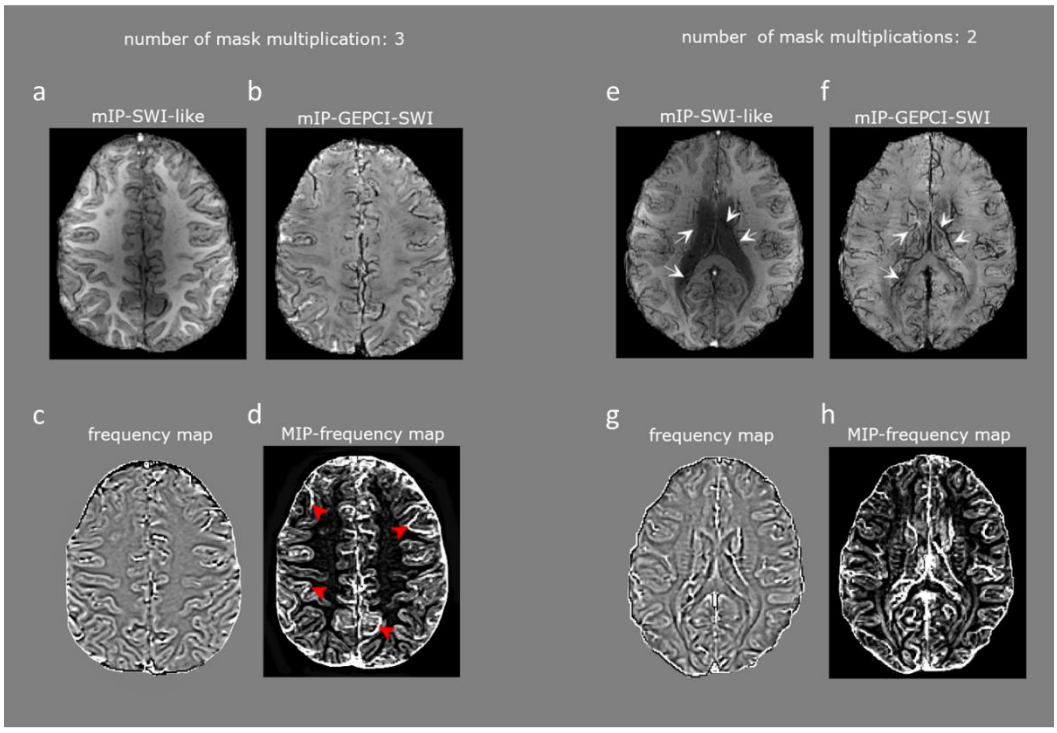

Figure 2.7: **a)** mIP-SWI-like, **b)** mIP-GEPCI-SWI, **c)** frequency map obtained after background field inhomogeneity correction with a range of -1.5 – 1.5 Hz, and **d)** Maximum intensity projected frequency map over 5 slices, veins appear the brightest on this image (red arrowheads). The Number of multiplications is 3. On the right, the number of multiplications is set to 2 for another subject, **e)** shows the SWI-like image, **f)** shows the

enhanced vein visibility on the GEPCI-SWI image particularly around ventricles (white arrows), **g)** The frequency map, and **h)** the maximum intensity projected frequency map over 5 slices. White matter appears darker than veins and the cortex region on the frequency map.

Note that Figure 2.7d shows that the brightest voxels on the frequency map belong to the veins and the cortex region, and WM appears darker compared to them. Figure 2.7e – 2,7h shows an example from another subject. Same echo times with 2 multiplications were used to generate these images. Generating multiple contrast images from the same acquisition can find application in the comprehensive characterization of disease pathophysiology over time [75, 76].

Figure 2.8 compares the T1-weighted image with the T1f image obtained by multiplying the T1-weighted image by the frequency mask generated using the GEPCI technique. GM/WM contrast is enhanced in the T1f image. (Number of multiplications 2).

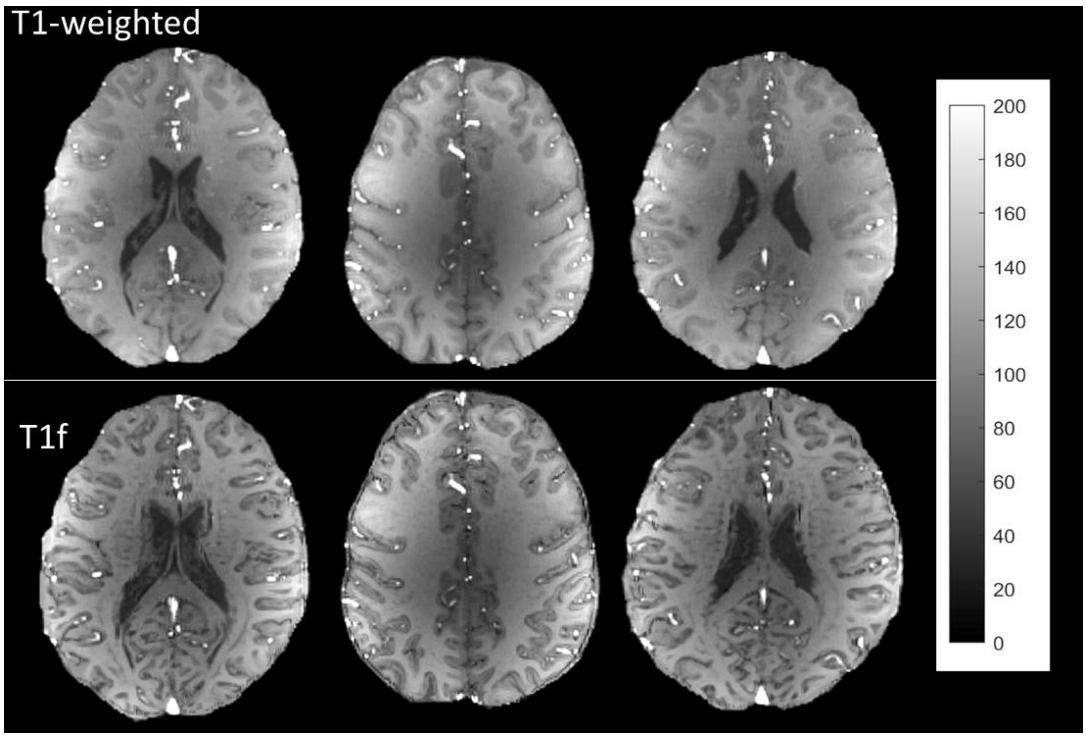

Figure 2.8: T1-weighted image obtained from GEPCI imaging (top row), and the corresponding T1f image obtained by 2 frequency mask multiplications (bottom row). GM/WM T1 contrast is enhanced in the T1f images compared to the T1-weighted images. One can also see some venous information on the T1-weighted image.

Figure 2.9 demonstrates the GEPCI analysis performed on the proton density-weighted mGRE data. Figure 2.9 shows (a) proton density image, (b) mIP GEPCI-SWI image using 15 slices projected, (c) T2* map, and (d) frequency map. The number of multiplications is 2, and a TE of 15 ms was used. Although there is no T1-weighting in these images, anatomical structures can be observed on the frequency map obtained as part of the processing (arrows point to deep gray structures, Such as the Caudate and putamen, in Figure 2.9d). Note that deep gray matter structures and the cortex region appear brighter than the WM, and the veins are brighter than both GM and WM. Having the Proton density information combined with the venous network information is helpful while studying vein-related diseases.

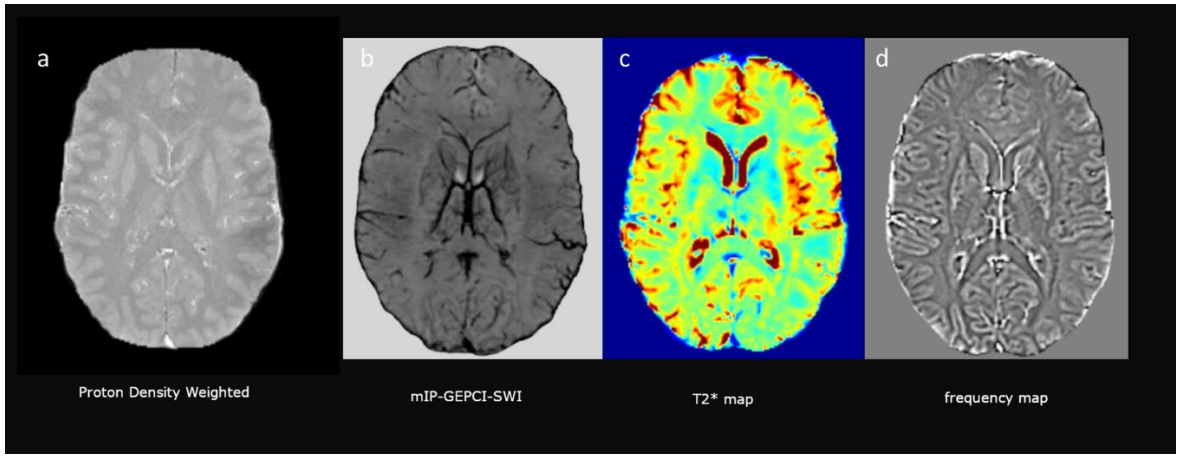

Figure 2.9: (**a**) Proton density weighted image, (**b**) mIP GEPCI-SWI over 15 slices using 2 multiplications and TE=15 ms, (**c**) background field inhomogeneity corrected T2* map (range 0 to 0.05 [s]), and (**d**) frequency map (range -1.5 to 1.5 [Hz]). Accessing proton density information along with the venous network structure might help in the diagnosis and treatment of vein-related disorders (see discussion). Notice the deep gray matter structures delineated with white arrows on the frequency map (caudate and putamen).

2.3.3 Spinal Cord

T2* mapping was performed on human spinal cords. Figure 2.10 shows the T2* maps and the frequency maps of different slices obtained after fitting Eq. 2.7 to the complex mGRE data. T2* values increased in both SC GM and WM, and the T2* contrast between the two regions was also enhanced after field inhomogeneity correction. In addition to improving the estimate of gray and white matter T2*, the VSF correction significantly reduces magnetic field inhomogeneity artifacts in the regions marked with red arrows. The average T2* values in GM and WM with/without accounting for the background field correction are in Table 2.3.

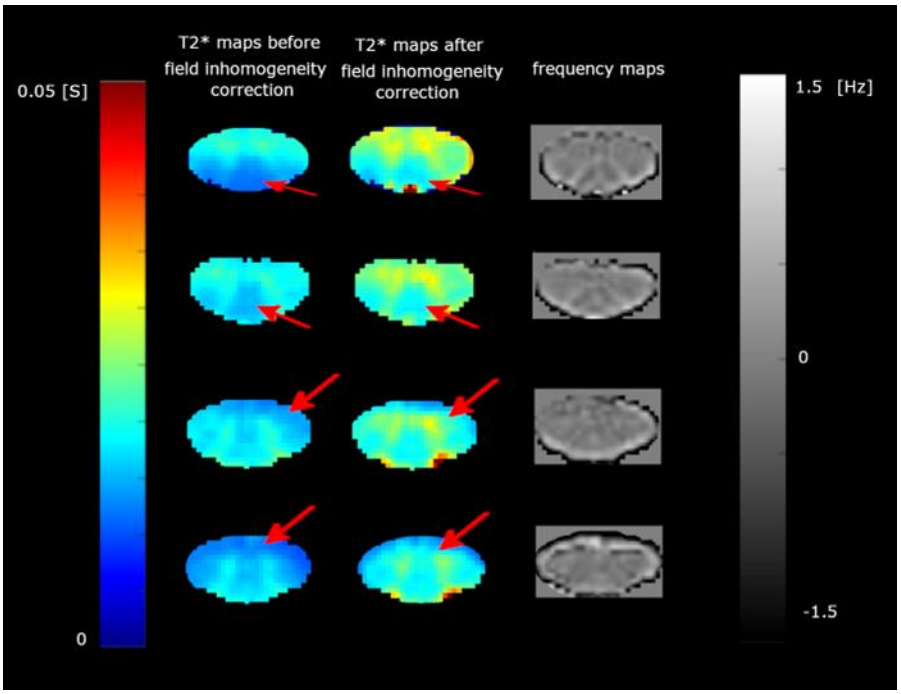

Figure 2.10: (**a**) Estimated co-registered images obtained after fitting Eq 2.7 to the complex mGRE data: First Column: T2* maps before background field inhomogeneity correction, Second Column: T2* maps after background field inhomogeneity correction, and Third Column: frequency maps. VSF correction significantly reduces magnetic field

inhomogeneity artifacts by correcting the signal losses in the regions marked with red arrows.

Table 2.3: Average T2* in human SC, GM, and WM. The average T2* values generally increased after background field inhomogeneity correction for both SC GM and SC WM.

Slice number	SC GM T2* (mean ± std) [ms]		SC WM T2* (mean ± std) [ms]	
	Before background field inhomogeneity correction	After background field inhomogeneity correction	Before background field inhomogeneity correction	After background field inhomogeneity correction
1	19 ± 2.3	26.6 ± 2.6	16.1 ± 3.3	23.3 ± 4.7
2	19.8 ± 1.2	26.7 ± 2.3	17.8 ± 1.7	22.5 ± 2.8
3	18.9 ± 1.5	25.4 ± 2.3	17.2 ± 2.1	21.3 ± 4.6
4	16.6 ± 1.5	22.4 ± 1.8	14.8 ± 2.5	19 ± 4

2.4 Discussion

In this study, we addressed T2* -mapping in the human central nervous system at 7T. Through a series of phantom and in vivo experiments, we demonstrated the feasibility of the VSF method in correcting for background field inhomogeneities that affect T2* measurements at 7T. It is worth mentioning that ultra-high-field MR imaging, combined with fast high-resolution 3D gradient-echo imaging, provides enhanced resolution, contrast, and sensitivity in neuroimaging [77]. Here, we successfully implemented a background field inhomogeneity technique (VSF) tailored for mGRE data at ultra-high field MRI settings (7T). We showed that using the F-function ($F(TE)$) correction with the mGRE data produces reliable quantitative T2* maps. We also used the GEPCI technique at 7T to generate susceptibility-weighted contrast images using mGRE data. The T2* relaxation time constant, as well as GEPCI contrast images, have the potential to serve as surrogates for tissue biological features, such as T1 and T2 relaxation times. The advantage of GEPCI imaging

at 7T is its ability to provide better resolution for depicting smaller veins. Unlike venography at a single fixed echo time, GEPCI offers the flexibility to select different echo times to depict this venous structure. We used TE=17 ms to generate the GEPCI-SWI images, which is comparable to the TE value considered to generate SWI images at 7T [74]. SWI-like images can be generated by echo times as short as TE= 1.95 ms. The flexibility of choosing the echo time while generating the GEPCI images using the mGRE data removes the limitation of the standard single echo, and analysis can be adapted to highlight pathology without reacquiring data. Gradient echo susceptibility weighted imaging (GE-SWI) can help in visualizing the veins in directions other than parallel to the main magnetic field (by choosing longer echo times) [78]. Generating susceptibility contrast using the GEPCI technique is the same as an ordinary SWI image in creating a frequency mask (instead of a phase mask) and multiplying it by the magnitude data [79]. The local frequency map obtained in GEPCI imaging is then used to generate the frequency mask as described in [64], which is required for generating the secondary co-registered GEPCI images: T1f, SWI-like, and GEPCI SWI. These images help in accessing susceptibility-related information that is not otherwise apparent on the original mGRE magnitude images.

Studying the venous structures alongside the proton density weighted MR images finds importance in revealing the aneurysm and the varicose veins [80]. Since an early diagnosis of the venous aneurysm is recommended for proper early repair, monitoring the venous structure, along with proton density information, before the onset of symptoms is crucial. To generate the GEPCI image using the proton density-weighted image, we followed the same routine as [64], with a difference that the original complex data used for fitting is not T1-weighted. We demonstrated that GEPCI-SWI can visualize vein structure even when a T1-

weighted image is not available. This may prove helpful when interpreting proton density correlation with venous information. Although there is no T1-weighted image to access the anatomical structure in this data set, the frequency map obtained in the GEPCI technique carries structural information needed and helps in revealing the venous structure.

One of the VSF applications is incorporating a representative BOLD signal contribution into the GEPCI signal model and quantifying the tissue-specific relaxation time constant (T2*) [81, 82]. Another important application of the Voxel spread function is to remove the background field inhomogeneity in the myelin water fraction (MWF) imaging. Future work will include multi-exponential T2* analysis at 7T to acquire artifact-free MWF maps. This analysis can be performed on the field inhomogeneity-corrected T2* maps or can be directly embedded into the signal model to generate the amplitude, T2*, and frequency shift maps for the myelin water and intra/extracellular water compartments. One potential application of the GEPCI technique is the early diagnosis or improved monitoring of MS patients by enabling the collection of venous information [83]. In addition, multiple contrast images with susceptibility-weighted property can help in the diagnosis and the treatment of vein-related disorders. Diagnosis of deep vein thrombosis (DVT) can be performed by detecting hyperintensities on the T1-weighted images acquired by the magnetization-prepared GRE sequence [84-86]. Additional applications can target imaging and monitoring the correlation between COVID-19-related cerebral venous thrombosis [87, 88]. Therefore, implementing the processing pipeline covered in this work on COVID-19 patients is an interesting topic to follow. For the spinal cord, we successfully implemented SCT analysis and VSF to generate high-resolution quantitative T2* and frequency maps in the spinal cord. T2* maps were generated from the same mGRE data that was used for segmentation and registration; hence,

there was no need to re-register the obtained maps over anatomical images. The T2* value in general increased after background field correction, and the method was able to enhance gray/white matter (GM/WM) T2* contrast. This work shows that the VSF method is effective in reducing background field inhomogeneity from quantitative T2* estimates in SC MRI at 7T. In conclusion, we have implemented an effective technique for removing background field inhomogeneity in the human central nervous system (CNS) at 7T, where the effect of magnetic susceptibility-related artifacts is particularly pronounced. Voxel spread function enables T2* relaxation time quantification that has significantly reduced background field inhomogeneity contamination and is representative of tissue properties. We also generated naturally co-registered contrast images using the GEPCI technique. The results revealed enhanced T2* values, as well as simultaneous susceptibility-weighted contrast, alongside conventional MR contrast images. Generating susceptibility-weighted images at ultra-high field MRI settings provides higher resolution and aids in visualizing smaller vein details. The approach has the potential to be used for T2*-based MWF imaging, Quantitative susceptibility mapping, quantifying iron deposition and calcification, and many other applications, offering flexible and fast acquisitions with higher SNR and resolution. There is no additional scan cost associated with GEPCI imaging, and only a single mGRE scan can generate multiple naturally co-registered contrast images.

Chapter 3: Multiparametric Quantitative MR Mapping Pipeline for Human Brain at 7T Terra. X using Clinically Available Sequences

3.1 Introduction

Clinical MRI is used to diagnose and monitor neurological diseases such as multiple sclerosis (MS), Alzheimer's disease (AD), and many more [89]. Clinical MRI focuses on the qualitative interpretation of MR images by acquiring spatial maps of relative variations in signal strength, which are "weighted" by specific parameters. (e.g., T1-weighted, T2-weighted, proton density-weighted images). Quantitative MRI (qMRI) generates maps of tissue's physiological properties and may contain vital information about tissue microstructure, iron deposition, myelin concentration, etc. This can enable the use of MRI in multi-site clinical studies, monitor disease progression and responses to therapeutic interventions, and help optimize treatment [24, 64, 90, 91]. Quantitative MRI (qMRI) is a rapidly advancing field that enables non-invasive mapping of physical tissue properties, offering reproducible and biologically meaningful biomarkers. QMRI at 7T offers considerable advantages due to increased signal-to-noise ratio (SNR) and enhanced contrast mechanisms. The higher field strength improves spatial resolution and sensitivity to magnetic susceptibility, making it ideal for detecting subtle microstructural features. This is particularly relevant for QSM and T2* imaging, as susceptibility effects scale with B0 field strength. Moreover, the spectral separation between water and macromolecular pools is enhanced at 7T, improving the estimation of myelin-sensitive metrics such as MWF and qMT F [92-94]. In this study, we first introduce a clinically feasible multi-parametric qMR

protocol at 7T to generate the maps of R2* (1/T2*), QSM, MWF, qMT, and T1 relaxation maps. The rationale behind this selection of qMR maps is that they are highly sensitive to myelin and iron content in the brain, which is important in neurological diseases in WM and GM, such as MS and Alzheimer's disease [95-99]. Furthermore, multiple parameters can be simultaneously obtained from the datasets (qMT and T1, R2* and QSM), potentially reducing scan time and/or increasing SNR.

QMT measures the magnetization exchange between the water protons and the protons bound to macromolecules [100]. qMT can be used to indirectly quantify myelin in the brain [34], which is particularly relevant for studying neurodegenerative disorders such as multiple sclerosis (MS), Alzheimer's disease (AD), amyotrophic lateral sclerosis (ALS), etc. [101-103]. qMT involves fitting multiple images to a mathematical model to extract tissue-specific parameters related to physical quantities, such as pool sizes, magnetization exchange rates between pools, and the T1 and T2 relaxation times of each pool. Compared to qualitative magnetization transfer ratio (MTR), qMT is more robust to variations in sequence parameters, scanners, and vendors[34]. There are different approaches to generating qMT maps: continuous-wave (CW) saturation [100], pulsed saturation [104-106], selective inversion recovery (SIR) [107-109], and stimulated echo [110] methods. Although pulsed saturation qMT is the most commonly used qMT method[111]; however, this approach requires co-registered additional data (e.g., maps of the main magnetic field, the transmit radio frequency field, and T1 maps), resulting in a complicated data analysis pipeline. Additionally, using saturation pulses can lead to increased SAR deposition at ultra-high fields. An alternative approach, the selective inversion recovery (SIR) qMT [98, 107-109, 112-114] technique, addresses these limitations by providing qMT maps in the human brain even at 7T[114]. With this technique,

not only is all data necessary to estimate qMT parameters contained within the SIR acquisition, but an extra co-registered T1 map can also be generated. Although various techniques are available to generate T1 maps [115-121], this work employed the inversion recovery (IR) method [122, 123] as its data is readily available in SIR acquisition, does not need accompanying field maps, and is considered a gold standard for T1-mapping [124].

R2* relaxation rate constant and quantitative susceptibility (QSM) maps are important due to their sensitivity to magnetic susceptibility variations caused by tissue micro-structure, macromolecule content, iron deposition, calcium, and deoxyhemoglobin levels, etc. [125, 126] [95]. QSM contrast is sensitive to myelin, whose lipids and proteins render its layers more diamagnetic than water [127], making it a useful biomarker of white matter (WM) pathology [128]. R2* can be calculated using a multi-echo gradient-recalled echo imaging (mGRE) that allows generating R2* by applying a mono-exponential fit [129, 130]. However, these techniques usually ignore the mGRE phase information that can be effectively used to account for background field inhomogeneity, which can cause R2* underestimation and negatively impact the reproducibility of the generated R2* maps [131]. The voxel spread function (VSF) is a post-processing technique that incorporates the contributions from the background field into the signal model to generate R2* maps [16, 17]. VSF has been successfully demonstrated with promising results on the 3T. In this work, we implemented VSF to generate background field inhomogeneity-corrected R2* maps at 7T and studied its reproducibility. QSM maps can be obtained from the same mGRE dataset acquired for R2* mapping, making them inherently coregistered. Among different QSM mapping methods such as Truncated K-space Division or TKD[132], Morphology Enabled Dipole Inversion (MEDI) algorithm[133], Calculation of susceptibility through multiple orientation sampling (COSMOS) [134], and

other techniques [135, 136], we used the QSMnet approach to perform dipole deconvolution from the source field map to generate the susceptibility maps. QSMnet is a deep neural network that generates susceptibility maps from single orientation data [137]. The network is trained using COSMOS-generated QSM maps, which are, in essence, considered the gold standard [137]. It has been shown that QSMnet maps are more consistent across multiple head orientation data compared to TKD or MEDI [137]. Since QSMnet is trained on 3T data, it is essential to evaluate its performance on data acquired at 7T.

Myelin is a lipid-rich material that surrounds axons (the nervous system's "wires") to insulate them and increase the rate at which electrical impulses (called action potentials) are passed along the axon [24]. It is an important parameter because the myelin content and integrity affect the speed of action potential propagation and brain function. It is an essential marker of disease progression in demyelinating diseases such as MS [138]. The myelin water fraction (MWF) is the ratio of the short T2 compartment from myelin (between 10 and 40 ms for humans in vivo) to the long T2 compartment of the entire T2 histogram in a single voxel [24]. Several different MWF mapping methods have been reported, including a three-pool complex model fitted to multi-echo gradient echo (mGRE) complex data with non-linear least squares (NLLS) [27], and multi-echo spin echo (MSE) T2 spectrum analysis with non-negative least squares (NNLS) [26, 139]. A technical review of various MRI-based MWF mapping techniques can be found in [29]. The mGRE approach requires a custom pulse sequence (i.e., to increase the number of available echoes) and computationally complex fitting of nine or more parameters to account for the background field inhomogeneity. In this study, we used conventional MSE data for MWF mapping using the multi-component non-parametric T2 relaxometry that was originally implemented for (FAST-T2) data at 1.5T and

3T [140]. Many MR parameters are accessible for quantitative imaging and have been tested for reproducibility through scan-rescan experiments [141-143]. Multi-parametric qMR mapping of the human brain has long enabled comprehensive analysis of the brain, representing tissue physiological and structural properties. Authors in [131] have pursued optimizing a multiparametric mapping of the human brain at 3T using different vendors' product sequences rather than custom sequences. The protocol used in their study is called the multiparameter mapping (MPM) method [144], which has been widely used in various trials [145, 146]. Leutritz T et. al., [131] generated R1 (1/T1), R2*, PD, and MTsat maps in about 18:45 min on the Siemens scanners. They report a high inter-site comparability with a low inter-site bias of <5% in the qMR maps generated. Their intra- and inter-site CV were between 5% and 10% for R1 and MT-maps. Although repeatability and reproducibility are recognized as essential for protocol development and implementation in many clinical trials (mentioned above), few studies have addressed the reproducibility of simultaneous mapping of quantitative magnetization transfer (qMT) pool size ratio (F-map), T1 relaxation time [s], R2* relaxation rate [s^{-1}], quantitative susceptibility map (QSM) [ppm], and myelin water fraction (MWF) maps at 7T. This is particularly important as many qMR maps are affected by field strength, and it is important to determine how they are repeatable in ultra-high fields. Therefore, in this chapter, we first introduce a clinically feasible multi-parametric qMR protocol at 7T to generate the maps of R2* (1/T2*), QSM, MWF, qMT, and T1 relaxation maps. Then, we show the reproducibility of multi-parametric quantitative characterization of the brain's physiological parameters using vendor-available sequences in a clinically acceptable scan time (30 minutes). The approach requires no dedicated sequence development and is easy to implement at any imaging site. The scan-rescan protocol was

applied to 8 subjects. We generated 3D maps of qMT F-map, T1, MWF, R2*, and QSM. The reproducibility and reliability of the acquired measurements were reported using Intra-class correlation coefficient (ICC) [147], coefficient of variation (CV), Bland-Altman plots, and the corresponding bias and variability using both voxel-wise and ROI-based analysis in 4 regions of interest (ROIs): caudate (Ca), putamen (Pu), white matter (WM), and gray matter (GM).

3.2 Materials and Methods

3.2.1 Theory

3.2.1.1 T2* and QSM mapping

T2* relaxation, a combination of spin-spin interactions and magnetic field inhomogeneity, was achieved using the VSF method that was discussed in depth in Chapter 2. Using the same mGRE data acquired for T2* mapping, QSM maps can be generated with no additional scan cost.

Quantitative Susceptibility Mapping (QSM) aims to reconstruct tissue magnetic susceptibility distributions from MRI phase data, but the process is fundamentally ill-posed due to the zero cone in the dipole kernel in k-space. Traditional methods such as TKD (Truncated K-space Division) [132], iLSQR (iterative Least-Squares) [148], and MEDI (Morphology Enabled Dipole Inversion) [133] have addressed this challenge by incorporating spatial priors, iterative solvers, and regularization constraints. However, these approaches often require manual parameter tuning, can be sensitive to noise, and are prone to streaking artifacts, especially in regions with strong susceptibility gradients. To overcome these

limitations, QSMnet was proposed by Yoon et al. [137, 149] as a deep learning-based framework that directly learns the mapping from the local field map to susceptibility, thereby bypassing the need to solve the dipole inversion equation explicitly.

3.2.1.2 MWF mapping

Myelin Water Fraction (MWF) mapping is a quantitative MRI technique that estimates the proportion of water trapped between the lipid bilayers of myelin, referred to as the "myelin water pool." This water compartment exhibits unique transverse relaxation properties that distinguish it from intra/extracellular water and cerebrospinal fluid (CSF), enabling its separation using multi-component T_2 relaxometry techniques [26, 139] . In multi-echo spin echo (MESE) acquisitions, the MR signal decay over successive echoes reflects a superposition of contributions from multiple water compartments: short T_2 (~10–40 ms): myelin associated water, intermediate T_2 (~40–200 ms): intra- and extracellular water, long T_2 (>1000 ms): cerebrospinal fluid, if present. This decay can be modeled as:

$$S(t) = \sum_{i=1}^{N} A_i e^{-\frac{t}{T_{2i}}} \qquad 3.1$$

Where A_i and T_{2i} represent the signal amplitude (proton density) and transverse relaxation time of the i^{th} compartment, respectively. The goal of multi-component T_2 relaxometry is to estimate the distribution A_i across a range of T_2 values, often referred to as the T_2 spectrum (Figure 3.1).

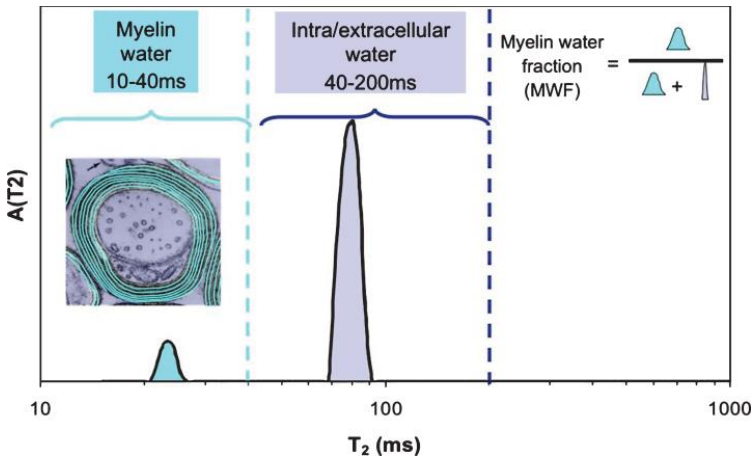

Figure 3.1: The histogram of the T2 values in the myelin water pool and the intra/extracellular water [138]

MWF is defined as the ratio of the faster decaying myelin component (T2 < 40 ms) to the total signal:

$$MWF = \frac{\sum_{T_{2i} \leq 40\ \mathrm{ms}} A_i}{\sum_{i=1}^{N} A_i} \qquad 3.2$$

This 40-ms cutoff is based on histological and in vivo validation studies indicating that water trapped within myelin bilayers relaxes more rapidly due to its restricted environment.

3.2.1.3 qMT

Quantitative magnetization transfer derived from selective inversion recovery (SIR) acquisitions allows parameter map estimation, including the myelin-sensitive macromolecular pool size ratio (*PSR* or *F* maps) [150]. The schematic of SIR acquisition for qMT mapping is shown in Figure 3.2.

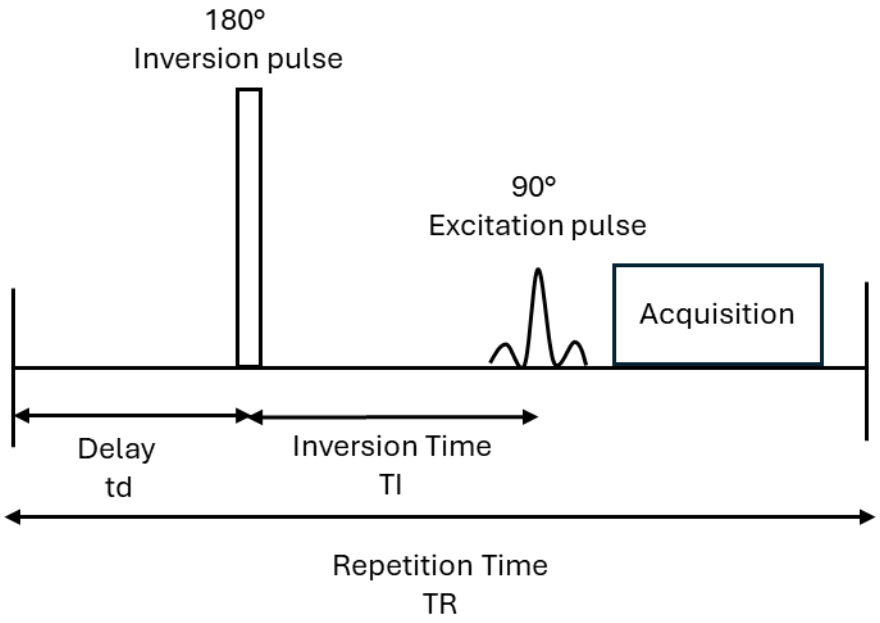

Figure 3.2: The schematic of the SIR pulse sequence used for qMT mapping. The inversion pulse is a simple rectangular pulse with no gradients.

In our SIR-qMT implementation, the selective inversion pulse is applied to the free water pool, and images are acquired at multiple inversion times (TIs) to sample the longitudinal recovery. The bound pool, which cannot be effectively inverted due to its extremely short T_2 (~10–50 μs), is assumed to remain near equilibrium. However, the recovery of the free pool is altered by magnetization exchange with the bound pool, resulting in a slower and non-monexponential inversion recovery curve. This recovery is modeled using the two-pool Bloch-McConnell equations, which account for longitudinal relaxation and bidirectional exchange between the pools. Fitting this model to the measured recovery curve yields quantitative parameters such as the pool size ratio (F) and exchange rate (k), which reflect macromolecular content and myelin density [94, 109]. Numerical solution to the Bloch-McConnell equations for two-pool systems under SIR conditions allows estimating the PSR (F), longitudinal relaxation of the free pool, and exchange rates [151].

3.2.1.4 T1-mapping

Inversion recovery (IR) methods are a gold standard for T_1 mapping due to their direct sensitivity to longitudinal relaxation. When performing SIR-based quantitative magnetization transfer (qMT) imaging, multiple images are acquired at varying inversion times (TIs) following selective inversion of the free water pool. These data inherently capture the T_1 recovery curve of the free pool and can be repurposed, without additional acquisition time, to generate a voxel-wise T_1 map [109, 152]. Assuming negligible exchange or by ignoring the contribution of the bound pool, and for TR > $5T_1$, the recovery of free pool magnetization can be modeled as:

$$S(TI) = M_0\left(1 - 2e^{\frac{-TI}{T_1}}\right) \quad 3.3$$

Where $S(TI)$ is the signal at a given inversion time, M_0 is the equilibrium magnetization, and T_1 is the longitudinal relaxation time. In practice, the following three-parameter signal model is used to account for the baseline signal offsets:

$$S(TI) = A - Be^{\frac{-TI}{T_1}} \quad 3.4$$

3.2.2 Multiparametric Mapping Protocol (MPM)

3.2.2.1 MPM Data Acquisition

In this section, we introduce a pipeline for data acquisition and processing to generate quantitative multi-parametric maps of the brain to enable a comprehensive characterization

of its properties. We use data from the standard MRI BEAT sequence at 7T Terra. X scanner to generate the quantitative maps. Using standard and clinically available sequences eliminates the need for more advanced sequence programming that may not be readily available at every medical center. We then analyze the reproducibility of the implemented protocol in section 3.2.3.

All the experiments were performed using Siemens 7T Terra. X with 8Tx/32Rx head coil. The imaging parameters for qMT and T1 mapping were a 3D BEAT sequence: in-plane resolution=0.7×0.7 mm, slice thickness mm, 16 slices, Inversion Times TIs: [15,25,150,200,280,400,1500,2000,3000] with TRs: [4215,3290,3500,3700,2980, 3500,3500,5500,3500]. The imaging parameters for T2*, QSM, and frequency mapping were a 3D BEAT sequence with monopolar readout. In-plane resolution 0.5×0.5 mm^2, slice thickness=1 mm, number of slices: 48, Flip angle 9˚. TE (0) = 1.51 ms, number of echoes 9, echo spacing: 2.57 ms, and TR: 30 ms. The protocol was tested on a single subject. MWF mapping is done with a spin echo sequence. All post-processing was done in MATLAB.

3.2.3 Reproducibility Analysis through Scan-Rescan Experiment

After successful implementation of our quantitative MPM protocol, enabling the simultaneous generation of T2*, QSM, T1, MWF, and qMT F map, we applied this protocol in a scan-rescan study involving healthy volunteers to assess scan-rescan reproducibility and parameter stability. These results help establish the feasibility and reliability of this protocol for future clinical and research studies.

Reproducibility of the multi-parametric qMR mapping protocol was tested on 8 participants. All the experiments were performed on a Siemens 7T Terra. X with 8Tx/32Rx head coil.

Eight healthy participants participated in the study. The participants had no history of neurological diseases or psychiatric disorders. All participants gave their written informed consent, and the Institutional Review Board of Auburn University approved the study. All participants (5 males / 3 females) were scanned twice. The participants were removed from the scanner and asked to walk around, use the restroom, or relax for at least five minutes between the two scans. B_0 shimming was performed for all scans using the vendor's default shimming routines.

3.2.3.1 Scan-Rescan Experiment for Reproducibility Analysis

High-resolution structural images were acquired using 3D T1-weighted (T1w) magnetization-prepared rapid gradient echo (MPRAGE). The imaging parameters were TR = 4000 ms, TE = 3.47 ms, TI = 1500 ms, 4° flip angle, bandwidth = 200 Hz/pixel, echo spacing = 8.12 ms, 0.6×0.6×0.8 mm^3 resolution, and 256 slices per slab. Acceleration mode was set to compressed sensing with a total factor of 6.5 and 32 phase encoding reference lines, resulting in a total acquisition time (TA) of 3:55 min.

For qMT and T1 mapping, we used inversion recovery GRE (T1-prepared 3D BEAT sequence) with in-plane resolution of 0.7×0.7 mm, slice thickness: 5 mm, 16 slices, inversion times TI: [15, 25, 150, 200, 280, 400, 1500, 2000, 3000] (ms), repetition time TR: [4215, 3290, 3500, 3700, 2980, 3500, 3500, 5500, 3500] (ms), with 5° flip angle, TE: 1.27 ms, and 63 segments were acquired per TI. The acquisition time for each 3D data set at a given TI was approximately 1 minute using a GRAPPA acceleration factor of 3 with 24 reference lines. TI and TR were selected based on previously reported studies [153, 154], which were modified during our pilot experiments based on the sequence parameter limitations and the

quality of the resulting qMT and T1 maps. A subset of TIs was selected ([25,150,400,3000]) after a comparative analysis of the quality of the generated maps to suggest the potential of reducing scan time when only T1 mapping is desired.

A 3D multi-echo GRE sequence was acquired for R2* and QSM mapping with a monopolar readout. In-plane resolution 0.5×0.5 mm^2, slice thickness=1 mm, number of slices: 48, flip angle: 9˚, TE1 =1.51 ms, number of echoes 9, echo spacing: 2.57 ms, TR: 30 ms, with factor 2 GRAPPA acceleration and 24 reference lines. TA: 3:15 min.

MWF mapping data was acquired with a multi-echo spin echo (MSE) sequence with a low SAR RF pulse type. The acquisition parameters were 9 slices, 2×2×6 mm^3 resolution, 32 echo times, TE1: 10 ms, echo spacing 10 ms, TR 9 s, acceleration using GRAPPA with a factor of 3 with 24 reference lines, and TA: 7:48 min.

3.2.3.2 Data Processing

All images were reconstructed online on the scanner, and DICOM images were transferred for offline post-processing in MATLAB (MathWorks, Natick, MA). Images were converted to NIFTI for further processing. All the 3D T1w images were processed in FreeSurfer 7.3.2 [155, 156] for brain segmentation (recon-all command). Using FreeSurfer's color lookup table (LUT), the following ROIs were extracted from the 3D label image to be used in statistical analysis. For T1, R2*, and QSM maps, left Caudate (Ca): 11, left Putamen (Pu): 12, left hemisphere WM (lh-WM): 2, and left hemisphere cortical GM (lh-GM) (index values between 1000 and 1220), were extracted for the analysis. See Figure 3.3. Note that the same statistical analysis can be applied to the right hemisphere, which was not considered in this work. Limiting the number of data points in this way will facilitate data representation in the

form of scatter plots, as illustrated in the voxel-wise analysis in the results section. Moreover, the objective is to test the reliability of the qMR maps when the same region is selected, which can be located in either the left or right hemisphere. For MWF and the pool size ratio F-map, however, the whole WM (LUT indices: 41 & 2) was considered as the ROI. This is because MWF and F-maps are often reported in the myelin-rich whole WM in many neurological disorders [31, 157].

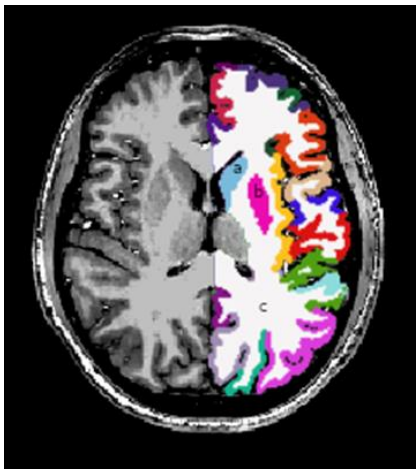

Figure 3.3: Representative anatomical image and the selected ROIs for reproducibility analysis from the left hemisphere: **(a)** Caudate, **(b)** Putamen, **(c)** WM, and FreeSurfer's color-coded cortical GM.

Before generating each quantitative map, the 3D T1w images were co-registered to the first magnitude image of the corresponding dataset using SPM12 (Statistical Parametric Mapping, https://www.fil.ion.ucl.ac.uk/spm/software/spm12/) with default parameters. We used this co-registered anatomical image (which now has the same number of slices as the corresponding quantitative maps) to crop and resample the FreeSurfer's 3D label image to the target quantitative map dimensions using the segmentation tool in ITK-SNAP 4.0.2[158] (www.itksnap.org).

qMT data processing: Before generating the qMT and T1 maps, all acquired images (TI: 15 to 3000 ms) were aligned with the first image (TI: 15 ms) with SPM12 realign (estimate & reslice) with default parameters. In addition, the rescan images were coregistered (estimate & reslice with default parameters) to the scan image space. T1 maps and qMT F-maps were generated using the qMRLab [151]. First, we generated a T1-map using Inversion recovery T1-relaxometry with TIs: [25,150,400,3000] and TR: 3500 ms. This T1 map was used to create a mask by thresholding it to T1 values less than 1400 ms to explicitly focus on voxels in the WM prior to qMT fitting. This helps in increasing the qMT fitting speed and accuracy. This threshold was set as it has been reported to be an inclusive higher limit for T1 values in WM, both at 3T [159] and 7T, where the mean T1 value is reported to be 1284 ± 22 ms in WM and 2065 ± 69 ms in GM using the IR method [160]. This mask further removes CSF from the fitting procedure to avoid direct saturation effects that might differ from tissue due to the longer T2 and the zero MT. Furthermore, a T1 map was used to generate the masks as it is inherently co-registered with the qMT maps and avoids further registration and alignment. QMRLab's qmt-sirfse method was used to generate the F-maps using all TI and TRs (https://qmrlab.readthedocs.io/en/master/qmt_sirfse_batch.html). The above-mentioned generated mask was applied while fitting. Both rescan T1 and F maps were further registered into scan space using symmetric normalization (SyN) [161] with cross correlation as the metric (SyNCC) implemented in Advanced Normalization Tools in R (ANTsR v0.5.7.6, https://github.com/ANTsX/ANTsR?tab=readme-ov-file). The T1 and F values were extracted in the 4 ROIs and thresholded to be between $0.01 < F < 0.4$ for the F map and $800 < T1 < 3000$ ms to avoid outliers affecting statistical analyses.

R2* and QSM data processing: Quantitative R2* maps were generated using VSF

implemented in MATLAB to correct for the background field inhomogeneity artifact. To generate the QSM maps, we used the Chisep toolbox (https://github.com/SNU-LIST/chi-separation/), which takes 4D magnitude and phase data as input parameters. Phase images underwent a sequential process of phase unwrapping, background-field removal, and dipole inversion. We used Laplacian (STI Suite Version 3.0 https://people.eecs.berkeley.edu/~chunlei.liu/software.html) for phase unwrapping with a 12 isotropic pad size. Then we used V-SHARP [162] with a spherical mean value (SMV) of 12 to remove the background field. QSMnet was then used to solve the inverse field-to-susceptibility problem. Both rescan R2* and QSM maps were registered to the same space using SyNCC. The R2* and QSM values were extracted in the 4 ROIs and thresholded to be between 3<R2*<80 1/s for the R2* map and -0.1<QSM<0.1 ppm to avoid outliers affecting statistical analyses. The thresholds were selected empirically from data histograms, considering the expected ranges of values.

MWF data processing: Scan and rescan images were realigned and registered into the same space before generating the maps (as explained in the qMT section). The non-parametric T2 relaxometry method with extended phase graph (EPG) correction for the stimulated echoes was done using the multicomponent-T2 toolbox [163] (Version 0.3, https://github.com/ejcanalesr/multicomponent-T2-toolbox). This toolbox estimates the T_2 distribution from MESE data by solving a regularized non-negative least squares (NNLS) problem:

$$\min \|S - KA\|^2 + \lambda R(A) \qquad 3.5$$

Where S id the observed signal, K is the dictionary of exponential decays over a predefined set of T_2 values, λ is the regularization weight, and $R(A)$ is the regularization term. A is the T_2 distribution to be estimated. We used the InvT_2 penalty term that considers the non-equidistant partition of the T_2 grid with the L-curve criterion to estimate the optimal regularization weight. The myelin T2 cutoff was set to 40 ms, and total variation denoising (TV) was applied. Further nonlinear registration was applied using SyNCC on the generated maps. This additional registration step may help increase reproducibility by limiting misregistered voxels that might negatively affect the analyses. The resulting maps were then masked using the FreeSurfer's WM labels (indices 2 & 41) eroded by 4 pixels to report the values in the central regions of WM away from edges and thresholded not to exceed 0.6.

3.2.3.3 Statistical Analysis

In voxel-wise analysis, the value of the qMR maps in each voxel during the scan and rescan experiments was considered in the statistical analysis. In the ROI-based analysis, the mean value of each map in each of the extracted regions was considered for comparison and statistical analysis between scan and rescan measurements. Therefore, statistical metrics such as ICC, Pearson's correlation (r), bias, and variability were averaged over subjects and reported in voxel-wise analysis (See **Table**). On the other hand, the ROI-based analysis considers the mean qMR values in each region, and therefore, the statistical metrics (ICC, CV, etc.) do not need to be averaged over subjects, as each subject is considered in the statistical analysis. The ICC and CV between scan and rescan were calculated for the generated maps in the selected ROIs. We used the A-1 type ICC metric to calculate the degree of absolute agreement among measurements and reported the upper and lower confidence intervals for each map. The Bland-Altman was also plotted to analyze the degree

of agreement between the measurements and to report the corresponding bias and variability in each case. We considered the variability (Var.) to be the upper minus lower limits of agreement (LOA) in the Bland-Altman plot to understand the width to which the parameter is confined. We performed a voxel-wise linear regression analysis comparing scan and rescan data, including the Pearson's regression coefficient (r), regression slope, and intercept. A two-sample t-test (ttest2 in MATLAB) at the 5% significance level with default parameters ('both' tails assuming 'equal' variances) was performed along with the Cohen's effect size value to assess the difference between scan and rescan in both voxel-wise and ROI-based analyses. The average of the mean qMR values in each ROI from the 8 subjects was also reported in a whisker plot along with the interquartile range: median, data range of values across subjects, and possible outliers. A representative difference map (scan minus rescan) was also plotted to depict the voxel-wise differences in each quantitative map (Diff. map).

3.3 Results

Figure 3.4 shows the quantitative T1 maps (a) and quantitative F maps from quantitative magnetization transfer mapping using Inversion recovery data. Figure 3.5 shows the BEAT magnitude images (a), T2* maps corrected for background field inhomogeneity with Voxel Spread function (VSF) (b), Quantitative Susceptibility Maps (QSM) (c), and frequency maps (d).

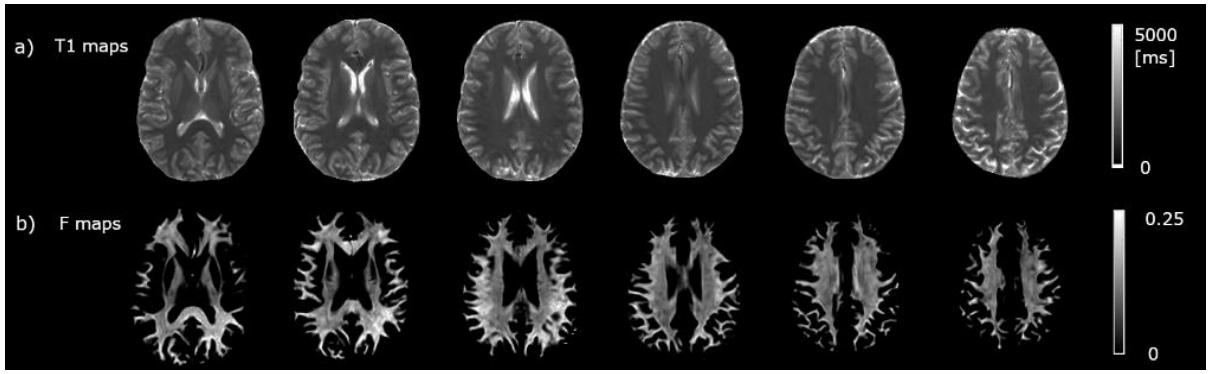

Figure 3.4: Representative quantitative **(a)** T1 and **(b)** F maps from the MPM protocol from a single subject in different slices.

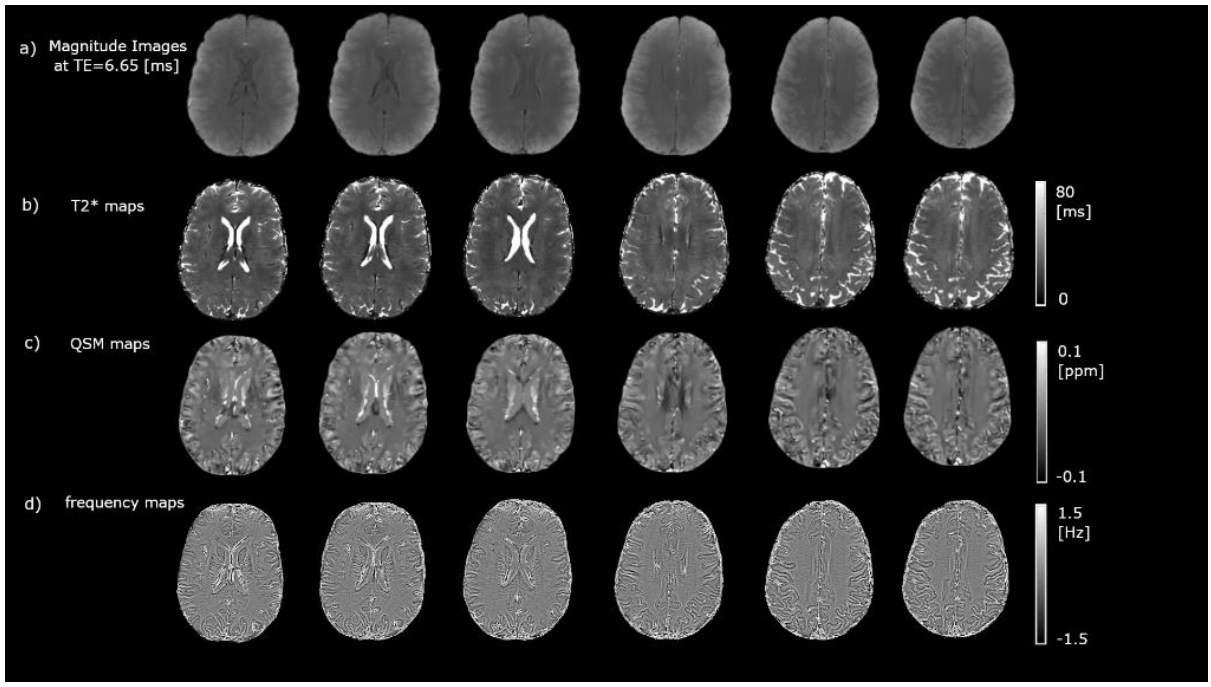

Figure 3.5: Representative **(a)** magnitude, **(b)** T2*, **(c)** QSM, and **(d)** frequency maps from the MPM protocol from a single subject in different slices.

Our results show the feasibility of multiparametric quantitative MR imaging of the brain at 7T Terra. X scanner using the clinically available 3D BEAT sequence. The maps generated enable a comprehensive characterization of tissue properties and might prove helpful in clinical studies.

A representative example of the generated T1, F, R2*, QSM, and MWF maps in a single subject is shown in Fig. 3.6a-e, respectively. Through a visual inspection, scan and rescan maps do not show extremely striking differences, as seen in the difference map (Diff), which is zoomed to 10 times the original scaling.

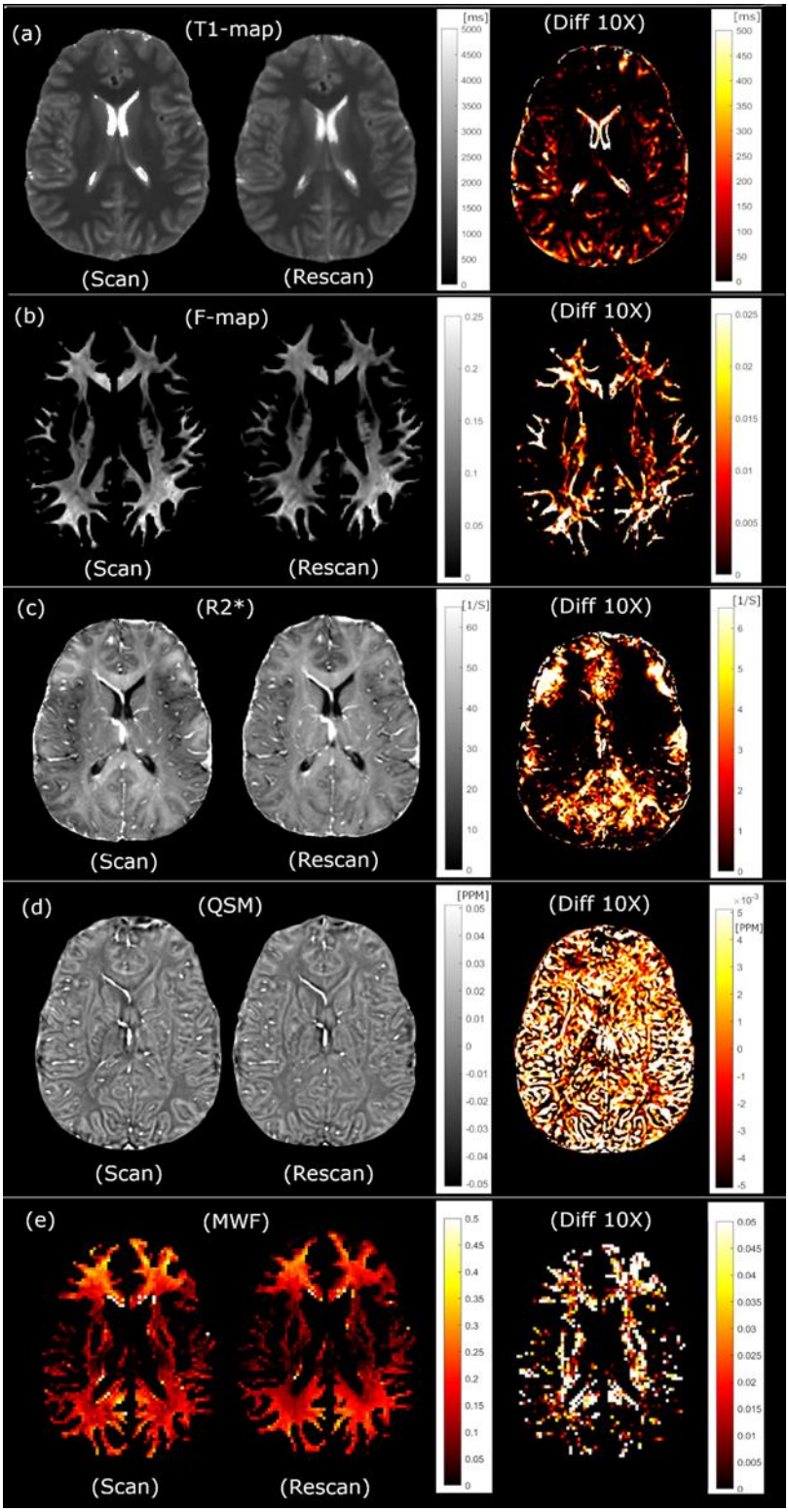

Figure 3.6: Representative quantitative MRI maps in scan and rescan experiments and the corresponding difference map (Diff) in a single subject: **(a)** T1-map (using all TIs), **(b)** qMT F-map, **(c)** R2*, **(d)** QSM, and **(e)** MWF maps. The difference map is zoomed in (10x).

Rescan maps are registered to the scan space using nonlinear registration (SyNCC) in ANTsR.

3.3.1 Voxel-wise analysis

T2* relaxation Figure 3.7 shows the voxel-wise correlation analysis results from a single subject T1 map, along with the regression line, slope, intercept, and Pearson r correlation values in **a)** Caudate, **b)** Putamen, **c)** lh-WM, and **d)** lh-GM. The corresponding Bland-Altman plots, the mean difference (bias: dashed red line), and the limits of agreement (LOA = mean difference ± 1.96 ∗ SD) are also shown (dashed green lines). Similar voxel-wise analysis results are depicted in Figures 3.8-3.10 for R2*, QSM, F-, and MWF maps, respectively.

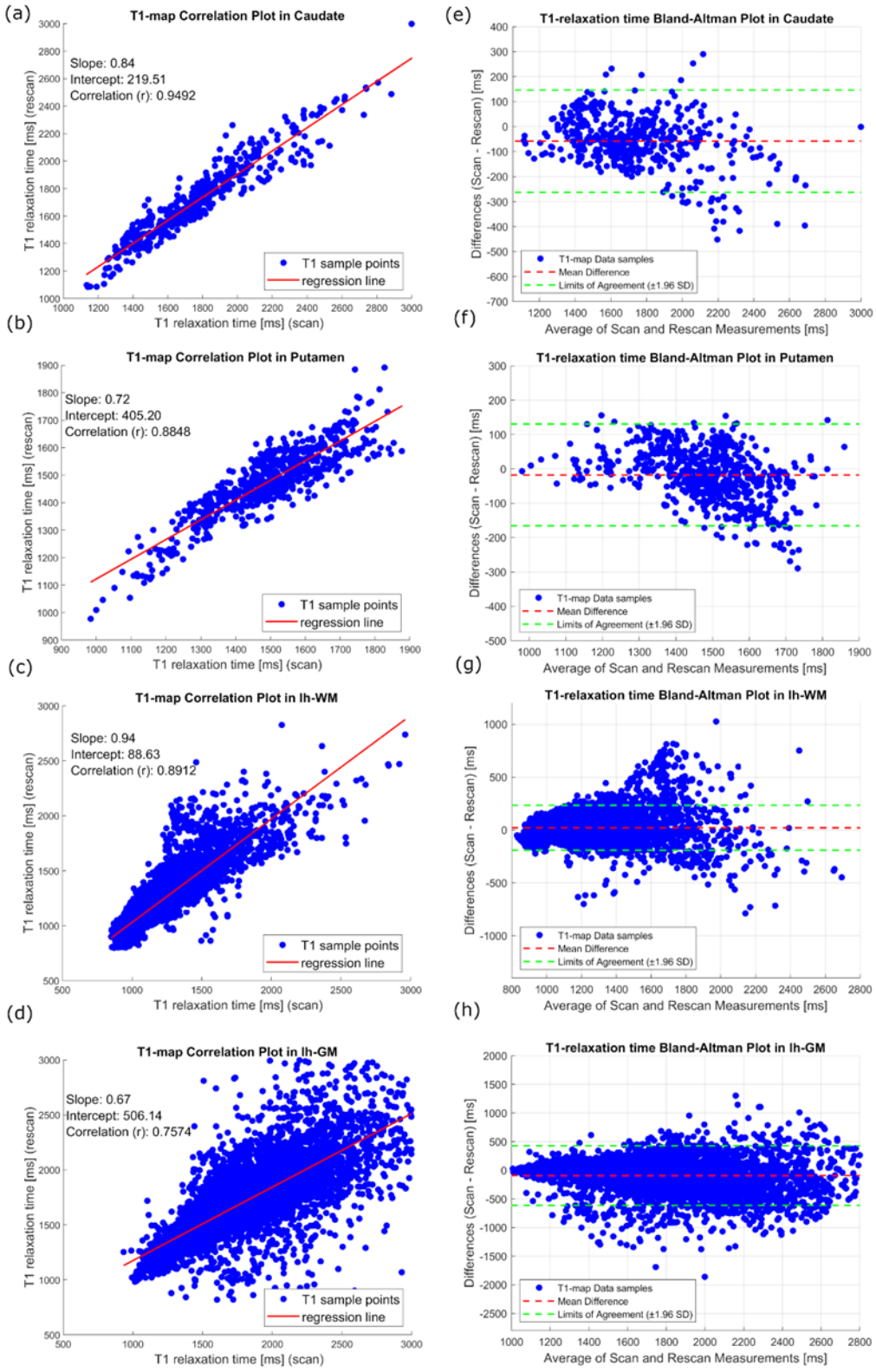

Figure 3.7: (a-d) T1-map correlation plots in Caudate, Putamen, lh-WM, and lh-GM and the corresponding Bland-Altman plots **(e-h)** in a single subject. The regression line is shown in solid red. TIs: [25,150,400,3000] and TR: 3500 ms.

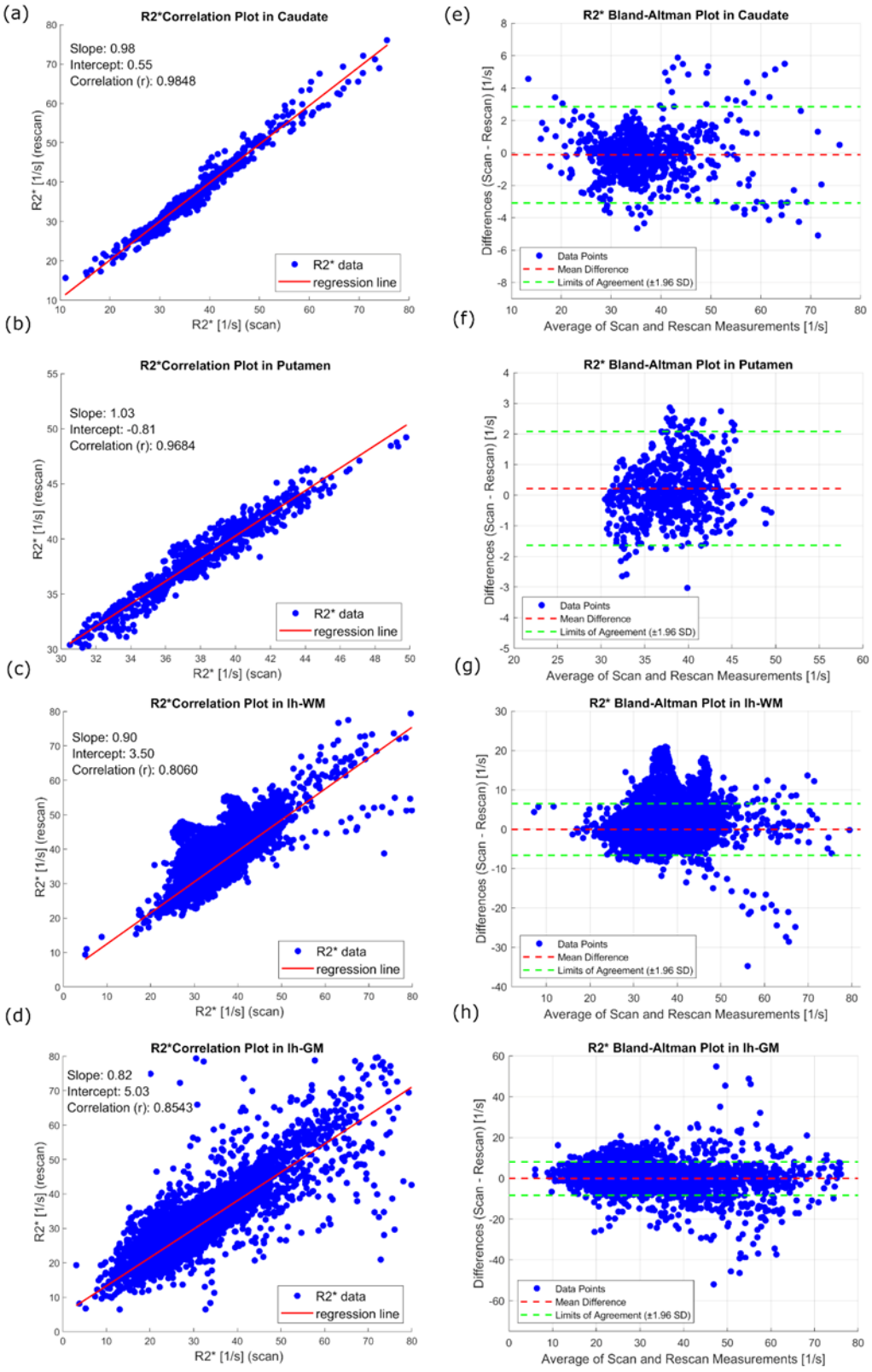

Figure 3.8: (a-d) R2* map correlation plots in Caudate, Putamen, lh-WM, and lh-GM and

the corresponding Bland-Altman plots (e-h) in a single subject. The regression line is shown in solid red.

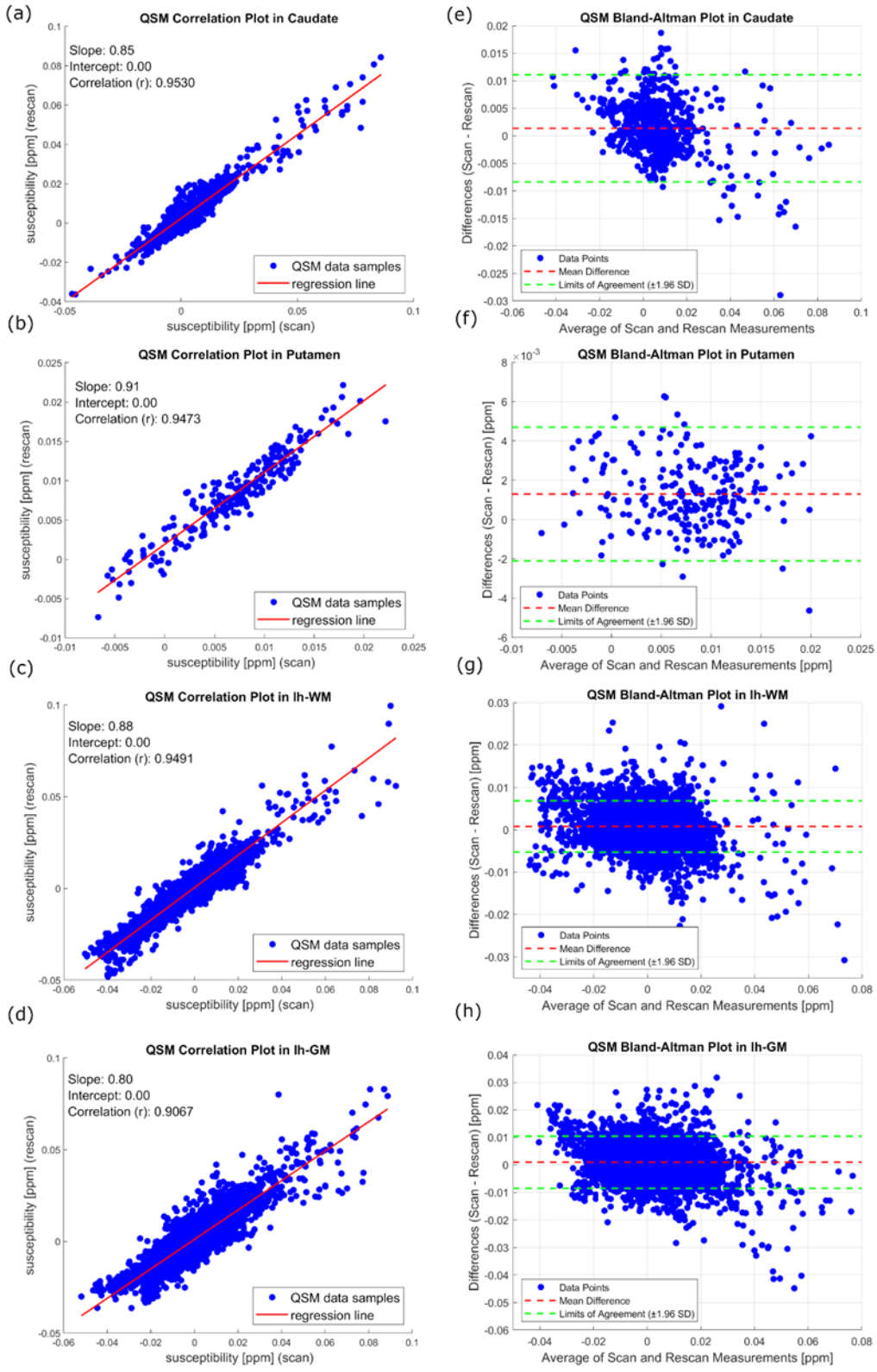

Figure 3.9: (a-d) QSM map correlation plots in Caudate, Putamen, lh-WM, and lh-GM and the corresponding Bland-Altman plots **(e-h)** in a single subject. The regression line is shown in solid red.

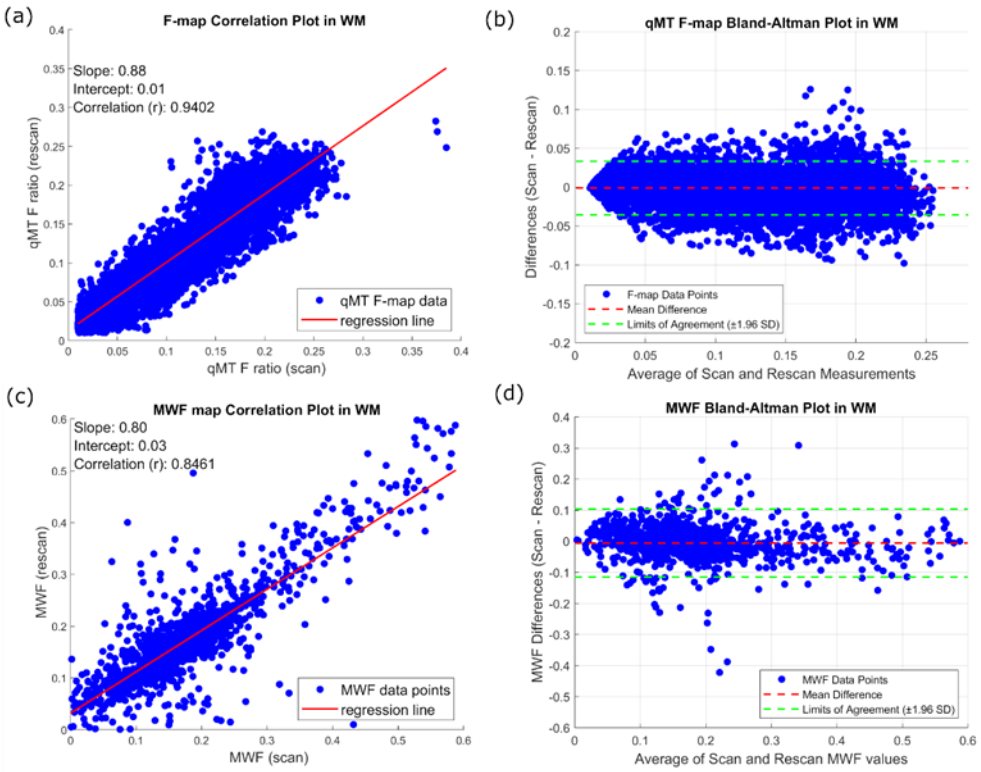

Figure 3.10: (a-b) F-map, and **(c-d)** MWF map correlation and Bland-Altman plots in WM in a single subject. The regression line is shown in solid red.

We tabulated the average behavior of the voxel-wise analysis results across all 8 subjects in Table 3.1. The reported metrics in this table are averaged over all 8 subjects. The voxel-wise analysis results for each individual subject, along with the t-test results and effect sizes, are presented in the supplementary materials section (**Tables A1-A3**).

Table 3.1: Voxel-wise analysis of qMR maps in selected ROIs. The reported values are the mean ± SD of each metric (obtained by considering each voxel's data as samples) over all 8 subjects. R: Pearson's correlation, abs (Bias): absolute value of the mean differences in the Bland-Altman plot, Var.: variability as the width of the upper minus lower LOA.

qMR map	Metric	ROI			
		Ca.	Pu.	lh-WM	lh-GM
T1 [ms]	ICC	85.63 ± 14.07	77.75 ± 11.95	86.5 ± 5.45	77.75 ± 5.63
	r	91.63 ± 7.17	80.38 ± 11.88	88 ± 4.9	79 ± 4.28
	abs (Bias)	75.86 ± 75.14	21.64 ± 7.79	31.99 ± 12.95	53.56 ± 42.82
	Var.	466.58 ± 191.76	267.66 ± 70.97	419.81 ± 121.54	945.76 ± 161.71
R2* [1/s]	ICC	91.63 ± 7.27	79.88 ± 16.06	79 ± 7.6	81.38 ± 4.63
	r	93.88 ± 5.49	86.25 ± 9.93	80.88 ± 6.22	81.38 ± 4.63
	abs (Bias)	0.96 ± 0.97	1 ± 1	1.19 ± 0.92	0.38 ± 0.33
	Var.	14.68 ± 10.45	10.21 ± 6.92	15.92 ± 6.61	21.25 ± 6.19
QSM [ppb]	ICC	87.63 ± 7.42	89.88 ± 7.12	88 ± 6.95	83.25 ± 8.4
	r	91 ± 5.95	94 ± 3.59	89.13 ± 6.56	84.25 ± 8.56
	abs (Bias)	0.18 ± 1.4	1.6 ± 1.39	0.69 ± 1.17	0.75 ± 0.94
	Var.	14.68 ± 10.45	10.04 ± 3.84	19.25 ± 6.95	30.38 ± 10.51
qMR map	Metric	WM			
F	ICC	92.5 ± 3.51			
	r	93.63 ± 2.26			
	abs (Bias)	0.004 ± 0.004			
	Var.	0.07 ± 0.02			
MWF	ICC	81 ± 4.34			
	r	82.88 ± 4.05			
	abs (Bias)	0.017 ± 0.009			
	Var.	0.24 ± 0.03			

3.3.2 ROI-based analysis

Table 3.2 shows the results of the ROI-based analysis, where the average value of the qMR is considered as a data sample in statistical analysis (making 8 samples for the scan to be compared with 8 samples from the rescan). ROIs CV, ICC, p-, and Cohen's d-values are tabulated. For the pairwise CV% of each subject, refer to the supplementary materials (Table A4). Box and whisker plots of the mean qMR maps in each ROI are shown in **Figures 3.11 to 3.13** for R2*, QSM, T1, F, and MWF, respectively. Each horizontal red solid line is the average of the corresponding mean qMR value inside the ROI, averaged across all subjects. The box plot is based on 8 data points from 8 different subjects. The dashed horizontal lines are the median values for the scan (blue) and rescan (red) quantitative maps.

Table 3.2: ROI-based analysis of qMR maps in selected ROIs. ICC, p, and abs (d) values are obtained using the mean qMR in the selected ROI from each subject, resulting in 8 data samples in the scan and 8 data samples in the rescan to be considered in the analyses. CV% is the average CV of the pair-wise CV of all 8 participants (see supplementary material **Table A4**).

qMR map	Metric	ROI			
		Ca.	Pu.	lh-WM	lh-GM
T1 [ms]	ICC (CI)	61 (0 , 90)	98 (90 , 100)	81 (28 , 96)	76 (25 , 65)
	CV %	3.06	1.13	2	2.21
	p	0.27	0.99	0.42	0.56
	abs (d)	0.53	0.01	0.39	0.28
R2* [1/s]	ICC (CI)	86 (46 , 97)	97 (84 , 99)	80 (33 , 96)	96 (83 , 99)
	CV %	1.78	1.83	2.21	0.85
	p	0.88	0.98	0.53	0.79
	abs (d)	0.07	0.01	0.3	0.13
QSM [ppb]	ICC (CI)	94 (69 , 99)	91 (39 , 98)	98 (88 , 100)	93 (61 , 99)
	CV %	46.37	33.3	29.65	55.59
	p	0.66	0.52	0.81	0.62
	abs (d)	0.21	0.31	0.12	0.24
qMR map	Metric	WM			
F	ICC (CI)	85 (39 , 97)			
	CV %	2.3			
	p	0.95			
	abs (d)	0.03			
MWF	ICC (CI)	64 (-9 , 93)			
	CV %	6.45			
	p	0.08			
	abs (d)	0.89			

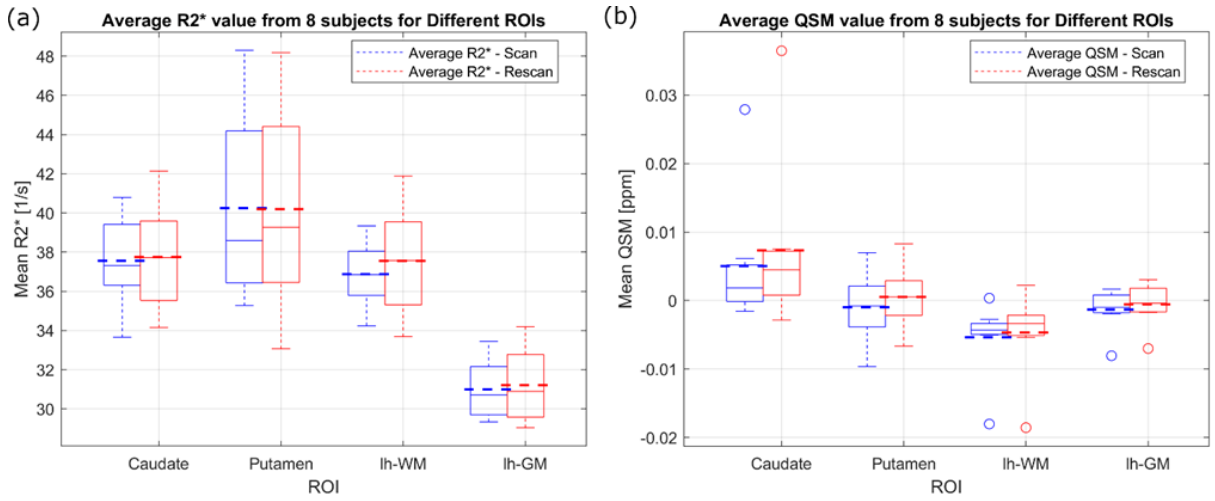

Figure 3.11: Mean **(a)** R2*, and **(b)** QSM values in each ROI in 8 subjects from scan (blue) and rescan (red) measurements. Dashed horizontal lines are the average over all 8 subjects in the scan (blue) and rescan (red). Box = interquartile range; bold horizontal lines = median; whiskers = data range of values across subjects. Circles = outliers, which is a subject that exceeded the range of (q1–1.5 × [q3–q1]; q3 + 1.5 × [q3–q1]), where q1 and q3 are the 25th and 75th percentiles of the mean qMR data, respectively.

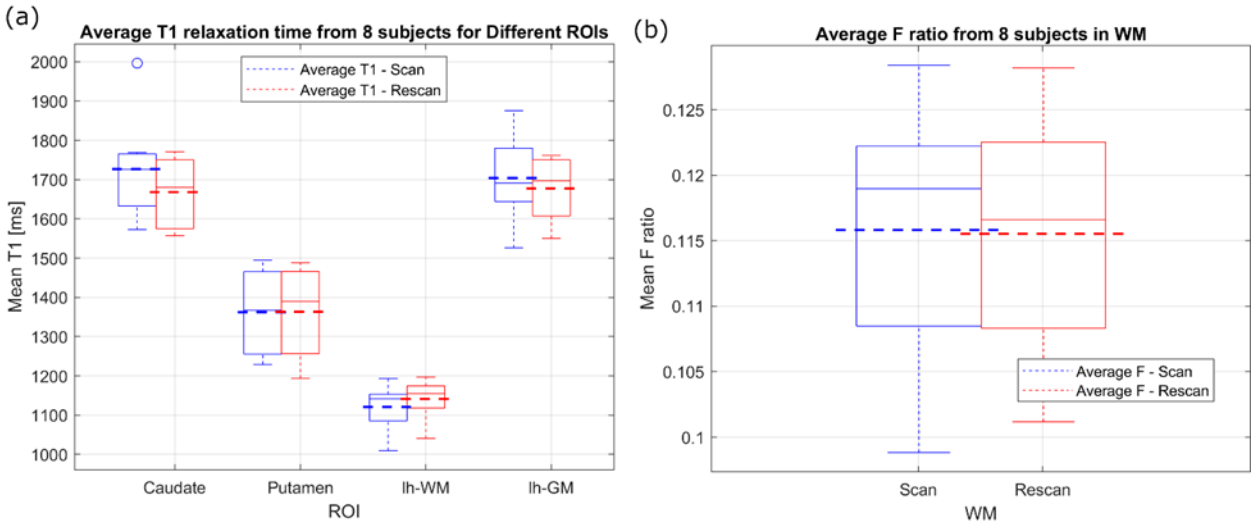

Figure 3.12: Mean **(a)** T1 and **(b)** F values in each selected ROI in 8 subjects from scan (blue) and rescan (red) measurements. Dashed horizontal lines are the average over all 8 subjects in the scan (blue) and rescan (red). Box = interquartile range; bold horizontal lines = median; whiskers = data range of values across subjects. Circles = outliers, which is a subject that exceeded the range of (q1–1.5 × [q3–q1]; q3 + 1.5 × [q3–q1]), where q1 and q3

are the 25th and 75th percentiles of the mean qMR data, respectively.

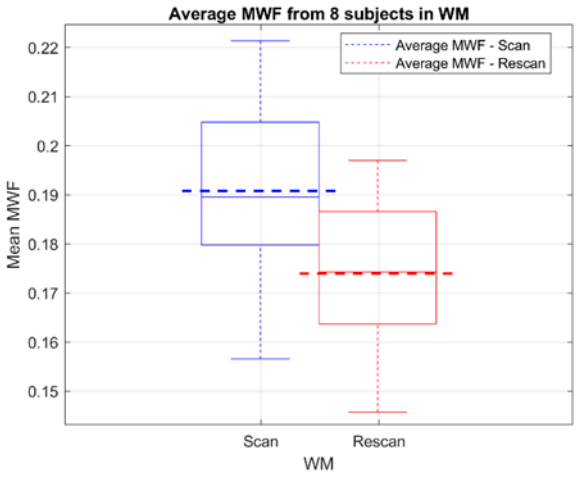

Figure 3.13: Mean MWF values in WM in 8 subjects from scan (blue) and rescan (red) measurements. Dashed horizontal lines are the average over all 8 subjects in the scan (blue) and rescan (red). Box = interquartile range; bold horizontal lines = median; whiskers = data range of values across subjects. Circles = outliers, which is a subject that exceeded the range of (q1–1.5 × [q3−q1]; q3 + 1.5 × [q3−q1]), where q1 and q3 are the 25th and 75th percentiles of the mean qMR data, respectively.

3.4 Discussion

In this chapter, we implemented a protocol for multiparametric quantitative mapping of the human brain using clinically available sequences in less than 30 minutes and assessed its reliability at 7T. Repeatability and reproducibility can be classified as poor for ICC values 50%, moderate for 50 <ICC< 75, good for 75<ICC<90, and excellent for values above 90, provided the 95% CIs are small [142]. In our voxel-wise analysis (Table 3.1), where the metrics were averaged over 8 subjects, our results showed good-to-excellent (75<ICC<100) reproducibility in all qMR maps in all the selected ROIs. Scan and rescan showed a high

Pearson's correlation (r>75) for all the qMR maps in all the chosen ROIs (see Figures 3.7-3.10 for a single subject). There was a slight absolute bias in each reported metric (see Table 3.1). When considering the whole WM, the qMT F-map outperformed MWF in ICC and correlation and showed less bias and variability than MWF.

In ROI-based analysis, where we averaged each qMR over the ROI and compared the resulting average qMR values between scan and rescan in all subjects, the following observations were obtained (Table 3.2): good-to-excellent reproducibility in all qMR maps in all the selected ROIs except for the T1 map in Caudate and MWF in WM that showed moderate ICC. To calculate the CV, we first calculated pairwise CV (Table S4) and averaged it over all subjects to get CV values in Table 3.2. The CV values were small, ranging from 0.85% to 6.45% across all qMR maps, except for the QSM, which had small values near zero that impacted the CV calculation. These high CVs are the result of the mean QSM values being close to zero, which results in a division by a small number [142].

By comparing the voxel-wise (Table S1-S2) and ROI-based t-test p-values (Table 3.2), it is seen that the average behavior of the qMR map over the ROI (ROI-based analysis) shows insignificant differences (P>0.05) between scan and rescan, while voxel-wise comparison between scan and rescan has smaller P values (P<0.05) in most of the selected subjects and ROIs. This can be due to misregistration errors, partial volume effect, or post-processing (such as thresholding) on each voxel. This could mean that ROI-based measurements might be a more reliable metric for longitudinal studies when t-statistics are considered, compared to monitoring each voxel value individually. However, this does not undermine the importance of monitoring qMR values in each voxel over time, as the effect sizes (d values)

reported for each subject in Tables A1 and A2 are too small, making the differences observed less practically significant.

We reported mean values of the qMR maps in the selected ROIs in box and whisker plots (Figures 3.11-3.13). There was a high degree of agreement between the average values of the mean qMR maps over all subjects (solid horizontal lines) in scan and rescan measurements.

Similar works have pursued multiparametric qMR mapping of the human brain at 7T. Meter et. al. introduced a novel sequence, multi-echo MP2RAGE, capable of generating simultaneous maps of T1, T2*, and QSM in 19 minutes [141]. The group average results reported for Ca., Pu. And WM in their work is 1441±34, 1659±36, 1219±30 for T1 (ms), 27.4 ± 1.1, 33.2 ± 1.9, 25.85 ± 0.8, for T2* (ms) and 26.3±3.4, -0.4±1.4, 7±2.3 for susceptibility (ppb), respectively. Comparing these results to Figure 3.11, our R2* values were comparable in Ca. and lh-WM, with slight overestimation in Pu. Our susceptibility values in Ca. showed a slight positive value (ppm), while Pu. had a negative or close to zero average QSM. Choi et al. reported QSM values close to 0.05 ppm in both left Ca. and left. Pu. With 0.834 (CI: 0.38, 0.964) and 0.734 (CI: 0.194, 0.939), respectively [164]. However, direct comparison between different QSM methods might not be desired as the reported susceptibility values differ in the selected reference and methods to calculate the susceptibility differences, rather than the bulk susceptibility [143]. Simultaneous reproducibility of QSM and R2* has also been studied at 7T with promising results [165]. Betts et al. have shown excellent reproducibility of QSM in Ca., and Pu. and have reported mean QSM values (ppm) for Ca., Pu., WM, and cortical GM to be 0.03 ± 0.0007, 0.014 ± 0.0008,

for Ca. and Pu., respectively, and between 0.04 to 0.03 ppm for WM, and between -0.01 to 0.015 ppm for cortical regions [166]. They have also shown excellent reproducibility for R2* in Ca. and Pu. With average R2* of 37±0.45 [1/s], and 44±0.56 [1/s], respectively. WM and cortical regions R2* were reported to be between 0 to 45 [1/s] and 0 to 70 [1/s], respectively [166]. Rua. at. al showed that R_2* values from the Auto-Regression on Linear Operations (ARLO) algorithm [130] followed the literature values closely for Ca. and Pu. With average values of 40 ms and ~50 ms, respectively. R2* in the left hemisphere has also been targeted, as is the case in our work, in the left Caudate and left Putamen with an average value of 46.4 ± 5.24 and 53.3 ± 7.6 [1/s], respectively [164].

Our T1-mapping results in Figure 3.12 differed from the values reported by Meter et. al [141], in smaller structures (Ca. and Pu.). As mentioned earlier, our T1 results, particularly in smaller structures (Ca. in Table 3.2), were not comparably reproducible as other qMR maps.

T-tests did not show any significant differences, as mentioned earlier in the ROI-based analysis, in any of the qMR maps. However, the MWF map showed relatively higher differences between the scan and rescan (Figure 3.13) with a P value of P = 0.08, which, compared to other qMR maps in this work, requires more careful consideration. A scan-rescan analysis of various regularization techniques and penalty functions in the non-parametric T2-relaxometry MWF tool used in our work can be found in [163]. Canales-Rodríguez et. al showed high reproducibility in the resulting MWF maps at 3T (with L-curve regularization outperforming others), above 90% Pearson's correlation, and smaller CV% compared to our values reported in Table 3.2. The lower relative reproducibility of MWF can be due to several factors: the processing geometric TE sampling might be ideal for MWF

mapping [167]. Fixed echo spacing might not be appropriate, as is the case in conventional MSE data with 10 ms fixed echo spacing. Furthermore, acquiring very short echo times that improve sensitivity to fast-decaying myelin signals is not feasible in a clinical setting. The advantage of using the parametric method, however, is that it generates MWF maps while accounting for stimulated echoes and applies effective spatial regularization to enhance the quality of the generated maps. Another confounding factor is SAR considerations and time-compensating acceleration. A higher SAR at 7T during MSE acquisition required a long TR, which was shortened with extreme acceleration; however, this might have compromised the reproducibility and quality of the MWF maps generated. Therefore, maybe for MWF mapping at 7T, switching to custom-programmed sequences might be a more reliable option. Other reliable biomarkers of myelin (e.g., qMT F map) can also serve as indicators of myelin content.

For qMT, we only focused on the WM as it shows significant pathological changes in several disorders [168, 169]. Scan-rescan reproducibility of the SIR qMT mapping has previously been implemented at 7T[114]. Dortch et. al.[114] reported mean value across selected WM ROIs to be (17.6 ± 1.3) %. The difference between these results and our results in Figure 3.12b may be due to the differences in the regions of interest (ROIs) covered, as we considered the entire white matter (WM) compared to selected smaller areas within the WM.

The choice of acquisition methods for each qMR mapping was based on several considerations, including SAR effects at 7T, acquisition time, and computational complexity. The parameters selected for data acquisition were limited to the scanner's default settings, with minimal flexibility in the chosen number of echo times, maximum

feasible echo time, minimum inversion time, echo spacing, and other parameters. One of the main impacts of this was observed on the MWF maps, as the SAR limitations required a higher TR, resulting in a longer acquisition with relatively lower reproducibility compared to other qMR maps generated in this work. Other techniques, such as myelin water imaging (MWI) using multi-echo gradient echo (mGRE) acquisition [27] might be more appropriate at higher fields. However, mGRE-based MWF mapping might not be feasible for clinical studies, as it requires custom sequence modification to enable optimized echo time sets for implementing non-linear least squares (NLLS) curve fitting to a complex 3-compartment signal model with 9 unknown parameters [27].

One limitation of the present work is the small sample size. While the results may not be suitable for drawing a general conclusion, they can be considered an approximate lower limit of discrepancies observed in longitudinal studies. A short resting time between scan and rescan sessions is another issue, as it does not accurately represent the long-term variation of both the brain and the scanner. While some statistical analyses can be performed on both hemispheres, we focused on the left hemisphere in the R2*, QSM, and T1 maps and reported the results for the selected ROIs in the left hemisphere. While this simplifies our report and representations, the qMR values in both hemisphere structures need to be considered and pooled over the whole slice for a more comprehensive report. Another limitation of our work is that we observed that the T1 map behavior is highly dependent on the selected ROI and cannot be considered reliable. We aimed to utilize the set of TIs and TRs already acquired for qMT mapping to generate an additional T1 map, thereby saving scan time. This limits the TIs considered for T1 mapping and could have impacted the moderate reproducibility of the T1 map. This calls for further optimizing the acquired data points for exclusive T1

mapping or using other more advanced T1 mapping techniques when feasible.

Conclusion: We have introduced and analyzed the reliability of a clinically feasible imaging protocol that enables multi-parametric quantitative mapping of the brain to access brain microstructural properties at 7T. This eases the process of comprehensive quantitative brain mapping, which might otherwise be hindered by the need for complex, custom sequence programming. The results of this work can also be further extended to analyze the degree of reproducibility between different vendors in different imaging sites or between different processing methods for each qMR parameter.

Chapter 4: Quantitative T2* Mapping with Multi-Echo Radial Stack-of-Stars Acquisition in Human Central Nervous System at 7T

4.1 Introduction

Quantitative MRI (qMRI) techniques, such as T2* mapping, quantitative magnetization transfer (qMT), and myelin water fraction (MWF) mapping, serve as effective methods for examining tissue microstructure and composition in vivo [105, 109, 139, 170, 171]. Typically, these techniques involve multiple acquisitions under different contrast-weighting conditions (for example, various echo times or inversion times) and depend on fitting biophysical models to estimate quantitative tissue parameters. Nevertheless, these acquisitions can be time-intensive and sensitive to movement, which can restrict their clinical and research uses. For example, qMT imaging can require at least nine inversion times, each taking over a minute, to ensure precise model fitting. Likewise, traditional Cartesian methods for T2* mapping usually demand prolonged scan durations to achieve high spatial and temporal resolution. To tackle these challenges, advanced non-Cartesian acquisition methods like radial [172], spiral [173], and rosette sampling [174] have become increasingly popular. Their strengths lie in tolerance to motion, efficient coverage of k-space, and their suitability for undersampled reconstruction techniques [175-177]. Among these methods, radial trajectories, especially the stack-of-stars approach, offer an effective balance between acquisition speed and motion

resilience, making them particularly suitable for imaging intricate anatomical areas such as the brain and spinal cord at ultra-high fields like 7 Tesla (7T).

In this chapter, we utilize a 2D multi-echo radial stack-of-stars technique for T2* mapping of the central nervous system. This method enables the creation of quantitative T2* maps for the human brain and cervical spinal cord, providing region-specific numerical values. The multi-echo radial acquisition facilitates simultaneous mapping across several echoes, offering improved resistance to motion artifacts and reducing scan time.

We first investigated the feasibility of generating T2* maps from single-shot k-space readouts in the human brain, which allows time-efficient acquisition. Then we image the spinal cord with single to multiple segments to assess how the quality of the images is affected by changing the number of kspace segments. From single-shot acquisition, which reduces scan time, to multi-shot segmented readout, which enhances SNR, we assess the resulting image quality and quantification performance. We also study the feasibility of compressed sensing (CS) reconstruction to enhance reconstruction when an undersampled kspace with a limited number of spokes is acquired in our radial acquisition.

This study is the first report to demonstrate the multi-echo high-resolution spinal cord radial stack-of-stars MRI with segmented acquisition and its application to brain and spinal cord T2* mapping at 7T. Particularly, this study aims to show that advanced multi-echo radial stack-of-stars can enable efficient, motion-insensitive, high-resolution T2* mapping in both the brain and spinal cord at 7T. The segmented and undersampling ability of this novel sequence makes it suitable for applications such as MR fingerprinting, where undersampled single-shot k-space acquisition is advantageous for saving time and enhancing contrast.

4.2 Materials and Methods

4.2.1 Radial Stack-of-Star (SoS) Pulse Sequence Design

A multi-echo golden angle radial stack-of-stars pulse sequence was implemented, which acquires the kx-ky plane along radial projections and Cartesian slice encoding. The 2D radial plane acquisition was segmented such that multiple radial spokes were acquired for each slice before switching to the next slice. The pulse sequence diagram implemented in Siemens IDEA software is demonstrated in Figure 4.1a. The multi-echo acquisition is repeated for each slice and each segment. For an acquisition with P radial spokes and N segments, each segment has P/N spokes acquired, and the acquisition is repeated for the next segment, resulting in a total acquisition time of N*M*TR. A representative segmented kspace with golden angle radial sampling (111.25°) [172] is shown in Figure 4.1b, where for an acquisition with N=3 segments and P = 12 spokes, 4 spokes are acquired in each segment for all slices to fill the kspace.

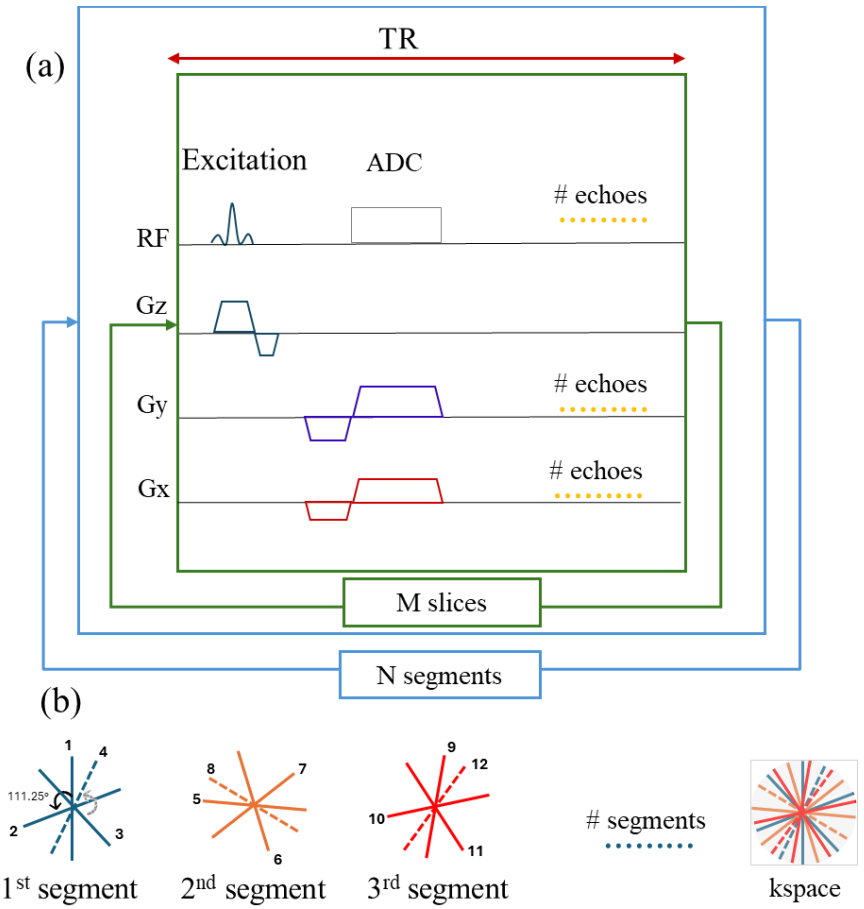

Figure 4.1: (a) Pulse sequence schematic and setup for the radial SoS acquisition, **(b)** kspace segmentation with golden angle radial sampling.

4.2.2 Data Acquisition

4.2.2.1 Brain Protocol

All the experiments were performed using Siemens 7T Terra. X with 8Tx/32Rx head coil. The sequence was tested on a single subject. Radial imaging parameters were: FOV=256 mm, readout=256, in-plane resolution=2×2 mm^2, slice thickness=5 mm, 5 slices, flip angle=15°, Golden angle sampling, number of spokes=128, 1 segment with TR=10 s. 11 echoes were acquired with TE1=2.40 ms, and dTE=3 ms.

4.2.2.2 Spinal Cord Protocol

All the experiments were performed using Siemens 7T Terra. X with an 8-channel spine coil (Rapid Biomedical GmbH). Radial imaging parameters were: FOV=240 mm, readout=448 pts, in-plane resolution=0.5×0.5 mm, slice thickness=5 mm, 9 slices, flip angle=15°, Golden angle sampling [172], number of spokes=1024, 512 spoke, 8 segments with TR=5.5s. Five echoes were acquired with TE1=2.40 ms, and dTE=4.02 ms.

The sequence was repeated with 512 radial spokes with different numbers of segments and TR as follows: = 1-segment (single shot/slice)/TR=11s, acquisition time=2 minutes; 4-segment/TR=5s, acquisition time=3:40 minutes; and 8-segment/TR=5s, acquisition time=7:20 minutes.

Standard clinical MEDIC images were also acquired at the same slice locations (see Figure 4.2). MEDIC combines 6 echoes into a single image. Parameters for the MEDIC images were: FOV=224, matrix=512 interpolated to a resolution of 0.2×0.2×5 mm^3, TE=15 ms, TR=500 ms, and flip angle=30^0. Standard Neck Bo shimming was performed for all scans.

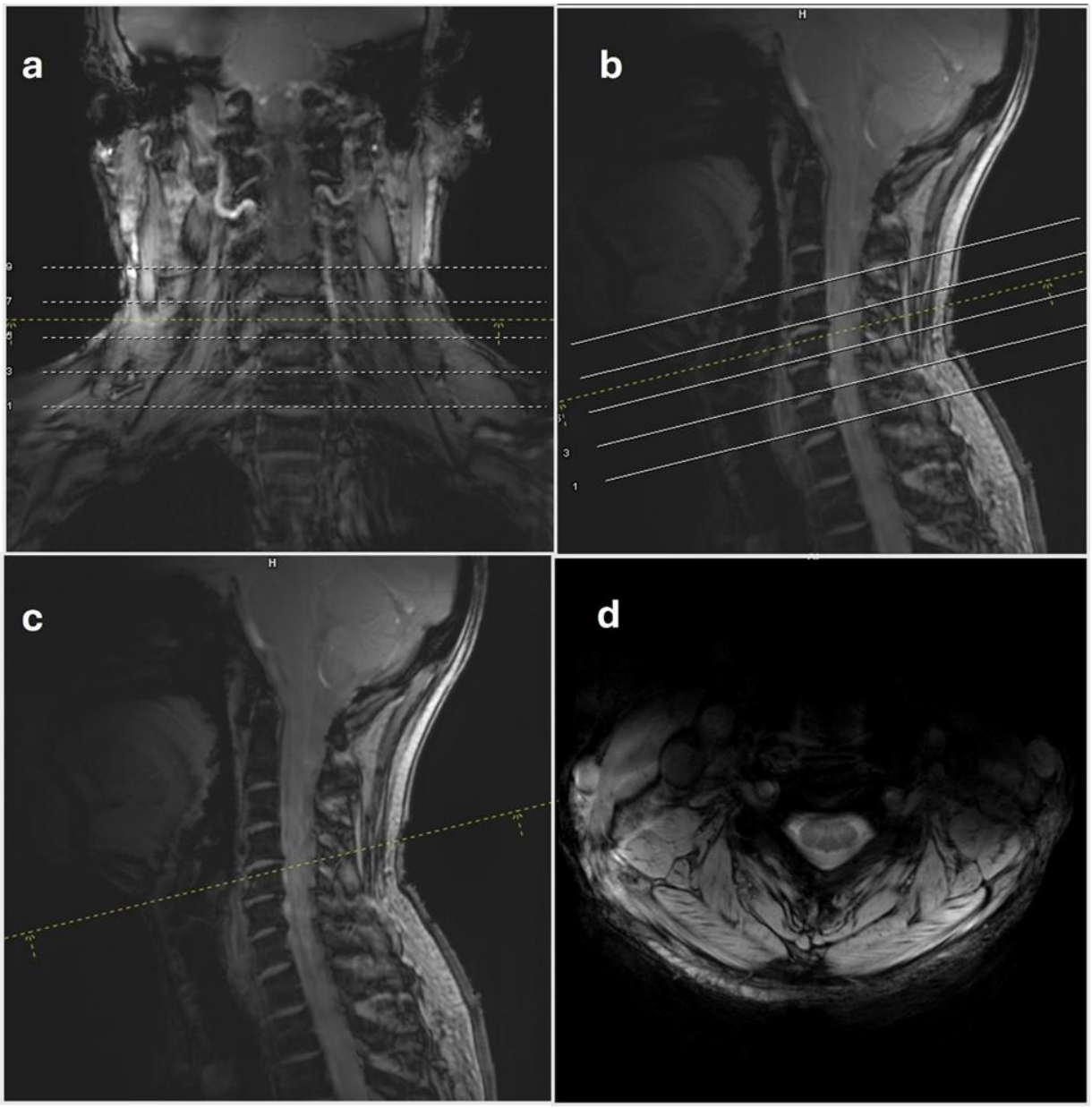

Figure 4.2: Slice positioning on the spinal cord: **(a)** coronal, **(b)** sagittal. A representative slice is selected in **(c) ,** and the corresponding axial MEDIC image is shown in **(d)** .

for the phantom experiment are shown in Figure 2.5. Macroscopic background field inhomogeneity due to (has impact of segmented kspace, no CS)

4.2.3 Radial Image Reconstruction

Image reconstruction from non-Cartesian k-space data, such as radial or spiral trajectories, necessitates specialized algorithms distinct from those employed in standard Cartesian imaging. The most widely used approach for reconstructing such data is the gridding method, which involves interpolating non-Cartesian k-space samples onto a Cartesian grid before applying the Fourier transformation. Gridding typically employs Kaiser-Bessel convolution kernels and density compensation functions (DCFs) to account for varying sampling density in k-space, followed by an inverse FFT to generate the image [178]. To enhance computational efficiency and accuracy, gridding can be implemented using non-uniform fast Fourier transform (NUFFT) algorithms [179], which performs direct transformation from non-Cartesian data to image space without explicit regridding. NUFFT eliminates interpolation artifacts and offers superior performance, particularly for high-resolution or large-scale reconstructions. These methods are widely adopted within the MRI community and are implemented in various toolkits. The Michigan Image Reconstruction Toolbox (MIRT) and the NUFFT package implemented in MATLAB by Fessler provide robust gridding and NUFFT approaches for non-cartesian image reconstruction [179].

An alternative toolbox for non-Cartesian MRI image reconstruction is the Berkeley Advanced Reconstruction Toolbox (BART) [180] that includes various reconstruction algorithms such as gridding, compressed sensing, parallel imaging, and nonlinear inversion methods [181]. BART accommodates multiple types of radial trajectories, including uniform radial and golden-angle radial trajectories. Golden-angle trajectories offer improved temporal incoherence, making them ideal for dynamic and undersampled scenarios, particularly beneficial for compressed sensing [182]. Before image reconstruction, BART's

"estdelay" command corrects for gradient delay errors in radial acquisitions by estimating and compensating for trajectory shifts caused by system imperfections [183, 184]. BART also facilitates the estimation of sensitivity maps from undersampled non-Cartesian data using the "nlinv" function. This function employs a regularized nonlinear inversion algorithm to estimate coil sensitivity maps and the image itself simultaneously [185]. Once the sensitivity maps are generated, they can be utilized in the "pics" tool for parallel imaging and compressed sensing reconstruction. The "pics" tool supports various regularization methods, such as total variation L2 and wavelets, making it well-suited for iterative reconstructions of undersampled radial data [175, 176, 186].

4.3 Results

4.3.1 Radial Stack-of-Star (SoS) Imaging in Human brain

The reconstructed radial images in the human brain are shown in Figure 4.3. The gridding method was used in MATLAB for image reconstruction [187]. TR was 10 [s], TE1=2.40 ms, and ΔTE=3 ms with 11 echo times acquired. Five slices were acquired, which are shown in Figure 4.3 for odd echo times. The acquisition was a single shot with 128 radial spokes, with a resolution of $2 \times 2 \times 5$ mm^3. The total acquisition time was 50 [s].

Brain imaging with Cartesian compared to radial stack-of-stars is shown in Figure 4.4. The radial image has been acquired in a single shot with 512 radial spokes. The image quality is comparable to that of Cartesian imaging, with a significant reduction in scan time achieved through single-shot acquisition. The Cartesian imaging acquires one line of kspace per TR, while the single-shot radial acquisition samples the whole kspace in a single TR.

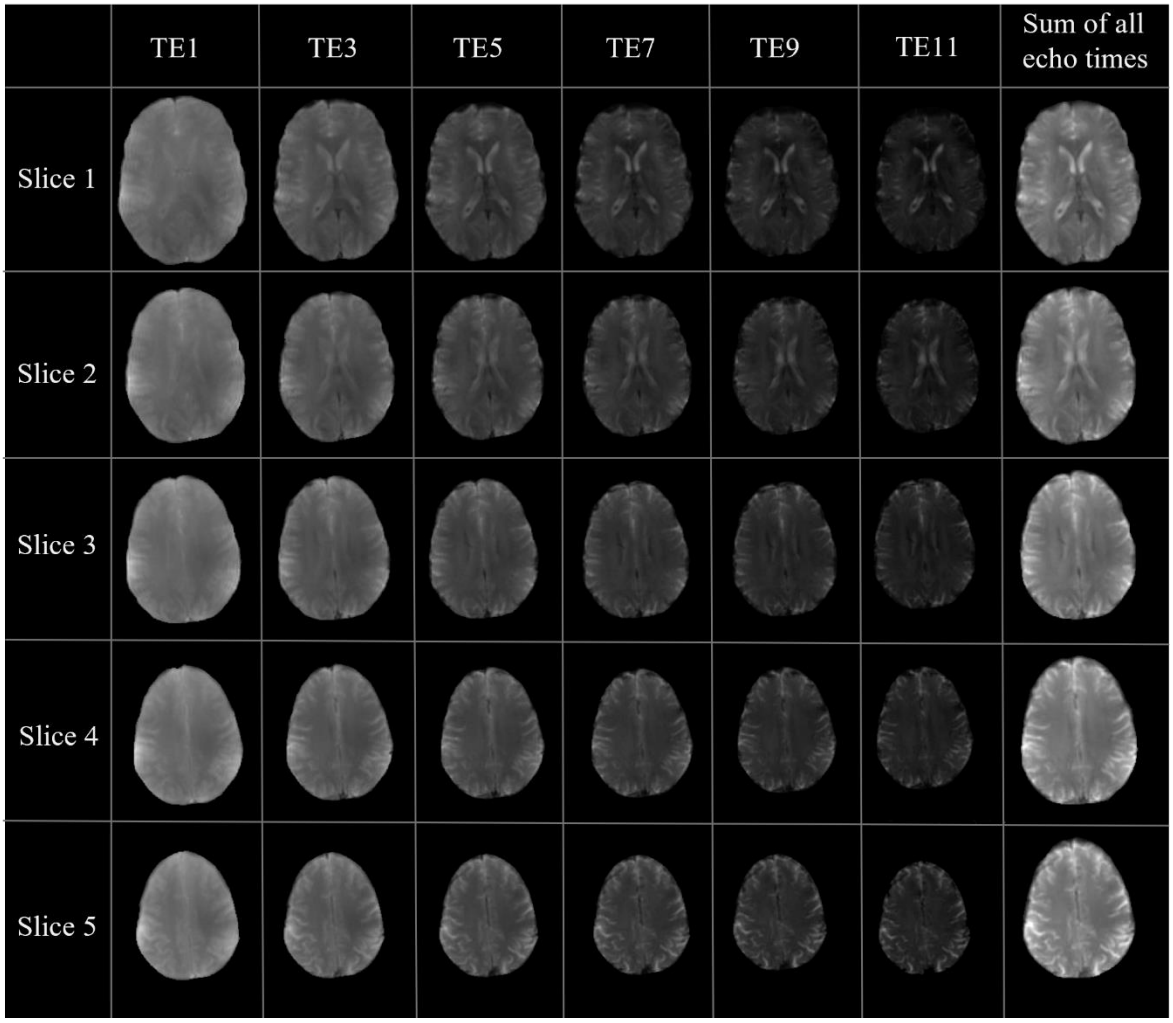

Figure 4.3: Brain imaging with multi-echo radial stack-of-stars acquisition.

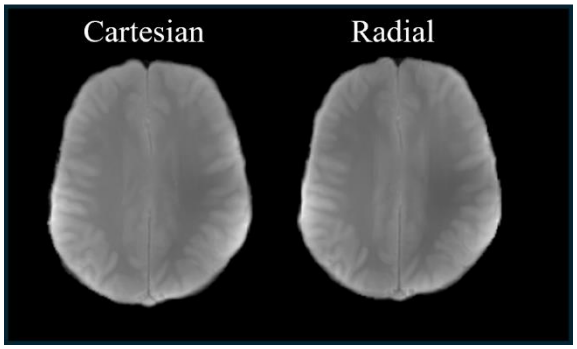

Figure 4.4: Brain imaging with Cartesian compared to radial stack-of-stars. The radial image has been acquired in a single shot with 512 radial spokes.

4.3.1.1 Compressed Sensing Reconstruction for Undersampled Radial Kspace

The results of image reconstruction with an undersampled k-space are shown in Figure 4.5. Data was sampled in a single shot with 32, 64, 128, 256, and 512 radial spokes to compare the image quality. Images were reconstructed in BART with different reconstruction algorithms. The 32-channel sensitivity maps were calculated with the "nlinv" command, which generates coil sensitivities and reconstructs the image at the same time. Wavelet regularization in-plane was done with 100 iterations and a regularization parameter of 0.0015. The L2 norm regularization parameter was 0.001. The quality of the reconstructed images was also compared to that of the standard NUFFT reconstruction method, which does not apply any regularization. Highly undersampled kspace data with 32 spokes generates comparable image quality to denser sampled kspace, indicating a successful acquisition and reconstruction. Radial trajectories are well-suited for compressed sensing-based MRI reconstruction because they inherently provide incoherent sampling of k-space. This incoherence is a crucial requirement for successful compressed sensing [176], enabling the reconstruction of high-quality images from highly undersampled data (Figure 4.5).

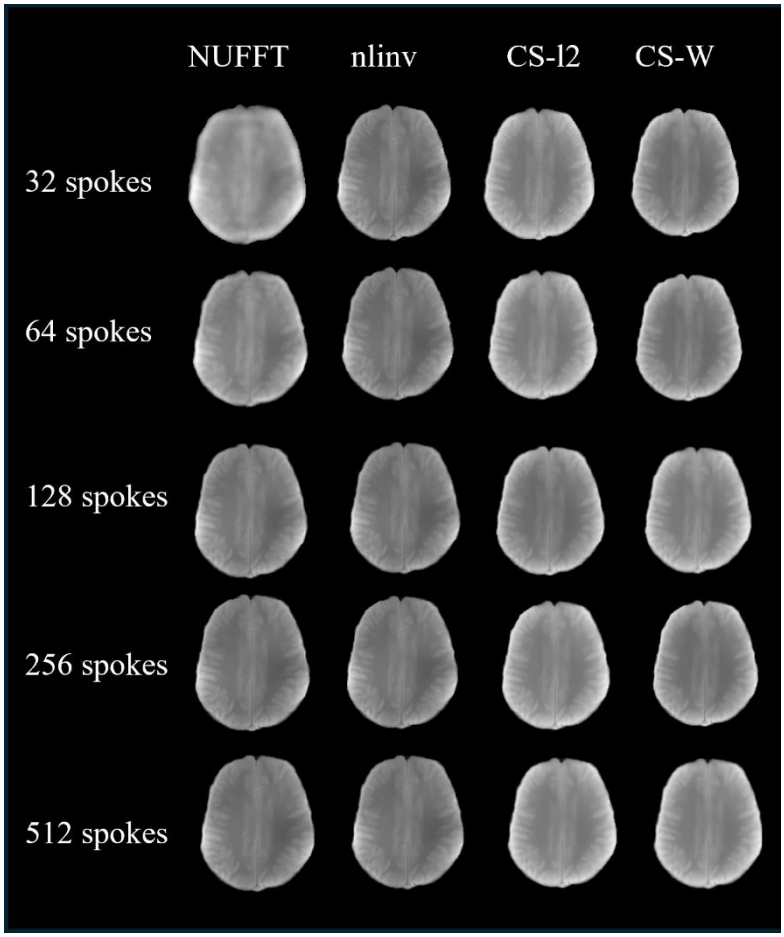

Figure 4.5: Radial image reconstruction from undersampled kspace with 32, 64,128,256, and 512 radial spokes in a single shot. NUFFT, nlinv, and compressed sensing reconstruction with l2-norm (CS-l2) and wavelet regularization (CS-W) were used to generate the images.

4.3.1.2 T2* Mapping in Human Brain Using the Multi-Echo Radial SoS Pulse Sequence

Using a mono-exponential fitting of the multi-echo radial SoS data acquired with a single shot and 128 spokes (shown previously in Figure 4.3), the T2* values were reported in Figure 4.6. With a 10-second TR, 11 echo times, and a total acquisition time of 50 seconds for this single-shot acquisition, T2* maps of the brain were yielded. The Arlo-function toolbox was

used for the magnitude-based fitting. The resolution was $2 \times 2 \times 5$ mm^3, which can be improved to submillimeter resolutions simply by increasing the matrix size (current matrix size is 128 with FOV of 256). Gridding was done in MATLAB for the reconstruction.

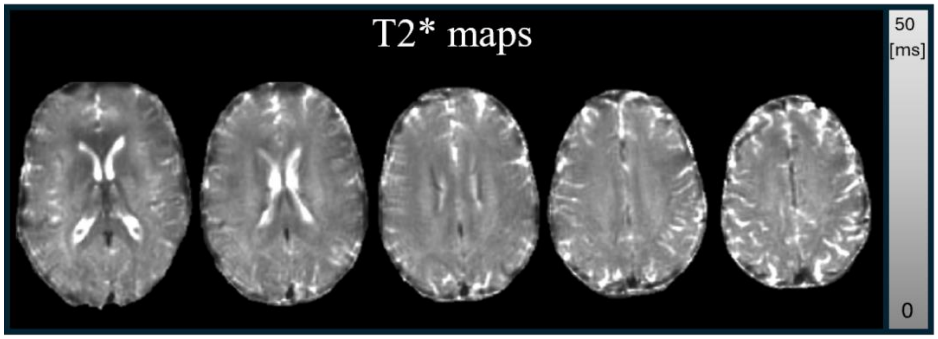

Figure 4.6: T2* maps from different slices in a single healthy subject.

4.3.2 Radial Stack-of-Star (SoS) Imaging in Human Cervical Spinal Cord

Radial images from 1024 spokes in four different slices (Figure 4.7a). The fusion of 5 echoes enhances the Signal-to-noise ratio (SNR) and contrast-to-noise ratio between gray and white matter. The corresponding MEDIC images are from the same location (Figure 4.7b). Qualitatively, radial images provide improved visualization of gray and white matter, yielding sharper results.

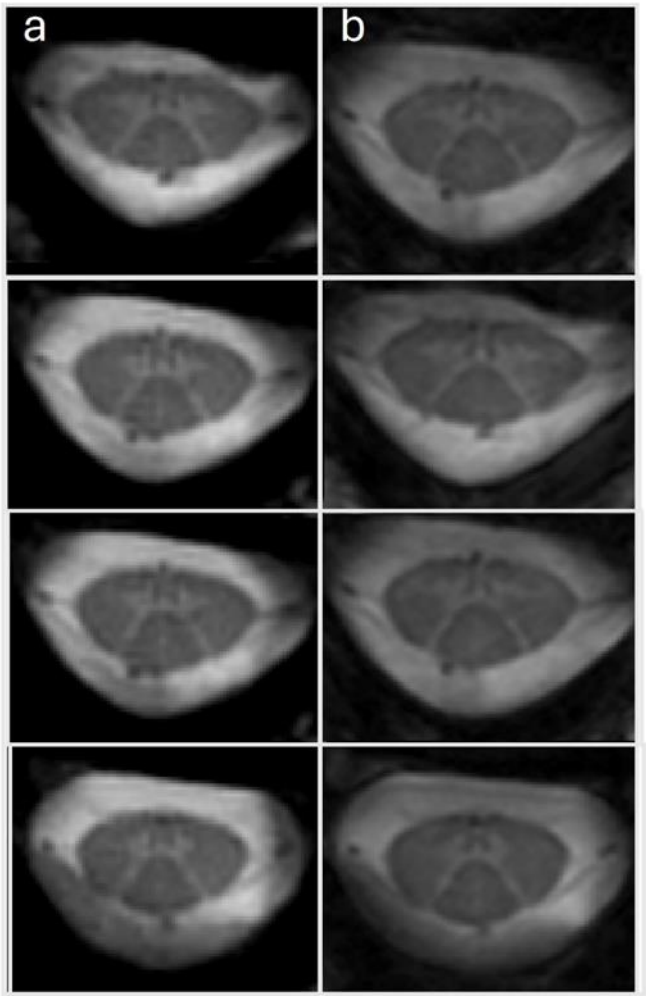

Figure 4.7: a) Reconstructed radial images averaged over all echoes (n = 1024 spokes) and **b)** the corresponding MEDIC images. Qualitatively, radial images provide improved visualization of gray and white matter, producing sharper images.

4.3.2.1 Segmented Readout in Human Spinal Cord

Figure 4.8 shows the effect of segmented kspace acquisition. Although image quality is improved with more segments, single-shot (Figure 4.8a) allows us to reduce imaging time and still generate excellent quality images significantly.

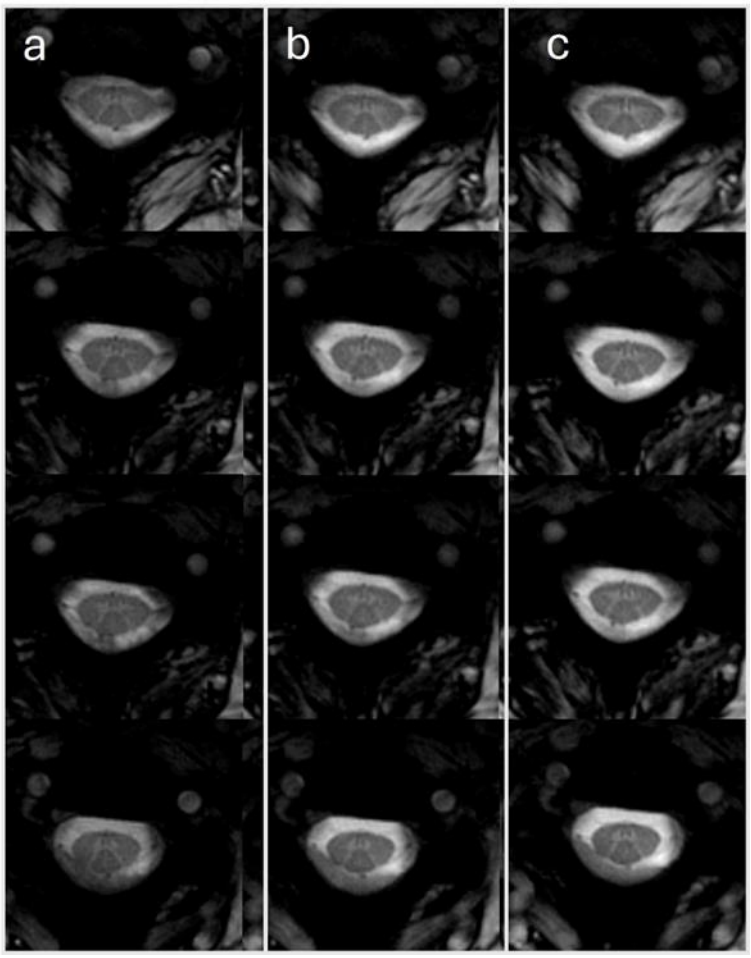

Figure 4.8: Representative radial images from multiple slices (each row) with a segmented k-space with columns **a)** single shot, **b)** 4 segments, and **c)** 8 segments. Although SNR and CNR are improved with multiple segments, excellent quality images can be attained with a single shot, mostly preserving the contrast.

4.3.2.2 T2* Mapping in Human Cervical Spinal Cord using the Multi-Echo Radial SoS Pulse Sequence

The bar plot in Figure 4.9 shows the T2* values obtained using the acquired radial multi-echo images. T2* values are averaged over three slices in GM and WM. Mean T2* values in GM and WM were 0.031 ± 0.003 [s] and 0.028 ± 0.003 [s], respectively. Segmentation was done in the Spinal Cord Toolbox (SCT) [5].

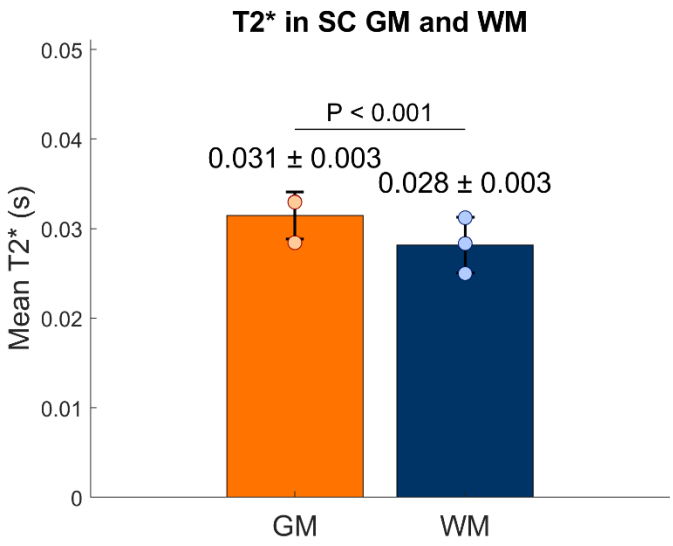

Figure 4.9: Average T2* in the spinal cord GM and WM.

The Golden Angle radial trajectory compensation was computed and applied in gridding.

4.4 Discussion

This study presents the first report on multi-echo high-resolution brain and spinal cord radial stack-of-stars MRI with segmented acquisition and its application to T2* mapping at 7T. Our result shows that high-resolution CNS imaging is feasible using radial imaging with improved contrast during acquisition. Multiple segments slightly improve visual image quality over a single shot at the cost of increased scan time. A radial trajectory is insensitive to bulk motion, which can potentially reduce motion artifacts in uncooperative patients.

Compared to conventional Cartesian multi-echo gradient echo (mGRE) acquisitions, the radial stack-of-stars approach reduced the total scan time per slice. It maintained high fidelity across multiple echo times. This was especially beneficial for T2* mapping in the cervical

spinal cord, where physiological motion and partial volume effects often degrade image quality in Cartesian protocols [188]. Quantitative T2* maps can be used in longitudinal studies to monitor spinal cord pathology. Radial trajectory is perfectly suited for compressed sensing, which can shorten imaging time and will be explored in future studies.

Another key aspect explored was the segmentation strategy of k-space sampling. By varying the number of spokes per segment, we examined the trade-off between scan time (single-shot) and signal-to-noise ratio (multi-shot). The results support a flexible acquisition framework that can be tailored to specific clinical or research needs, favoring speed in motion-prone subjects or maximizing SNR when time permits.

Looking ahead, the radial stack-of-stars approach can be extended to more advanced quantitative frameworks such as MR Fingerprinting (MRF). Incorporating pseudo-random echo timings and variable acquisition parameters into the radial trajectory can enable joint estimation of T1, T2*, and additional tissue properties in a single scan [189]. The inherent motion robustness and flexibility of radial trajectories make them particularly well-suited for these next-generation qMRI applications, especially in challenging areas like the spinal cord.

In conclusion, the radial stack-of-stars method provides a versatile and efficient platform for high-resolution, motion-insensitive imaging and T2* mapping. It not only improves quantitative imaging in the brain and spinal cord at 7T but also lays the groundwork for future integration with multi-parametric and dictionary-based MRI techniques.

Chapter 5: Magnetization Transfer in Human Central Nervous System (CNS) using Radial Stack-of-Stars (SoS) Acquisitions at 7T.

5.1 Introduction

Magnetization transfer (MT) is a magnetic resonance imaging (MRI) contrast mechanism that causes a transfer of energy between bound (macromolecular) and free-water pools comprising the tissue primarily via dipole-dipole interaction [190]. MRI imaging with MT contrast is well-established in clinical practice [191-193]. Perhaps the simplest way to access the bound protons' content is by the magnetization transfer ratio (MTR) assessment, where the ratio of water signal intensities with and without off-resonance irradiation is calculated [194]. MTR is high in myelin-rich white matter (WM), lower in gray matter (GM), and almost zero in CSF, and can be used as a surrogate marker for WM abnormalities in various clinical trials [195]. MTR is a semi-quantitative approach that depends on pulse sequence parameters, scanner hardware dependency, off-resonance frequency, saturation power, etc.

Conventional MTR imaging typically employs Cartesian acquisitions with and without MT saturation pulses, and calculates MTR as the ratio of the saturated to the unsaturated signal intensities. However, such acquisitions are prone to motion artifacts and require long scan times, especially in the spinal cord, where physiological motion and small anatomical structures demand high resolution.

Furthermore, when imaging at higher field strengths, the saturation experiment results in high power deposition, leading to significant tissue heating. This calls for designing and

implementing appropriate RF saturation pulse blocks that can effectively saturate the bound pool while having little to no effect on the free pool. One way to overcome this issue is to repeat low-power RF pulses before the acquisition instead of using high-power RFs.

To address these challenges, we therefore aimed to prepare the magnetization using multiple pulsed-saturation train blocks before our efficient, fast, segmented radial acquisition. Notably, we implemented a rapid, motion-robust Magnetization Transfer imaging protocol using a radial stack-of-stars acquisition at 7 Tesla. The stack-of-stars trajectory offers multiple advantages over Cartesian sampling, including inherent motion insensitivity, oversampling of the k-space center, and compatibility with advanced undersampled reconstruction techniques [175, 177]. These features are particularly beneficial for imaging the brain and spinal cord, where subject motion, pulsatile flow, and susceptibility artifacts pose significant challenges to image quality.

Advanced reconstruction methods are necessary to accelerate scans and enhance patient comfort when working with highly undersampled data. Both parallel imaging and compressed sensing (CS) are methods to accelerate MRI acquisition [176, 196]. Parallel imaging methods like SENSE use the multiple coils' sensitivity profiles to reconstruct MR images from undersampled kspace data [197]. While successful in many cases, SENSE has a limitation in balancing image quality and the scan time reduction [198] that can be improved by using more advanced techniques such as combined CS and SENSE [198] iterative, regularized, and other more general approaches [175, 185, 186, 199].

Therefore, in this work, we generate MTR from the off-resonance spoiled gradient-echo model at 7T with the following enhancements: A customizable train of adiabatic saturation

pulses is implemented that allows saturating with fewer repetitions of low-power RF pulses, b) The readout is segmented, and each segment is prepared with the saturation pulse block, therefore, increasing the MT sensitivity of the resulting signal, c) a highly under-sampled radial acquisition is reconstructed with parallel imaging and compressed sensing reconstruction (pics) that take advantage of multiple coil sensitivity profiles. By default, Pics performs a SENSE reconstruction using a conjugate gradient to generate unaliased images.

This chapter presents MTR maps from the central nervous systems (CNS) of healthy volunteers, highlighting the capability of this radial non-Cartesian technique to generate robust MT contrast in anatomically challenging regions efficiently. The approach has the potential to be extended into clinical populations to assess CNS tissue and lesion properties. Efficient 2D/3D multi-slice MT-prepared data acquisition is also introduced for further optimizing the acquisition scheme.

5.2 Materials and Methods

5.2.1 MT-prepared Radial Acquisition Sequence Design

The schematic of the sequence implemented for MT prepared data acquisition is shown in Figure 5.1. A saturation pulse is applied before the image acquisition to prepare the magnetization with MT contrast.

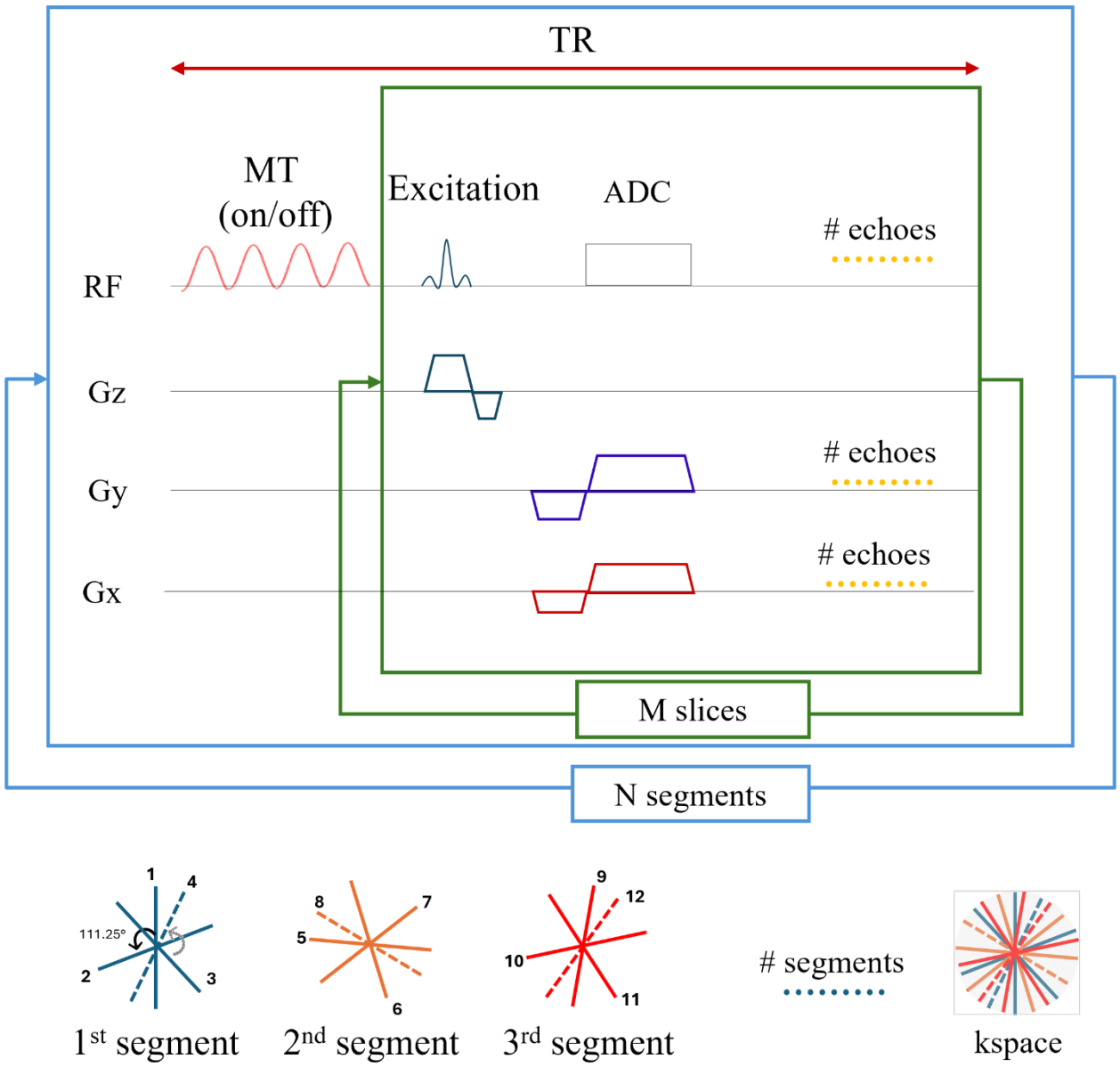

Figure 5.1: Segmented radial SoS data acquisition with MT preparation pulse applied before data acquisition.

Figure 5.1 shows our multi-echo golden angle radial stack-of-stars pulse sequence equipped with a saturation pulse that, when turned on, acquires images with bound pool spins saturated. M_s, and when it is off M_0, it acquires an unsaturated image. The ratio of these two

images gives the targeted MTR image ($MTR = M_s/M_0$).

5.2.2 Phantom Experiment

To find the most efficient MT pulse and acquisition protocol to saturate the magnetization at 7T, we conducted a series of phantom experiments with our segmented radial SoS sequence. We designed a custom phantom with different Agarose concentration tubes (1% to 4%) connected randomly to an oil cylindrical phantom.

The schematic of the RF saturation pulse train is shown in Figure 5.2. Each RF pulse is repeated multiple times, which is set during the acquisition. 1 ms gradient spoilers are present between the train of pulses to destroy any residual transverse magnetization. The pulse amplitude (μT) is also set during the acquisition. Gaussian and Adiabatic pulses were considered with different pulse powers applied in a range of offset frequencies [ppm] to assess the saturation efficiency. See Table 5.1. All the experiments were performed on a Siemens 7T Terra. X.

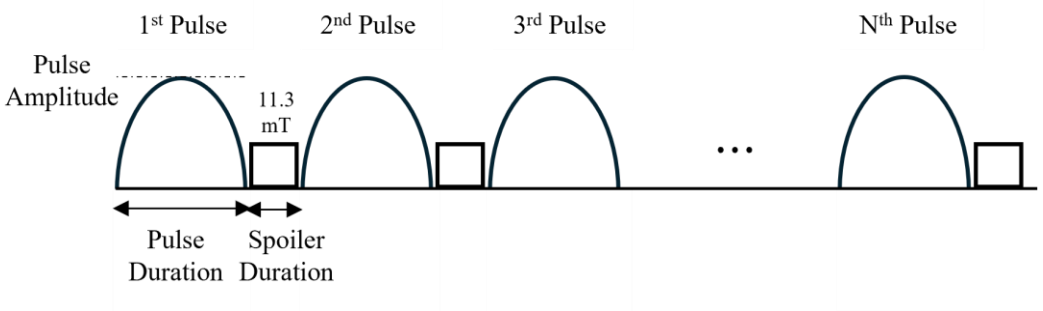

Figure 5.2: RF saturation pulse train applied before our radial SoS acquisition

Table 5.1: Saturation pulse properties for the phantom experiment

Saturation	Pulse Type	MT Pulse	# Pulses in	Offset

Protocol ID	- Duration	amplitude μT	RF Train	[ppm]
Gauss	Gaussian 16 ms	9	1	4
Adiabatic	Adiabatic 49 ms	[5, 9]	[1, 5, 20]	[2, 2.5, 4]

With a fixed number of radial spokes (256), we also compared an 8-segmented readout to 256 segments to analyze the effect of the kspace segmentation on the resulting images.

5.2.2.1 Protocol Optimization Results

The results of the phantom experiment are shown in Figure 5.3. Both Gaussian and Adiabatic RF pulses were applied at 4 ppm with a power of 9 μT, with a duration of 16 ms and 49 ms, respectively. Only a single pulse was used in the saturation pulse train (Figure 5.3, N=1). As shown in this figure, a 50-ms adiabatic pulse applied at 4 ppm yields a strong MT effect that is not observed with the 16-ms Gaussian pulse. The Adiabatic pulse saturation differentiated between different tubes depending on their agar concentration, showing the feasibility of using this setting to sensitize the tissue to the MT effect.

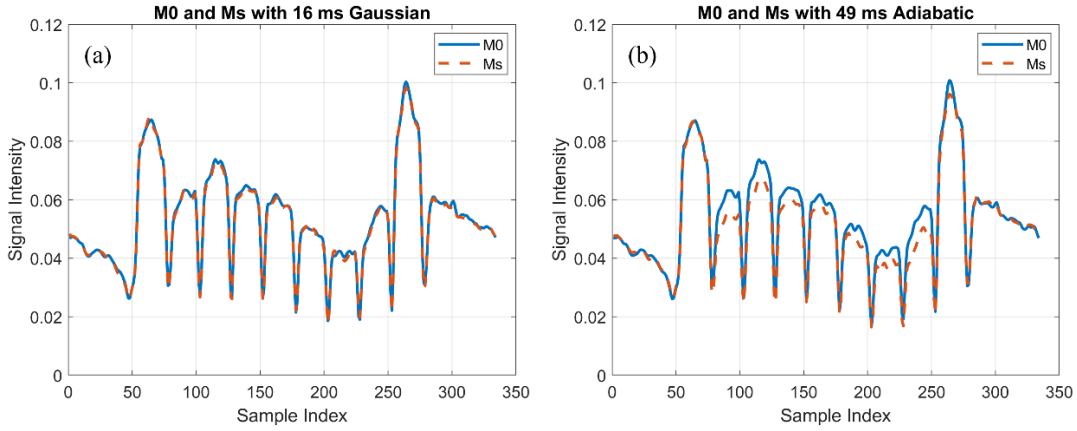

Figure 5.3: a) Gauss 16 ms 9 μT 1 pulse at 4 ppm vs **b)** adiabatic 9 μT 1 pulse at 4 ppm. An adiabatic pulse is more efficient in saturating the bound pool.

Using the adiabatic pulse, we tested different protocols to assess the effect of the number of pulses on the RF pulse train. This can help achieve the optimal saturation protocol, which provides the most saturation at 7T within the tubes undergoing the MT effect, while leaving the water tubes unimpacted. 5 μT adiabatic pulse was applied with the following settings: i) 20 pulses at 2 ppm, ii) 20 pulses at 2.5 ppm, iii) 5 pulses at 2.5 ppm, and iv) 5 pulses at 2 ppm. Data was acquired with 256 spokes on the same phantom with 8 segments as before. The results are shown in Figure 5.4. Saturating at around 2 ppm shows more MT effect compared to Figure 5.3, which was saturated at 4 ppm.

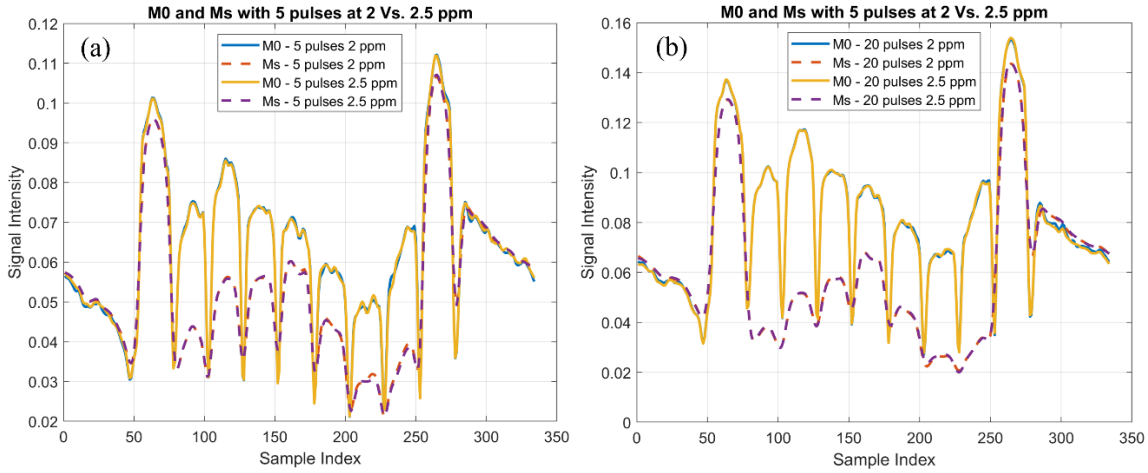

Figure 5.4: MT saturation with **a)** 5 MT pulses and with **b)** 20 MT pulses applied at 2 ppm and 2.5 ppm. Compared to applying fewer pulses, applying 20 consecutive pulses before the readout results in a greater saturation effect within the tubes, allowing for differentiation based on their agar concentration. Pulse power was set to 5 μT and data was acquired in 8 segments with 256 spokes.

5.2.3 In-Vivo Data Acquisition (Brain)

Data was acquired with an 8Tx/32Rx head coil for the brain from a single subject using our

2D radial SoS sequence. One segment acquisition was performed using an MT-prepared pulse train, applied with 20 pulses and 5 μT power at 2 ppm. For this experiment, 1 slice was acquired with TR=2.5 [s] and the total acquisition time was TA=3 [s] due to being a single-shot acquisition. This experiment demonstrates the feasibility of MTR mapping using highly undersampled k-space data with our 2D SoS acquisition. 32, 64, and 256 spokes were acquired for this purpose. The resolution was $1\times1\times5$ mm^3. Other imaging parameters were TE=2 ms, flip angle: 15 degrees, Golden angle (111.25 full spokes). Reconstruction was done in BART using pics with wavelet regularization.

Using the 3D implementation shown in Figure 5.5, we also acquired saturated (Ms) and non-saturated (M0) images with the following scan parameters to generate multiple MTR maps from different slices: 8 slices with slice oversampling of 50% were acquired in a single-shot with a TR= TA= 10 [s]. Resolution was $1\times1\times4$ mm^3, 64 radial spokes, FOV=256. The saturation block contained 120 Adiabatic pulses with 1 uT pulse power, duration of 50 ms, applied at 2 ppm.

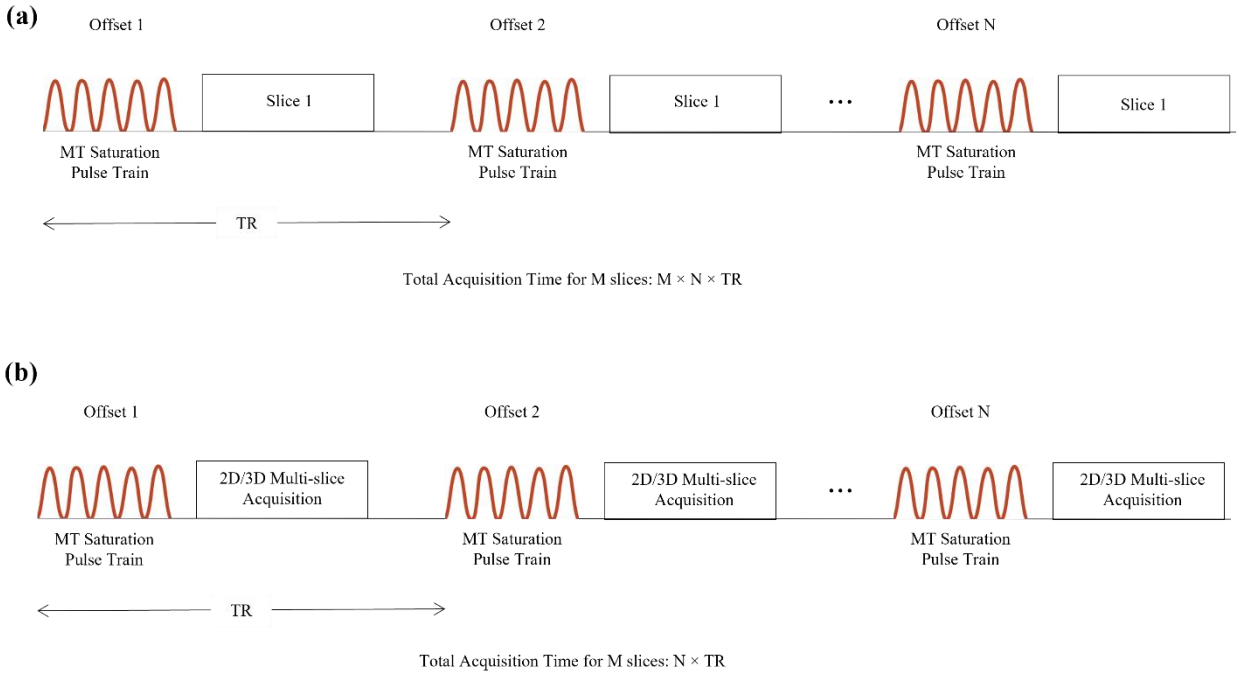

Figure 5.5: The schematic of the 2D/3D multiple slice radial SoS acquisition with MT-prepared magnetization. The arrangement in **a**, leads to a total acquisition time of M×N×TR, while acquiring all slices with a 2D/3D multiple-slice sequence shown in **b**, decreases the scan time by a factor of M (N×TR).

5.2.4 In-Vivo Data Acquisition (Spine)

Data was acquired with an 8-channel spine coil (Rapid Biomedical GmbH) from a single subject using our 2D multi-echo SoS sequence. Twenty adiabatic pulses of power, 5 μT, were applied at 2 ppm before a readout with 384 spokes in a total of 6 segments. Sub-millimeter resolution was 0.5×0.5×5 mm^3. Flip angle was 15 degrees, TR=5 [s], TE=2.5 ms, single slice with golden angle acquisition (111.25 full spokes). Images were reconstructed in BART with L2 regularization.

5.3 Results

5.3.1 MTR in the Brain

The image in Figure 5.6 was acquired using 20 adiabatic pulses applied at 2 ppm, with highly undersampled k-space reconstructed via compressed sensing and parallel imaging in Bart. This demonstrates the feasibility of generating high-quality MTR maps using our sequence, particularly in undersampled settings. Note that there is more MT effect in the WM with 32 spokes compared to 256 spokes in single-shot acquisition. This can be attributed to the loss of magnetization and MT for the final spokes in a 256-spoke acquisition in a single shot, compared to acquiring a limited number of segments (32 spokes). Therefore, undersampling in single-shot acquisitions not only generates the same image quality but also proves more efficient in terms of mitigating the MT saturation loss. Moreover, radial acquisition inherently acquires the center of the k-space first. This helps capture the majority of the contrast at the start of k-space acquisition, before the MT contrast is lost.

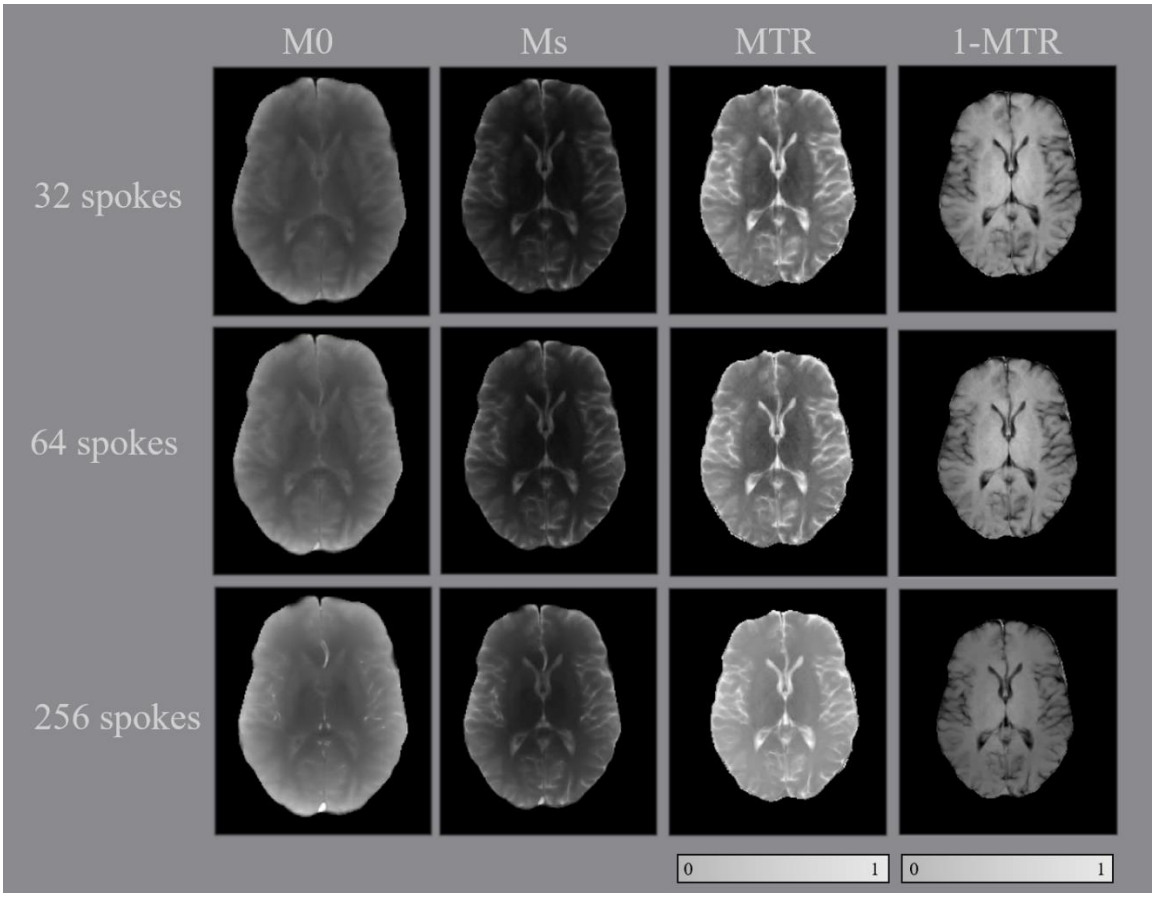

Figure 5.6: In-vivo brain experiment with single-shot kspace with MT-prepared radial SoS acquisition. Twenty pulses with 5 uT power were applied. 32 spokes, 64 spokes, and 256 spokes are shown in each row, respectively. (TR= 2.5 [s], TA= 3 [s]).

5.3.2 2D/3D MTR

An extension of our single-slice MTR mapping to multiple-slice 3D acquisition is shown in Figure 5.7. The arrangement shown in Figure 5.5 enables multiple slice acquisition without increasing scan time.

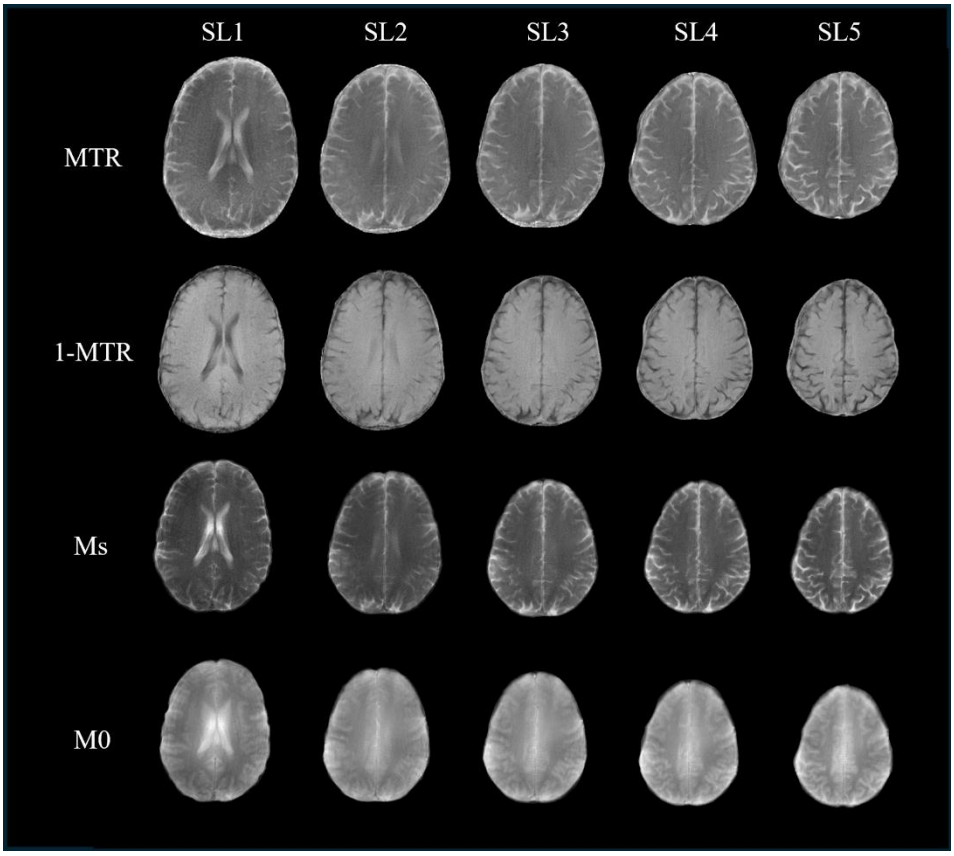

Figure 5.7: Multiple slice brain experiment with single-shot 3D radial SoS acquisition with MT-prepared magnetization. One hundred twenty pulses with 1 uT power were applied. Sixty-four spokes were acquired. (TR= TA= 10 [s].). MTR and 1-MTR maps are shown in a [0 1] range. SL: Slice, Ms: saturated image at 2 ppm, M0: non-saturated image.

5.3.3 MTR in Spinal Cord

The Resulting MTR image of the human spinal cord is shown in Figure 5.8. The free water CSF surrounding the small structure of the spinal cord does not undergo MT effect, as demonstrated by a value of 1 on the MTR map. The WM region in the spinal cord loses magnetization due to the MT effect and appears darker than the GM. The sub-millimeter resolution achieved by high-resolution imaging at 7T using 6-segment radial acquisition makes it feasible to visualize this small structure with good quality and contrast.

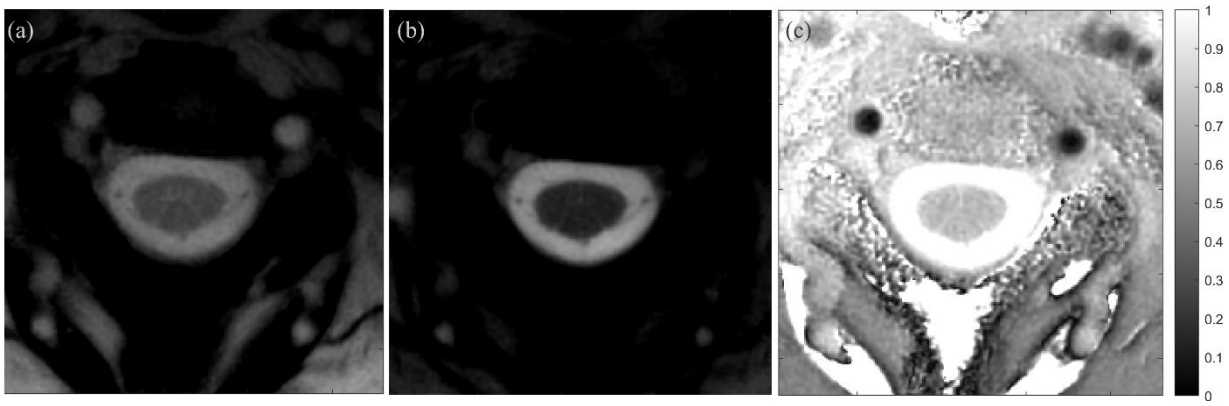

Figure 5.8: In vivo spinal cord MTR with MT-prepared radial SoS acquisition in 6 segments. Twenty pulses with 5 uT power were applied. A) M0 with no saturation, b) Ms with MT saturation at 2 ppm, and c) MTR ratio. TA = 30 [s].

5.4 Discussion

In this chapter, we implemented a radial stack-of-stars (SoS) acquisition with magnetization transfer (MT) preparation at 7T. We demonstrated a promising direction for efficient and motion-robust MTR mapping in anatomically complex regions such as the brain and spinal cord. Our radial stack-of-stars acquisition scheme utilizes the inherent advantages of radial sampling, namely, motion insensitivity, oversampling of the k-space center, and improved tolerance to flow and physiological noise [175, 200] . These properties are particularly advantageous for spinal cord imaging, where subject motion and small cross-sectional area challenge the utility of conventional Cartesian acquisitions.

Previous studies using Cartesian acquisitions for MT imaging in the human brain and spinal cord have demonstrated feasibility and high reproducibility at lower field strengths, such as 3T [201]. Our results extend these findings to ultra-high-field (7T), where the increased signal-

to-noise ratio and enhanced MT contrast further enhance resolution and quantification. Advanced non-Cartesian imaging techniques can improve acquisition speed, enhance MT and image contrast, while reducing sensitivity to motion artifacts. Similar work has previously been done with the Rosette trajectory at 7T [174]. Our radial approach enables flexible undersampling strategies, allowing for acceleration via compressed sensing and parallel imaging without the severe artifacts typically associated with undersampled Cartesian scans. To our knowledge, this is the first study to introduce an MT-prepared multi-echo radial stack-of-stars acquisition, enabling multi-slice 2D and 3D MTR mapping in the human spinal cord at 7T.

While MTR remains a semi-quantitative metric influenced by B1 inhomogeneities and T1 effects, its rapid implementation using stack-of-stars acquisition enables widespread adoption in clinical and research settings. The method could be further enhanced by integrating flip angle corrections and incorporating B1 mapping for improved accuracy [202, 203].

Looking forward, our radial stack-of-stars framework provides a solid foundation for advancing toward more comprehensive quantitative MT modeling, such as qMT parameter estimation using model-based fitting to multiple MT-weighted images. Moreover, this approach is well-suited for integration into MR Fingerprinting (MRF) workflows. Recent developments in MRF have demonstrated that pseudo-randomized acquisition parameters can be combined with dictionary matching to estimate multiple tissue parameters simultaneously [189]. By incorporating MT-sensitive preparations into a radial MRF sequence, it may be possible to simultaneously map parameters such as T1, T2*, and MT metrics in a

single rapid scan.

In summary, radial stack-of-stars acquisition with MT preparation provides a fast, robust, and motion-insensitive method for 2D/3D MTR mapping in the human central nervous system (CNS) at 7T. Equipped with its inherent compatibility with compressed sensing and undersampling reconstruction, it enhances the efficiency of acquisition in undersampled settings while preserving image quality and contrast.

Chapter 6: Spectroscopy

6.1 Introduction

Modern neuroimaging has provided powerful quantitative tools, such as magnetization transfer ratio (MTR), quantitative susceptibility mapping (QSM), and T2* mapping, that elucidate the structural and biochemical substrates of brain disorders. These modalities offer crucial insights into myelin integrity, iron deposition, and microvascular health. However, fully understanding psychiatric conditions like schizophrenia requires probing neurotransmitter systems, notably the gamma-aminobutyric acid (GABA) inhibitory network. This chapter transitions from macrostructural and microstructural measures to the molecular realm, where GABA spectroscopy using 1H-MRS can reveal synaptic-level disruptions and their relation to clinical symptoms and treatment outcomes.

Gamma-aminobutyric acid (GABA), the primary inhibitory neurotransmitter in the central nervous system, has been increasingly implicated in the pathophysiology of schizophrenia (SZ) based on animal models, [204-207] postmortem studies, [208, 209] and a growing number of *in vivo* magnetic resonance spectroscopy (MRS) studies [210, 211]. Postmortem studies in SZ have demonstrated differences in presynaptic GABA synthesis, [209, 212, 213] transport and reuptake, [214, 215] as well as altered postsynaptic GABA receptor expression.[216] Cognitive dysfunction, a core feature of schizophrenia,[217] has been linked to abnormalities in GABA neurons in different brain regions, especially in the prefrontal cortex [218]. The anterior cingulate cortex (ACC), a brain region consistently implicated in the pathophysiology of SZ, [219, 220] plays a critical role in cognitive adjustment and control functions [221] that are known to be impaired in SZ [222]. However, the role of GABA in the ACC and cognition remains poorly understood [211].

Inherent compatibility with compressed sensing and undersampling reconstruction enhances the efficiency of acquisition in undersampled settings while preserving image quality and contrast. Here, we used MRS to measure dorsal ACC GABA levels *in vivo* in a large group of antipsychotic medication-naïve FEP and matched HC. We followed FEP longitudinally, measuring GABA at baseline and after six and sixteen weeks of treatment with antipsychotic medication.[223] Based on the literature, we hypothesized that (1) ACC GABA levels would be lower at baseline in FEP compared to HC, (2) antipsychotic medication treatment would not modulate GABA levels in FEP, and (3) GABA levels in FEP would correlate with cognition scores. Furthermore, to examine the relationship between GABA and treatment response, we measured the percent change in psychiatric symptom scores. Also, we considered patients as treatment responders or non-responders based on Andreasen's remission criteria.[224]

6.2 Methods

6.2.1 Image Acquisition

Participants were scanned on a 3T Siemens MAGNETOM Prisma MRI scanner (Siemens, Erlangen, Germany) equipped with a 20-channel head coil. A high-resolution structural T1-weighted scan (MPRAGE: TR = 2400 ms; TE = 2.22 ms; inversion time = 1000 ms; flip angle = 8°; GRAPPA factor = 2; voxel size = 0.8 mm^3) was acquired for anatomical reference, to guide voxel placement, and for voxel tissue segmentation. A spectroscopy voxel was placed in the dorsal ACC (voxel size: 30 × 40 × 20 mm^3, Figure 6.1a), and outer volume suppression bands were placed close to the edge of the voxel above and below the voxel to reduce unwanted fat signal. After automated and manual shimming to optimize field

homogeneity and water suppression, spectra were acquired using a MEGA-PRESS sequence (TR/TE = 1500/68 ms; flip angle = 90º; 44 Hz bandwidth full width at half maximum editing pulses applied at 1.9 [ON] and 1.5 ppm [OFF]; 256 averages [128 ON and 128 OFF, interleaved]), where editing pulses at 1.9 and 1.5 ppm allow for macromolecule suppression using J-difference editing. We also acquired 16 averages of unsuppressed water scans from the same voxel for reference. Data were saved as single-shot spectra.

6.2.2 MRS Data Processing

Participants Analyses were performed with the Gannet Toolkit in MATLAB. GannetLoad was used to import time-domain data from the scanner and transform data into a frequency-domain GABA-edited spectrum (patient spectrum example in Figure 6.1b). GannetFit was used for nonlinear least-squares fitting of the spectra to integrate the edited GABA peak at 3 ppm and produce GABA concentration estimates. We quantified GABA with respect to water (Figure 6.1c) and corrected measures for CSF and voxel tissue concentrations using tissue correction methods as introduced by Edden et al.[225, 226] The tissue fraction values were based on voxel segmentations with GannetCoRegister and GannetSegment.

6.2.3 Statistical Analysis

Statistical analyses were performed in SPSS (version 29). Demographic variables, spectral quality parameters, and voxel tissue composition measures were compared between groups using independent samples t-tests.

A study flowchart showing the number of participants (HC, healthy controls; FEP, first episode psychosis patients) per timepoint and reasons for exclusion is shown in Figure 6.2.

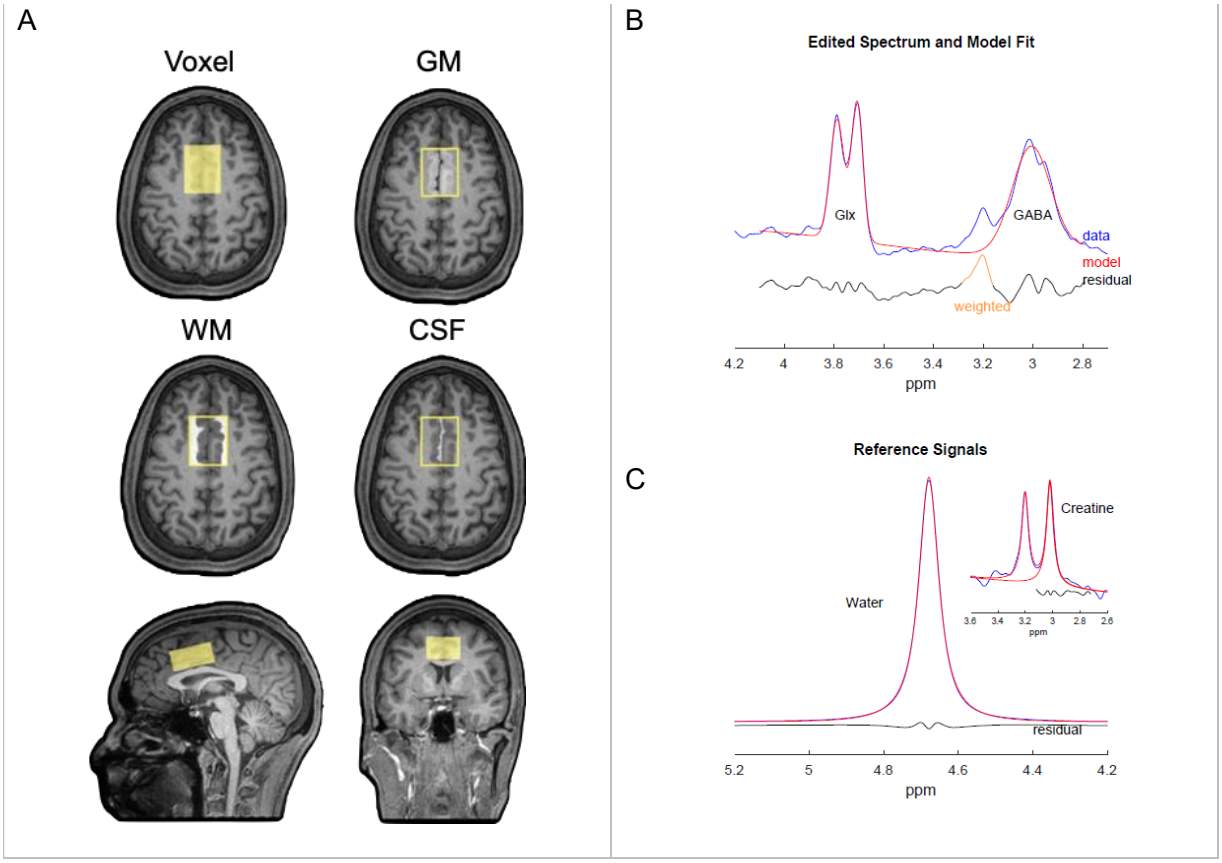

Figure 6.1: a) Example voxel placement for the assessment of GABA in the dorsal anterior cingulate cortex in one subject. Abbreviations: GM, gray matter; WM, white matter; CSF, cerebrospinal fluid. **b)** Example of acquired spectrum in one subject, where the electromagnetic signals of specific molecules are used to quantify the concentration of neurometabolite. Blue line shows the collected spectra; red line is a model fit; and black is the residual. Peaks at approximately 3.8 parts-per-million (ppm) and 3 ppm indicate measures of Glx (combined glutamate + glutamine) and GABA, respectively. **C)** Reference signals show signal amplitudes for water and creatine, where water signals were used for the estimation of GABA levels.

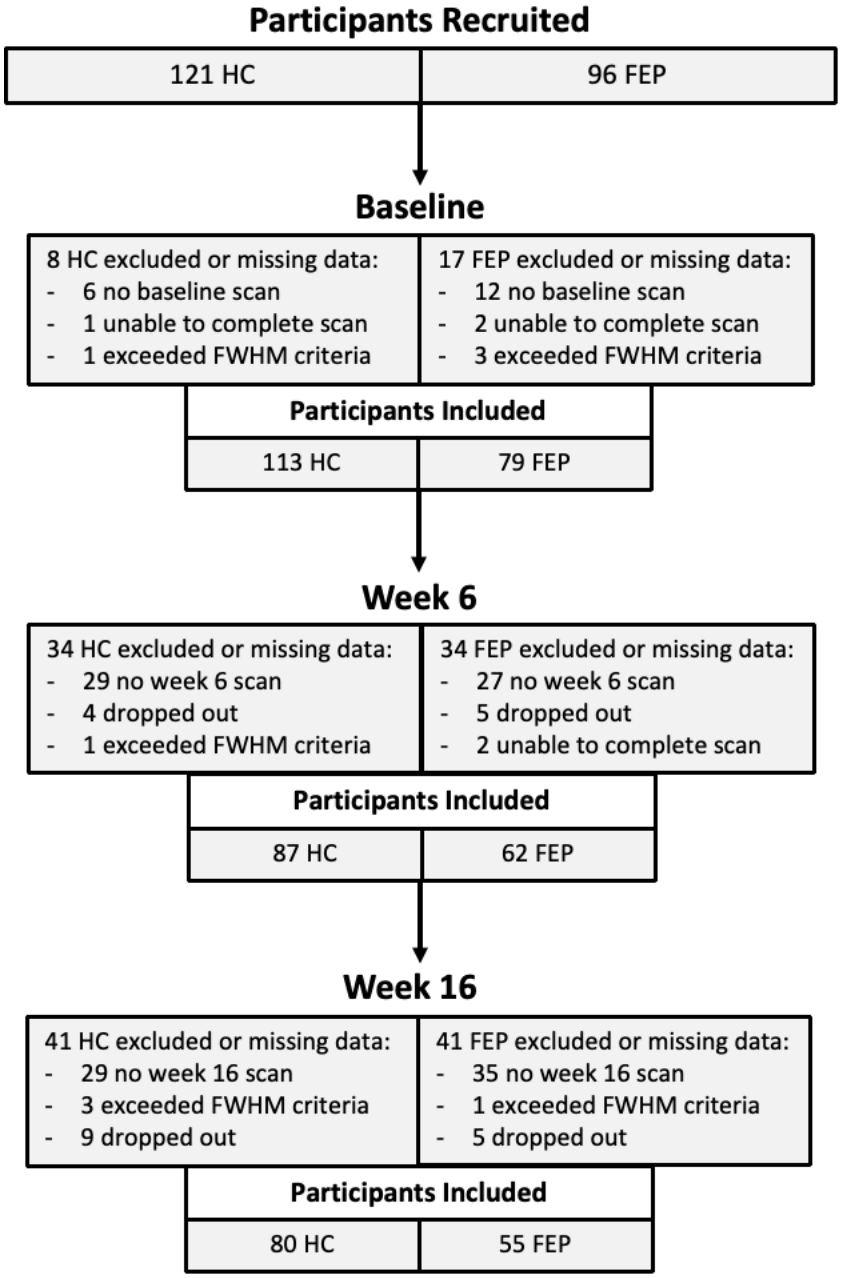

Figure 6.2: participants (HC, healthy controls; FEP, first episode psychosis patients) per timepoint and reasons for exclusion.

6.3 Results

6.3.1 MRS measurement

At baseline, GABA levels were significantly lower in FEP compared to HC ($p = .032$) (Figure

6.3a). Similarly, we also found that GABA levels were significantly lower in FEP compared to HC across all timepoints (p = .014); (Table 6.1, Figure 6.3b). Finally, we found no significant effect of time (p = .739), and no significant group by time interaction (p = .860). When comparing treatment response groups to HC, we found that baseline GABA levels were significantly lower in patients considered non-responders at week 16 (n = 15) than HC (n = 110) (p = .007) (Figure 6.3c), but there was no significant difference between responders (n = 46) and HC (n = 110) (p = .640) (Figure 6.3d).

Table 6.1: GABA to Water Ratio, Spectral Quality, and Tissue Fraction[a]

	Baseline			**Week 6**			**Week 16**		
	HC (n = 113)	FEP (n = 79)	p-value	HC (n = 87)	FEP (n = 62)	p-value	HC (n = 80)	FEP (n = 55)	p-value
Neurometabolite									
GABA/Water	.596 (.12)	.557 (.12)	.036*	.594 (.12)	.554 (.12)	.047*	.581 (.12)	.554 (.14)	.199
Spectral quality									
GABA Fit Error %	4.09 (1.20)	4.53 (1.74)	.037*	4.54 (2.09)	4.77 (2.24)	.522	4.70 (1.91)	4.78 (2.24)	.823
GABA FWHM	18.79 (1.49)	18.96 (1.60)	.445	18.47 (2.50)	18.58 (2.23)	.776	18.44 (2.21)	18.68 (1.70)	.498
GABA SNR	29.86 (6.56)	27.10 (6.29)	.004**	30.02 (7.28)	27.13 (6.66)	.014*	28.94 (6.20)	26.27 (4.79)	.008**
Voxel tissue fraction									
Grey matter (%)	53.26 (4.06)	51.30 (3.90)	.001**	53.51 (4.39)	51.35 (3.49)	.001**	52.74 (5.15)	49.94 (4.26)	.001**
White matter (%)	37.54 (4.74)	38.08 (4.86)	.440	37.02 (5.23)	37.93 (4.37)	.260	37.78 (6.15)	37.96 (7.11)	.876

Mean and standard deviation values for GABA concentration, spectral quality indices, and voxel tissue fraction per group per timepoint. GABA/Water p-values indicate significance as determined by linear mixed model (difference between Groups, HC vs FEP); spectral quality index and voxel tissue fraction indicate significance as determined by independent samples t-tests.
(*) indicates significance at p < .05.
(**) indicates significance at p < .01.
Abbreviations: HC, healthy controls; FEP, first episode psychosis patients; GABA, gamma-aminobutyric acid; FWHM, full width half maximum; SNR, signal-to-noise ratio.
[a] Mean (SD) unless indicated otherwise.

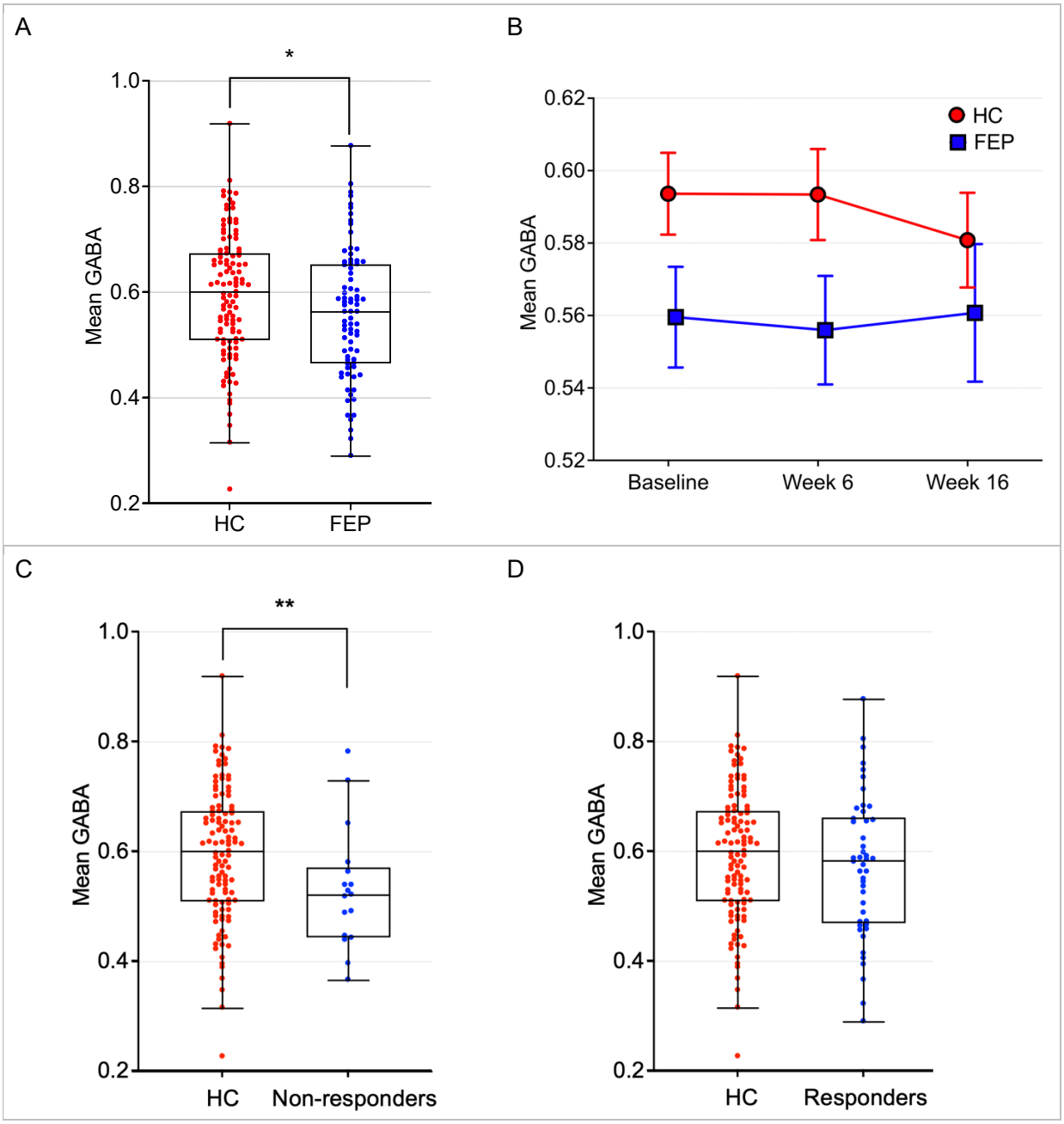

Figure 6.3: (A) Boxplot illustrating baseline GABA concentrations (y-axis) in healthy controls (HC, in red) and first episode psychosis patients (FEP, in blue), where ACC GABA levels are significantly lower in FEP compared to HC. * indicates significance at $p < .05$. (B) Line graph illustrating GABA concentrations (y-axis) in healthy controls (HC, red circles) and first episode psychosis patients (FEP, blue squares) over time (x-axis, at baseline, week 6, and week 16). GABA levels significantly differed between groups, but we found no significant change over time, nor any group-by-time interaction. Error bars indicate +/- 1 standard error from the mean.

(C) Baseline GABA levels significantly differed between HC and patients considered non-responders at 16 weeks of treatment. ** indicates significance at $p < .01$.
(D) Baseline GABA levels did not significantly differ between HC and patients considered responders at 16 weeks of treatment.

6.4 Discussion

To our knowledge, this is the most extensive longitudinal study assessing GABA function in the dorsal ACC *in vivo* in antipsychotic medication-naïve FEP. We report that GABA levels in this region were significantly lower in patients compared to matched HC. GABA levels were lower in patients at baseline and were not affected by treatment with risperidone. Our findings are in agreement with Bojesen [227] who reported lower ACC GABA/Cr (GABA scaled to total creatine) in medication-naïve FEP at baseline, after 6 weeks on aripiprazole monotherapy, and after 26 weeks on "naturalistic antipsychotic treatment" and findings of GABA/Cr levels unaffected by treatment. Together, this study and ours strongly support the proposition that GABA levels are reduced at the start of psychotic illness.

We found that ACC GABA levels can differentiate between treatment responders and non-responders, in agreement with the Bojesen study.[227] Bojesen compared baseline GABA levels in HC, responders, and non-responders at 6 and 26 weeks, and found that GABA levels did not significantly differ between HC and responders, or between HC and non-responders at 6 weeks. However, non-responders in the 26-week group had substantially lower baseline GABA levels than the healthy control group. Similarly, we found that non-responders at 16 weeks had significantly lower baseline GABA levels than the healthy controls (HC), and that responders and HC did not differ significantly.

The major strength of this study is that it is the most extensive longitudinal neuroimaging

study characterizing GABA levels in psychosis spectrum disorders. Further, we used MEGA-PRESS with macromolecule-suppressed editing pulses to acquire GABA, which has been suggested to be a key methodological improvement of the standard MEGA-PRESS sequence, as macromolecule-suppressed GABA measurements correlate more strongly with behavior than macromolecule-contaminated measurements, thus increasing statistical power.[228-230]

In conclusion, our findings strongly support the proposition that GABA dysfunction in the ACC is an essential feature of the core pathophysiology of psychosis, as it is already present in medication-naïve FEP. This dysfunction does not appear to be attenuated by conventional antipsychotic treatment over 16 weeks. Our results also suggest the clinical relevance of baseline GABA levels in identifying patients who are likely to experience a poor clinical response to treatment. It will be important to investigate pharmacological interventions that specifically target GABAergic dysfunction in first-episode psychosis patients.

Chapter 7: Conclusion

Quantitative MRI offers powerful, non-invasive methods for exploring tissue structure, microstructure, and metabolism in vivo. These techniques hold great promise for the early detection and monitoring of central nervous system (CNS) disorders. This dissertation presents a comprehensive pipeline of methodological developments and evaluations, including voxel spread function correction for T2* mapping, reproducibility studies of T2*, QSM, MWF, T1, and qMT mapping techniques, and advanced radial imaging approaches for both T2* and MTR mapping. The integration of non-Cartesian acquisition schemes has enabled motion-robust, high-resolution CNS imaging, particularly well-suited for spinal cord applications.

In an additional chapter, proton magnetic resonance spectroscopy was utilized to measure GABA levels in patients with schizophrenia. This enabled researchers to observe the changes in neurotransmitters and their relationship to treatment. These studies, along with others, form a comprehensive framework that enhances both the technical accuracy and practical utility of quantitative MRI. While further testing is necessary to integrate these techniques into regular clinical practice, the tools and insights derived from this research provide a strong foundation for investigating various neurological and psychiatric conditions through structural, microstructural, and neurochemical biomarkers.

References

1. Hemond CC, Bakshi R. Magnetic resonance imaging in multiple sclerosis. Cold Spring Harbor perspectives in medicine. 2018;8(5):a028969.
2. Chandra A, Dervenoulas G, Politis M, Initiative AsDN. Magnetic resonance imaging in Alzheimer's disease and mild cognitive impairment. Journal of neurology. 2019;266:1293-302.
3. Ji S, Jeong J, Oh S-H, Nam Y, Choi SH, Shin H-G, et al. Quad-contrast imaging: simultaneous acquisition of four contrast-weighted images (pd-weighted, t_2-weighted, pd-flair and t_2-flair images) with synthetic t_1-weighted image, t_1-and t_2-maps. IEEE Transactions on Medical Imaging. 2021;40(12):3617-26.
4. Pierpaoli C. Quantitative brain MRI. LWW; 2010. p. 63.
5. Tofts P. Quantitative MRI of the brain: measuring changes caused by disease: John Wiley & Sons; 2005.
6. Granziera C, Wuerfel J, Barkhof F, Calabrese M, De Stefano N, Enzinger C, et al. Quantitative magnetic resonance imaging towards clinical application in multiple sclerosis. Brain. 2021;144(5):1296-311.
7. Helpern JA, Jensen J, Lee S-P, Falangola MF. Quantitative MRI assessment of Alzheimer's disease. Journal of Molecular Neuroscience. 2004;24:45-8.
8. Keenan KE, Biller JR, Delfino JG, Boss MA, Does MD, Evelhoch JL, et al. Recommendations towards standards for quantitative MRI (qMRI) and outstanding needs. Journal of magnetic resonance imaging: JMRI. 2019;49(7):e26.
9. Leandrou S, Petroudi S, Kyriacou PA, Reyes-Aldasoro CC, Pattichis CS. Quantitative MRI brain studies in mild cognitive impairment and Alzheimer's disease: a methodological review. IEEE reviews in biomedical engineering. 2018;11:97-111.
10. Zhang Y, Gauthier S, Gupta A, Chen W, Comunale J, Chiang G-Y, et al. Quantitative susceptibility mapping and R2* measured changes during white matter lesion development in multiple sclerosis: myelin breakdown, myelin debris degradation and removal, and iron accumulation. American Journal of Neuroradiology. 2016;37(9):1629-35.
11. Mamah D, Wen J, Luo J, Ulrich X, Barch DM, Yablonskiy D. Subcomponents of brain T2* relaxation in schizophrenia, bipolar disorder and siblings: a Gradient Echo Plural Contrast Imaging (GEPCI) study. Schizophrenia research. 2015;169(1-3):36-45.
12. Ghadery C, Pirpamer L, Hofer E, Langkammer C, Petrovic K, Loitfelder M, et al. R2* mapping for brain iron: associations with cognition in normal aging. Neurobiology of Aging. 2015;36(2):925-32.
13. O'Regan DP, Ahmed R, Karunanithy N, Neuwirth C, Tan Y, Durighel G, et al. Reperfusion hemorrhage following acute myocardial infarction: assessment with T2* mapping and effect on measuring the area at risk. Radiology. 2009;250(3):916-22.
14. Vivier P-H, Storey P, Chandarana H, Yamamoto A, Tantillo K, Khan U, et al. Renal blood oxygenation level–dependent imaging: Contribution of r2 to r2* values. Investigative radiology. 2013;48(7):501-8.

15. Aslan E, Luo JW, Lesage A, Paquin P, Cerny M, Chin AS-L, et al. MRI-based R2* mapping in patients with suspected or known iron overload. Abdominal Radiology. 2021;46:2505-15.
16. Yablonskiy DA, Sukstanskii AL, Luo J, Wang X. Voxel spread function method for correction of magnetic field inhomogeneity effects in quantitative gradient-echo-based MRI. Magnetic resonance in medicine. 2013;70(5):1283-92.
17. Wen J, Zeng F, Yablonskiy D, Sukstansky A, Liu Y, Cai B, et al. Fast library-driven approach for implementation of the voxel spread function technique for correcting magnetic field inhomogeneity artifacts. arXiv preprint arXiv:200109400. 2020.
18. Liu Y, Ye Q, Zeng F, Jiang X, Cai B, Lv W, et al. Library-driven approach for fast implementation of the voxel spread function to correct magnetic field inhomogeneity artifacts for gradient-echo sequences. Medical physics. 2021;48(7):3714-20.
19. Wang Y, Spincemaille P, Liu Z, Dimov A, Deh K, Li J, et al. Clinical quantitative susceptibility mapping (QSM): biometal imaging and its emerging roles in patient care. Journal of magnetic resonance imaging. 2017;46(4):951-71.
20. Piredda GF, Hilbert T, Thiran JP, Kober T. Probing myelin content of the human brain with MRI: A review. Magnetic resonance in medicine. 2021;85(2):627-52.
21. Committee QCO, Bilgic B, Costagli M, Chan KS, Duyn J, Langkammer C, et al. Recommended implementation of quantitative susceptibility mapping for clinical research in the brain: a consensus of the ISMRM electro-magnetic tissue properties study group. Magnetic resonance in medicine. 2024;91(5):1834-62.
22. Zhang Y, Gauthier SA, Gupta A, Chen W, Comunale J, Chiang GC-Y, et al. QSM and R2* measured changes during white matter lesion development in multiple sclerosis: myelin breaking down, myelin debris degradation and removal, and iron accumulation. AJNR American journal of neuroradiology. 2016;37(9):1629.
23. Stadelmann C, Timmler S, Barrantes-Freer A, Simons M. Myelin in the central nervous system: structure, function, and pathology. Physiological reviews. 2019;99(3):1381-431.
24. MacKay AL, Laule C. Magnetic resonance of myelin water: an in vivo marker for myelin. Brain plasticity. 2016;2(1):71-91.
25. Cottaar M, Wu W, Tendler BC, Nagy Z, Miller K, Jbabdi S. Quantifying myelin in crossing fibers using diffusion-prepared phase imaging: Theory and simulations. Magnetic Resonance in Medicine. 2021;86(5):2618-34.
26. Mackay A, Whittall K, Adler J, Li D, Paty D, Graeb D. In vivo visualization of myelin water in brain by magnetic resonance. Magnetic resonance in medicine. 1994;31(6):673-7.
27. Nam Y, Lee J, Hwang D, Kim D-H. Improved estimation of myelin water fraction using complex model fitting. NeuroImage. 2015;116:214-21.
28. Alonso-Ortiz E, Levesque IR, Paquin R, Pike GB. Field inhomogeneity correction for gradient echo myelin water fraction imaging. Magnetic resonance in medicine. 2017;78(1):49-57.
29. Alonso-Ortiz E, Levesque IR, Pike GB. MRI-based myelin water imaging: a technical review. Magnetic resonance in medicine. 2015;73(1):70-81.

30. Dvorak AV, Ljungberg E, Vavasour IM, Liu H, Johnson P, Rauscher A, et al. Rapid myelin water imaging for the assessment of cervical spinal cord myelin damage. NeuroImage: Clinical. 2019;23:101896.
31. Kolind S, Abel S, Taylor C, Tam R, Laule C, Li DK, et al. Myelin water imaging in relapsing multiple sclerosis treated with ocrelizumab and interferon beta-1a. NeuroImage: Clinical. 2022;35:103109.
32. Faizy TD, Thaler C, Broocks G, Flottmann F, Leischner H, Kniep H, et al. The myelin water fraction serves as a marker for age-related myelin alterations in the cerebral white matter–a multiparametric MRI aging study. Frontiers in neuroscience. 2020;14:136.
33. Smirnova LP, Yarnykh VL, Parshukova DA, Kornetova EG, Semke AV, Usova AV, et al. Global hypomyelination of the brain white and gray matter in schizophrenia: quantitative imaging using macromolecular proton fraction. Translational psychiatry. 2021;11(1):365.
34. Heath F, Hurley SA, Johansen-Berg H, Sampaio-Baptista C. Advances in noninvasive myelin imaging. Developmental neurobiology. 2018;78(2):136-51.
35. Ou X, Sun SW, Liang HF, Song SK, Gochberg DF. Quantitative magnetization transfer measured pool-size ratio reflects optic nerve myelin content in ex vivo mice. Magnetic Resonance in Medicine: An Official Journal of the International Society for Magnetic Resonance in Medicine. 2009;61(2):364-71.
36. Balchandani P, Naidich T. Ultra-high-field MR neuroimaging. American Journal of Neuroradiology. 2015;36(7):1204-15.
37. Ladd ME, Bachert P, Meyerspeer M, Moser E, Nagel AM, Norris DG, et al. Pros and cons of ultra-high-field MRI/MRS for human application. Progress in nuclear magnetic resonance spectroscopy. 2018;109:1-50.
38. Chavhan GB, Babyn PS, Thomas B, Shroff MM, Haacke EM. Principles, techniques, and applications of T2*-based MR imaging and its special applications. Radiographics. 2009;29(5):1433-49.
39. Hargreaves B. Rapid gradient-echo imaging. Journal of Magnetic Resonance Imaging. 2012;36(6):1300-13.
40. Van der Flier WM, Cordonnier C. Microbleeds in vascular dementia: clinical aspects. Experimental gerontology. 2012;47(11):853-7.
41. Charidimou A, Jäger HR, Werring DJ. Cerebral microbleed detection and mapping: principles, methodological aspects and rationale in vascular dementia. Experimental gerontology. 2012;47(11):843-52.
42. Kidwell CS, Saver JL, Villablanca JP, Duckwiler G, Fredieu A, Gough K, et al. Magnetic resonance imaging detection of microbleeds before thrombolysis: an emerging application. Stroke. 2002;33(1):95-8.
43. Ihn Y-K, Jung W-S, Hwang S-S. The value of T2*-weighted gradient-echo MRI for the diagnosis of cerebral venous sinus thrombosis. Clinical imaging. 2013;37(3):446-50.
44. Tsushima Y, Endo K. Hypointensities in the brain on T2*-weighted gradient-echo magnetic resonance imaging. Current problems in diagnostic radiology. 2006;35(4):140-50.
45. Mamisch TC, Hughes T, Mosher TJ, Mueller C, Trattnig S, Boesch C, et al. T2 star relaxation times for assessment of articular cartilage at 3 T: a feasibility study. Skeletal radiology. 2012;41:287-92.

46. Tang MY, Chen TW, Zhang XM, Huang XH. GRE T2*-weighted MRI: principles and clinical applications. BioMed research international. 2014;2014(1):312142.
47. Meloni A, Hezel F, Positano V, Keilberg P, Pepe A, Lombardi M, et al. Detailing magnetic field strength dependence and segmental artifact distribution of myocardial effective transverse relaxation rate at 1.5, 3.0, and 7.0 T. Magnetic Resonance in Medicine. 2014;71(6):2224-30.
48. Nam Y, Han D, Kim D-H. Single-scan R2⁎ measurement with macroscopic field inhomogeneity correction. Neuroimage. 2012;63(4):1790-9.
49. Simchick G, Liu Z, Nagy T, Xiong M, Zhao Q. Assessment of MR-based and quantitative susceptibility mapping for the quantification of liver iron concentration in a mouse model at 7T. Magnetic resonance in medicine. 2018;80(5):2081-93.
50. Soellradl M, Lesch A, Strasser J, Pirpamer L, Stollberger R, Ropele S, et al. Assessment and correction of macroscopic field variations in 2D spoiled gradient-echo sequences. Magnetic Resonance in Medicine. 2020;84(2):620-33.
51. Steidle G, Schick F. A new concept for improved quantitative analysis of reversible transverse relaxation in tissues with variable microscopic field distribution. Magnetic Resonance in Medicine. 2021;85(3):1493-506.
52. Hernando D, Vigen KK, Shimakawa A, Reeder SB. R mapping in the presence of macroscopic B0 field variations. Magnetic resonance in medicine. 2012;68(3):830-40.
53. Fernandez-Seara M, Wehrli F. Postprocessing technique to correct for background gradients in image-based R* 2 measurements. Magnetic Resonance in Medicine: An Official Journal of the International Society for Magnetic Resonance in Medicine. 2000;44(3):358-66.
54. Yang X, Sammet S, Schmalbrock P, Knopp MV. Postprocessing correction for distortions in T2* decay caused by quadratic cross-slice B0 inhomogeneity. Magnetic resonance in medicine. 2010;63(5):1258-68.
55. Nam Y, Kim H, Zho S-Y, Kim D-H. Background Gradient Correction using Excitation Pulse Profile for Fat and T2* Quantification in 2D Multi-Slice Liver Imaging. Journal of the Korean Society of Magnetic Resonance in Medicine. 2012;16(1):6-15.
56. Shin H-G, Oh S-H, Fukunaga M, Nam Y, Lee D, Jung W, et al. Advances in gradient echo myelin water imaging at 3T and 7T. NeuroImage. 2019;188:835-44.
57. Hezel F, Thalhammer C, Waiczies S, Schulz-Menger J, Niendorf T. High spatial resolution and temporally resolved T2* mapping of normal human myocardium at 7.0 Tesla: an ultrahigh field magnetic resonance feasibility study. PloS one. 2012;7(12):e52324.
58. Hong T, Han D, Kim DH. Simultaneous estimation of PD, T1, T2, T2*, andΔ B0 using magnetic resonance fingerprinting with background gradient compensation. Magnetic resonance in medicine. 2019;81(4):2614-23.
59. Soellradl M, Strasser J, Lesch A, Stollberger R, Ropele S, Langkammer C. Adaptive slice-specific z-shimming for 2D spoiled gradient-echo sequences. Magnetic Resonance in Medicine. 2021;85(2):818-30.
60. Yu H, Shimakawa A, McKenzie CA, Brodsky E, Brittain JH, Reeder SB. Multiecho water-fat separation and simultaneous R estimation with multifrequency fat spectrum modeling. Magnetic Resonance in Medicine: An Official Journal of the International Society for Magnetic Resonance in Medicine. 2008;60(5):1122-34.

61. Reeder SB, Wen Z, Yu H, Pineda AR, Gold GE, Markl M, et al. Multicoil Dixon chemical species separation with an iterative least-squares estimation method. Magnetic Resonance in Medicine: An Official Journal of the International Society for Magnetic Resonance in Medicine. 2004;51(1):35-45.
62. Yu H, Reeder SB, Shimakawa A, Brittain JH, Pelc NJ. Field map estimation with a region growing scheme for iterative 3-point water-fat decomposition. Magnetic Resonance in Medicine: An Official Journal of the International Society for Magnetic Resonance in Medicine. 2005;54(4):1032-9.
63. Han D, Nam Y, Gho SM, Kim DH. Volumetric R2* mapping using z-shim multi-echo gradient echo imaging. Magnetic resonance in medicine. 2015;73(3):1164-70.
64. Luo J, Jagadeesan BD, Cross AH, Yablonskiy DA. Gradient echo plural contrast imaging—signal model and derived contrasts: T2*, T1, phase, SWI, T1f, FST2* and T2*-SWI. Neuroimage. 2012;60(2):1073-82.
65. Vachha B, Huang SY. MRI with ultrahigh field strength and high-performance gradients: challenges and opportunities for clinical neuroimaging at 7 T and beyond. European Radiology Experimental. 2021;5:1-18.
66. Hwang D, Kim D-H, Du YP. In vivo multi-slice mapping of myelin water content using T2* decay. Neuroimage. 2010;52(1):198-204.
67. Yablonskiy DA. Quantitation of intrinsic magnetic susceptibility-related effects in a tissue matrix. Phantom study. Magnetic resonance in medicine. 1998;39(3):417-28.
68. Bashir A, Yablonskiy DA. Natural linewidth chemical shift imaging (NL-CSI). Magnetic Resonance in Medicine: An Official Journal of the International Society for Magnetic Resonance in Medicine. 2006;56(1):7-18.
69. De Leener B, Lévy S, Dupont SM, Fonov VS, Stikov N, Collins DL, et al. SCT: Spinal Cord Toolbox, an open-source software for processing spinal cord MRI data. Neuroimage. 2017;145:24-43.
70. Bioucas-Dias JM, Valadao G. Phase unwrapping via graph cuts. IEEE Transactions on Image processing. 2007;16(3):698-709.
71. De Leener B, Fonov VS, Collins DL, Callot V, Stikov N, Cohen-Adad J. PAM50: Unbiased multimodal template of the brainstem and spinal cord aligned with the ICBM152 space. Neuroimage. 2018;165:170-9.
72. Smith SM, Jenkinson M, Woolrich MW, Beckmann CF, Behrens TE, Johansen-Berg H, et al. Advances in functional and structural MR image analysis and implementation as FSL. Neuroimage. 2004;23:S208-S19.
73. Zhang Y, Brady M, Smith S. Segmentation of brain MR images through a hidden Markov random field model and the expectation-maximization algorithm. IEEE transactions on medical imaging. 2001;20(1):45-57.
74. Bian W, Hess CP, Chang SM, Nelson SJ, Lupo JM. Susceptibility-weighted MR imaging of radiation therapy-induced cerebral microbleeds in patients with glioma: a comparison between 3T and 7T. Neuroradiology. 2014;56(2):91-6.
75. Sati P, Cross AH, Luo J, Hildebolt CF, Yablonskiy DA. In vivo quantitative evaluation of brain tissue damage in multiple sclerosis using gradient echo plural contrast imaging technique. Neuroimage. 2010;51(3):1089-97.

76. Zhao Y, Raichle ME, Wen J, Benzinger TL, Fagan AM, Hassenstab J, et al. In vivo detection of microstructural correlates of brain pathology in preclinical and early Alzheimer Disease with magnetic resonance imaging. Neuroimage. 2017;148:296-304.
77. Vachha B, Huang SY. MRI with ultrahigh field strength and high-performance gradients: challenges and opportunities for clinical neuroimaging at 7 T and beyond. European Radiology Experimental. 2021;5(1):1-18.
78. Jang U, Nam Y, Kim D-H, Hwang D. Improvement of the SNR and resolution of susceptibility-weighted venography by model-based multi-echo denoising. Neuroimage. 2013;70:308-16.
79. Haacke EM, Xu Y, Cheng YCN, Reichenbach JR. Susceptibility weighted imaging (SWI). Magnetic Resonance in Medicine: An Official Journal of the International Society for Magnetic Resonance in Medicine. 2004;52(3):612-8.
80. Musa J, Rahman M, Saliaj K, Siddik AB, Khadra R, Guy A, et al. Popliteal vein aneurysm in a teenager with knee swelling. Radiology Case Reports. 2021;16(6):1410-9.
81. Astafiev SV, Wen J, Brody DL, Cross AH, Anokhin AP, Zinn KL, et al. A novel gradient echo plural contrast imaging method detects brain tissue abnormalities in patients with TBI without evident anatomical changes on clinical MRI: a pilot study. Military medicine. 2019;184(Supplement_1):218-27.
82. Ulrich X, Yablonskiy DA. Separation of cellular and BOLD contributions to T2* signal relaxation. Magnetic resonance in medicine. 2016;75(2):606-15.
83. Haacke EM, Ge Y, Sethi SK, Buch S, Zamboni P. An overview of venous abnormalities related to the development of lesions in multiple sclerosis. Frontiers in Neurology. 2021;12:589.
84. Goldhaber SZ. Diagnosis of pulmonary embolism. Clinical cornerstone. 2000;2(4):38-45.
85. Penailillo E, Bravo-Grau S, Plaza N, Cruz JP. Cerebral Venous Thrombosis: Review of Diagnosis, Follow-Up, Late Complications and Potential Pitfalls. Current Problems in Diagnostic Radiology. 2021;50(5):725-33.
86. Raj S, Bhatia V, Bhatia P, Joshi M, Saini AG, Singh P. Imaging in Cerebral Sinovenous Thrombosis. 2021.
87. ApurvaDubey S, Shukla S, Kumar S. Cerebral Venous Sinus Thrombosis (CVST) in a Young Female with COVID-19 Infection and Oral Contraceptive Pill Ingestion Double Hit?–A Case Report. 2021.
88. Al-Mufti F, Amuluru K, Sahni R, Bekelis K, Karimi R, Ogulnick J, et al. Cerebral venous thrombosis in COVID-19: a New York metropolitan cohort study. American Journal of Neuroradiology. 2021.
89. Filippi M, Rocca MA. MR imaging of multiple sclerosis. Radiology. 2011;259(3):659-81.
90. Seiler A, Nöth U, Hok P, Reiländer A, Maiworm M, Baudrexel S, et al. Multiparametric quantitative MRI in neurological diseases. Frontiers in Neurology. 2021;12:640239.
91. Marcille M, Hurtado Rúa S, Tyshkov C, Jaywant A, Comunale J, Kaunzner UW, et al. Disease correlates of rim lesions on quantitative susceptibility mapping in multiple sclerosis. Scientific Reports. 2022;12(1):4411.

92. Pohmann R, Speck O, Scheffler K. Signal-to-noise ratio and MR tissue parameters in human brain imaging at 3, 7, and 9.4 tesla using current receive coil arrays. Magnetic resonance in medicine. 2016;75(2):801-9.
93. Lutti A, Dick F, Sereno MI, Weiskopf N. Using high-resolution quantitative mapping of R1 as an index of cortical myelination. Neuroimage. 2014;93:176-88.
94. Yarnykh VL. Fast macromolecular proton fraction mapping from a single off-resonance magnetization transfer measurement. Magnetic resonance in medicine. 2012;68(1):166-78.
95. Langkammer C, Schweser F, Krebs N, Deistung A, Goessler W, Scheurer E, et al. Quantitative susceptibility mapping (QSM) as a means to measure brain iron? A post mortem validation study. Neuroimage. 2012;62(3):1593-9.
96. Langkammer C, Liu T, Khalil M, Enzinger C, Jehna M, Fuchs S, et al. Quantitative susceptibility mapping in multiple sclerosis. Radiology. 2013;267(2):551-9.
97. Bagnato F, Franco G, Ye F, Fan R, Commiskey P, Smith SA, et al. Selective inversion recovery quantitative magnetization transfer imaging: Toward a 3 T clinical application in multiple sclerosis. Multiple Sclerosis Journal. 2020;26(4):457-67.
98. Bagnato F, Hametner S, Franco G, Pawate S, Sriram S, Lassmann H, et al. Selective inversion recovery quantitative magnetization transfer brain MRI at 7T: clinical and postmortem validation in multiple sclerosis. Journal of Neuroimaging. 2018;28(4):380-8.
99. Qin Y, Zhu W, Zhan C, Zhao L, Wang J, Tian Q, et al. Investigation on positive correlation of increased brain iron deposition with cognitive impairment in Alzheimer disease by using quantitative MR R2' mapping. Journal of Huazhong University of Science and Technology [Medical Sciences]. 2011;31(4):578-85.
100. Henkelman RM, Huang X, Xiang QS, Stanisz GJ, Swanson SD, Bronskill MJ. Quantitative interpretation of magnetization transfer. Magnetic resonance in medicine. 1993;29(6):759-66.
101. O'Muircheartaigh J, Vavasour I, Ljungberg E, Li DK, Rauscher A, Levesque V, et al. Quantitative neuroimaging measures of myelin in the healthy brain and in multiple sclerosis. Human Brain Mapping. 2019;40(7):2104-16.
102. Giulietti G, Bozzali M, Figura V, Spanò B, Perri R, Marra C, et al. Quantitative magnetization transfer provides information complementary to grey matter atrophy in Alzheimer's disease brains. Neuroimage. 2012;59(2):1114-22.
103. Barritt AW. Understanding the Mechanisms of Neurodegeneration in Amyotrophic Lateral Sclerosis (ALS) Using Detailed Magnetic Resonance Neuroimaging: University of Brighton; 2020.
104. Sled JG, Pike GB. Quantitative interpretation of magnetization transfer in spoiled gradient echo MRI sequences. Journal of Magnetic Resonance. 2000;145(1):24-36.
105. Sled JG, Pike GB. Quantitative imaging of magnetization transfer exchange and relaxation properties in vivo using MRI. Magnetic Resonance in Medicine: An Official Journal of the International Society for Magnetic Resonance in Medicine. 2001;46(5):923-31.
106. Yarnykh VL. Pulsed Z-spectroscopic imaging of cross-relaxation parameters in tissues for human MRI: theory and clinical applications. Magnetic Resonance in Medicine:

An Official Journal of the International Society for Magnetic Resonance in Medicine. 2002;47(5):929-39.
107. Gochberg DF, Kennan RP, Gore JC. Quantitative studies of magnetization transfer by selective excitation and T1 recovery. Magnetic resonance in medicine. 1997;38(2):224-31.
108. Gochberg DF, Fong PM, Gore JC. A quantitative study of magnetization transfer in MAGIC gels. Physics in Medicine & Biology. 2003;48(21):N277.
109. Gochberg DF, Gore JC. Quantitative magnetization transfer imaging via selective inversion recovery with short repetition times. Magnetic Resonance in Medicine: An Official Journal of the International Society for Magnetic Resonance in Medicine. 2007;57(2):437-41.
110. Soellinger M, Langkammer C, Seifert-Held T, Fazekas F, Ropele S. Fast bound pool fraction mapping using stimulated echoes. Magnetic resonance in medicine. 2011;66(3):717-24.
111. Li K, Dortch RD, Kroop SF, Huston JW, Gochberg DF, Park JH, et al. A rapid approach for quantitative magnetization transfer imaging in thigh muscles using the pulsed saturation method. Magnetic resonance imaging. 2015;33(6):709-17.
112. Gochberg DF, Gore JC. Quantitative imaging of magnetization transfer using an inversion recovery sequence. Magnetic Resonance in Medicine: An Official Journal of the International Society for Magnetic Resonance in Medicine. 2003;49(3):501-5.
113. Dortch RD, Li K, Gochberg DF, Welch EB, Dula AN, Tamhane AA, et al. Quantitative magnetization transfer imaging in human brain at 3 T via selective inversion recovery. Magnetic resonance in medicine. 2011;66(5):1346-52.
114. Dortch RD, Moore J, Li K, Jankiewicz M, Gochberg DF, Hirtle JA, et al. Quantitative magnetization transfer imaging of human brain at 7 T. Neuroimage. 2013;64:640-9.
115. Marques JP, Kober T, Krueger G, van der Zwaag W, Van de Moortele P-F, Gruetter R. MP2RAGE, a self bias-field corrected sequence for improved segmentation and T1-mapping at high field. Neuroimage. 2010;49(2):1271-81.
116. Fram EK, Herfkens RJ, Johnson GA, Glover GH, Karis JP, Shimakawa A, et al. Rapid calculation of T1 using variable flip angle gradient refocused imaging. Magnetic resonance imaging. 1987;5(3):201-8.
117. Gupta RK. A new look at the method of variable nutation angle for the measurement of spin-lattice relaxation times using fourier transform NMR. Journal of Magnetic Resonance (1969). 1977;25(1):231-5.
118. Tietze A, Mouridsen K, Mikkelsen IK. The impact of reliable prebolus T 1 measurements or a fixed T 1 value in the assessment of glioma patients with dynamic contrast enhancing MRI. Neuroradiology. 2015;57:561-72.
119. Chang LC, Koay CG, Basser PJ, Pierpaoli C. Linear least-squares method for unbiased estimation of T1 from SPGR signals. Magnetic Resonance in Medicine: An Official Journal of the International Society for Magnetic Resonance in Medicine. 2008;60(2):496-501.
120. Henderson E, McKinnon G, Lee T-Y, Rutt BK. A fast 3D look-locker method for volumetric T1 mapping. Magnetic resonance imaging. 1999;17(8):1163-71.
121. Jahng GH, Stables L, Ebel A, Matson GB, Meyerhoff DJ, Weiner MW, et al. Sensitive and fast mapping based on two inversion recovery images and a reference image. Medical physics. 2005;32(6Part1):1524-8.

122. Drain L. A direct method of measuring nuclear spin-lattice relaxation times. Proceedings of the Physical Society Section A. 1949;62(5):301.
123. Hahn EL. An accurate nuclear magnetic resonance method for measuring spin-lattice relaxation times. Physical Review. 1949;76(1):145.
124. Tsialios P, Thrippleton M, Glatz A, Pernet C, editors. Evaluation of MRI sequences for quantitative T1 brain mapping. Journal of Physics: Conference Series; 2017: IOP Publishing.
125. Henninger B, Kremser C, Rauch S, Eder R, Zoller H, Finkenstedt A, et al. Evaluation of MR imaging with T1 and T2* mapping for the determination of hepatic iron overload. European radiology. 2012;22:2478-86.
126. Dusek P, Dezortova M, Wuerfel J. Imaging of iron. International review of neurobiology. 2013;110:195-239.
127. Möller HE, Bossoni L, Connor JR, Crichton RR, Does MD, Ward RJ, et al. Iron, myelin, and the brain: neuroimaging meets neurobiology. Trends in neurosciences. 2019;42(6):384-401.
128. van der Weijden CW, García DV, Borra RJ, Thurner P, Meilof JF, van Laar P-J, et al. Myelin quantification with MRI: A systematic review of accuracy and reproducibility. Neuroimage. 2021;226:117561.
129. Cohen-Adad J, Polimeni JR, Helmer KG, Benner T, McNab JA, Wald LL, et al. T2* mapping and B0 orientation-dependence at 7 T reveal cyto-and myeloarchitecture organization of the human cortex. Neuroimage. 2012;60(2):1006-14.
130. Pei M, Nguyen TD, Thimmappa ND, Salustri C, Dong F, Cooper MA, et al. Algorithm for fast monoexponential fitting based on auto-regression on linear operations (ARLO) of data. Magnetic resonance in medicine. 2015;73(2):843-50.
131. Leutritz T, Seif M, Helms G, Samson RS, Curt A, Freund P, et al. Multiparameter mapping of relaxation (R1, R2*), proton density and magnetization transfer saturation at 3 T: A multicenter dual-vendor reproducibility and repeatability study. Human brain mapping. 2020;41(15):4232-47.
132. Shmueli K, de Zwart JA, van Gelderen P, Li TQ, Dodd SJ, Duyn JH. Magnetic susceptibility mapping of brain tissue in vivo using MRI phase data. Magnetic Resonance in Medicine: An Official Journal of the International Society for Magnetic Resonance in Medicine. 2009;62(6):1510-22.
133. Liu T, Liu J, De Rochefort L, Spincemaille P, Khalidov I, Ledoux JR, et al. Morphology enabled dipole inversion (MEDI) from a single-angle acquisition: comparison with COSMOS in human brain imaging. Magnetic resonance in medicine. 2011;66(3):777-83.
134. Liu T, Spincemaille P, De Rochefort L, Kressler B, Wang Y. Calculation of susceptibility through multiple orientation sampling (COSMOS): a method for conditioning the inverse problem from measured magnetic field map to susceptibility source image in MRI. Magnetic Resonance in Medicine: An Official Journal of the International Society for Magnetic Resonance in Medicine. 2009;61(1):196-204.
135. De Rochefort L, Liu T, Kressler B, Liu J, Spincemaille P, Lebon V, et al. Quantitative susceptibility map reconstruction from MR phase data using bayesian regularization: validation and application to brain imaging. Magnetic Resonance in Medicine: An Official

Journal of the International Society for Magnetic Resonance in Medicine. 2010;63(1):194-206.
136. Bilgic B, Chatnuntawech I, Fan AP, Setsompop K, Cauley SF, Wald LL, et al. Fast image reconstruction with L2-regularization. Journal of magnetic resonance imaging. 2014;40(1):181-91.
137. Yoon J, Gong E, Chatnuntawech I, Bilgic B, Lee J, Jung W, et al. Quantitative susceptibility mapping using deep neural network: QSMnet. Neuroimage. 2018;179:199-206.
138. Laule C, Vavasour I, Moore G, Oger J, Li DK, Paty D, et al. Water content and myelin water fraction in multiple sclerosis: AT 2 relaxation study. Journal of neurology. 2004;251:284-93.
139. Whittall KP, Mackay AL, Graeb DA, Nugent RA, Li DK, Paty DW. In vivo measurement of T2 distributions and water contents in normal human brain. Magnetic resonance in medicine. 1997;37(1):34-43.
140. . !!! INVALID CITATION !!! 63, 64.
141. Metere R, Kober T, Möller HE, Schäfer A. Simultaneous quantitative MRI mapping of T 1, T 2* and magnetic susceptibility with multi-echo MP2RAGE. PloS one. 2017;12(1):e0169265.
142. Salluzzi M, McCreary CR, Gobbi DG, Lauzon ML, Frayne R. Short-term repeatability and long-term reproducibility of quantitative MR imaging biomarkers in a single centre longitudinal study. NeuroImage. 2022;260:119488.
143. Feng X, Deistung A, Reichenbach JR. Quantitative susceptibility mapping (QSM) and R2* in the human brain at 3 T: Evaluation of intra-scanner repeatability. Zeitschrift für Medizinische Physik. 2018;28(1):36-48.
144. Weiskopf N, Suckling J, Williams G, Correia MM, Inkster B, Tait R, et al. Quantitative multi-parameter mapping of R1, PD*, MT, and R2* at 3T: a multi-center validation. Frontiers in neuroscience. 2013;7:46379.
145. Seif M, Curt A, Thompson AJ, Grabher P, Weiskopf N, Freund P. Quantitative MRI of rostral spinal cord and brain regions is predictive of functional recovery in acute spinal cord injury. NeuroImage: Clinical. 2018;20:556-63.
146. Callaghan MF, Freund P, Draganski B, Anderson E, Cappelletti M, Chowdhury R, et al. Widespread age-related differences in the human brain microstructure revealed by quantitative magnetic resonance imaging. Neurobiology of aging. 2014;35(8):1862-72.
147. McGraw KO, Wong SP. Forming inferences about some intraclass correlation coefficients. Psychological methods. 1996;1(1):30.
148. Li W, Wang N, Yu F, Han H, Cao W, Romero R, et al. A method for estimating and removing streaking artifacts in quantitative susceptibility mapping. Neuroimage. 2015;108:111-22.
149. Jung W, Yoon J, Ji S, Choi JY, Kim JM, Nam Y, et al. Exploring linearity of deep neural network trained QSM: QSMnet+. Neuroimage. 2020;211:116619.
150. Sisco NJ, Wang P, Stokes AM, Dortch RD. Rapid parameter estimation for selective inversion recovery myelin imaging using an open-source Julia toolkit. PeerJ. 2022;10:e13043.

151. Karakuzu A, Boudreau M, Duval T, Boshkovski T, Leppert I, Cabana J-F, et al. qMRLab: Quantitative MRI analysis, under one umbrella. Journal of Open Source Software. 2020;5(53).
152. Deoni SC. High-resolution T1 mapping of the brain at 3T with driven equilibrium single pulse observation of T1 with high-speed incorporation of RF field inhomogeneities (DESPOT1-HIFI). Journal of Magnetic Resonance Imaging: An Official Journal of the International Society for Magnetic Resonance in Medicine. 2007;26(4):1106-11.
153. Cronin MJ, Xu J, Bagnato F, Gochberg DF, Gore JC, Dortch RD. Rapid whole-brain quantitative magnetization transfer imaging using 3D selective inversion recovery sequences. Magnetic resonance imaging. 2020;68:66-74.
154. Dortch RD, Bagnato F, Gochberg DF, Gore JC, Smith SA. Optimization of selective inversion recovery magnetization transfer imaging for macromolecular content mapping in the human brain. Magnetic resonance in medicine. 2018;80(5):1824-35.
155. Desikan RS, Ségonne F, Fischl B, Quinn BT, Dickerson BC, Blacker D, et al. An automated labeling system for subdividing the human cerebral cortex on MRI scans into gyral based regions of interest. Neuroimage. 2006;31(3):968-80.
156. Fischl B, Salat DH, Busa E, Albert M, Dieterich M, Haselgrove C, et al. Whole brain segmentation: automated labeling of neuroanatomical structures in the human brain. Neuron. 2002;33(3):341-55.
157. York EN, Thrippleton MJ, Meijboom R, Hunt DP, Waldman AD. Quantitative magnetization transfer imaging in relapsing-remitting multiple sclerosis: A systematic review and meta-analysis. Brain Communications. 2022;4(2):fcac088.
158. Yushkevich PA, Piven J, Hazlett HC, Smith RG, Ho S, Gee JC, et al. User-guided 3D active contour segmentation of anatomical structures: significantly improved efficiency and reliability. Neuroimage. 2006;31(3):1116-28.
159. Lee Y, Callaghan MF, Acosta-Cabronero J, Lutti A, Nagy Z. Establishing intra-and inter-vendor reproducibility of T1 relaxation time measurements with 3T MRI. Magnetic resonance in medicine. 2019;81(1):454-65.
160. Dieringer MA, Deimling M, Santoro D, Wuerfel J, Madai VI, Sobesky J, et al. Rapid parametric mapping of the longitudinal relaxation time T1 using two-dimensional variable flip angle magnetic resonance imaging at 1.5 Tesla, 3 Tesla, and 7 Tesla. PLoS One. 2014;9(3):e91318.
161. Avants BB, Epstein CL, Grossman M, Gee JC. Symmetric diffeomorphic image registration with cross-correlation: evaluating automated labeling of elderly and neurodegenerative brain. Medical image analysis. 2008;12(1):26-41.
162. Özbay PS, Deistung A, Feng X, Nanz D, Reichenbach JR, Schweser F. A comprehensive numerical analysis of background phase correction with V-SHARP. NMR in Biomedicine. 2017;30(4):e3550.
163. Canales-Rodríguez EJ, Pizzolato M, Piredda GF, Hilbert T, Kunz N, Pot C, et al. Comparison of non-parametric T2 relaxometry methods for myelin water quantification. Medical Image Analysis. 2021;69:101959.
164. Choi S, Li X, Harrison DM. The impact of coregistration of gradient recalled echo images on quantitative susceptibility and R2* mapping at 7T. bioRxiv. 2019:529891.

165. Rua C, Clarke WT, Driver ID, Mougin O, Morgan AT, Clare S, et al. Multi-centre, multi-vendor reproducibility of 7T QSM and R2* in the human brain: results from the UK7T study. Neuroimage. 2020;223:117358.
166. Betts MJ, Acosta-Cabronero J, Cardenas-Blanco A, Nestor PJ, Düzel E. High-resolution characterisation of the aging brain using simultaneous quantitative susceptibility mapping (QSM) and R2* measurements at 7 T. Neuroimage. 2016;138:43-63.
167. Nguyen TD, Deh K, Monohan E, Pandya S, Spincemaille P, Raj A, et al. Feasibility and reproducibility of whole brain myelin water mapping in 4 minutes using fast acquisition with spiral trajectory and adiabatic T2prep (FAST-T2) at 3T. Magnetic resonance in medicine. 2016;76(2):456-65.
168. Makovac E, Serra L, Di Domenico C, Marra C, Caltagirone C, Cercignani M, et al. Quantitative magnetization transfer of white matter tracts correlates with diffusion tensor imaging indices in predicting the conversion from mild cognitive impairment to Alzheimer's disease. Journal of Alzheimer's Disease. 2018;63(2):561-75.
169. Bluestein KT, Pitt D, Knopp MV, Schmalbrock P. T1 and proton density at 7 T in patients with multiple sclerosis: an initial study. Magnetic resonance imaging. 2012;30(1):19-25.
170. MacKay A, Laule C, Vavasour I, Bjarnason T, Kolind S, Mädler B. Insights into brain microstructure from the T2 distribution. Magnetic resonance imaging. 2006;24(4):515-25.
171. Deistung A, Schweser F, Reichenbach JR. Overview of quantitative susceptibility mapping. NMR in Biomedicine. 2017;30(4):e3569.
172. Feng L. Golden-angle radial MRI: basics, advances, and applications. Journal of Magnetic Resonance Imaging. 2022;56(1):45-62.
173. Ahn C, Kim J, Cho Z. High-speed spiral-scan echo planar NMR imaging-I. IEEE transactions on medical imaging. 1986;5(1):2-7.
174. Mahmud SZ, Denney TS, Bashir A. Feasibility of spinal cord imaging at 7 T using rosette trajectory with magnetization transfer preparation and compressed sensing. Scientific Reports. 2023;13(1):8777.
175. Block KT, Uecker M, Frahm J. Undersampled radial MRI with multiple coils. Iterative image reconstruction using a total variation constraint. Magnetic Resonance in Medicine: An Official Journal of the International Society for Magnetic Resonance in Medicine. 2007;57(6):1086-98.
176. Lustig M, Donoho D, Pauly JM. Sparse MRI: The application of compressed sensing for rapid MR imaging. Magnetic Resonance in Medicine: An Official Journal of the International Society for Magnetic Resonance in Medicine. 2007;58(6):1182-95.
177. Coppo S, Piccini D, Bonanno G, Chaptinel J, Vincenti G, Feliciano H, et al. Free-running 4D whole-heart self-navigated golden angle MRI: initial results. Magnetic resonance in medicine. 2015;74(5):1306-16.
178. Jackson JI, Meyer CH, Nishimura DG, Macovski A. Selection of a convolution function for Fourier inversion using gridding (computerised tomography application). IEEE transactions on medical imaging. 1991;10(3):473-8.
179. Fessler JA, Sutton BP. Nonuniform fast Fourier transforms using min-max interpolation. IEEE transactions on signal processing. 2003;51(2):560-74.

180. Uecker M, Ong F, Tamir JI, Bahri D, Virtue P, Cheng JY, et al., editors. Berkeley advanced reconstruction toolbox. Proc Intl Soc Mag Reson Med; 2015.
181. Uecker M, Lai P, Murphy MJ, Virtue P, Elad M, Pauly JM, et al. ESPIRiT—an eigenvalue approach to autocalibrating parallel MRI: where SENSE meets GRAPPA. Magnetic resonance in medicine. 2014;71(3):990-1001.
182. Winkelmann S, Schaeffter T, Koehler T, Eggers H, Doessel O. An optimal radial profile order based on the Golden Ratio for time-resolved MRI. IEEE transactions on medical imaging. 2006;26(1):68-76.
183. Block KT, Uecker M, editors. Simple method for adaptive gradient-delay compensation in radial MRI. Proceedings of the 19th Annual Meeting of ISMRM, Montreal, Canada; 2011.
184. Rosenzweig S, Holme HCM, Uecker M. Simple auto-calibrated gradient delay estimation from few spokes using radial intersections (RING). Magnetic resonance in medicine. 2019;81(3):1898-906.
185. Uecker M, Hohage T, Block KT, Frahm J. Image reconstruction by regularized nonlinear inversion—joint estimation of coil sensitivities and image content. Magnetic Resonance in Medicine. 2008;60(3):674-82.
186. Liu B, King K, Steckner M, Xie J, Sheng J, Ying L. Regularized sensitivity encoding (SENSE) reconstruction using Bregman iterations. Magnetic Resonance in Medicine: An Official Journal of the International Society for Magnetic Resonance in Medicine. 2009;61(1):145-52.
187. Pauly J. Non-cartesian reconstruction. URL: http://www stanford edu/class/ee369c/notes/non cart rec. 2005;7.
188. Stroman PW, Wheeler-Kingshott C, Bacon M, Schwab J, Bosma R, Brooks J, et al. The current state-of-the-art of spinal cord imaging: methods. Neuroimage. 2014;84:1070-81.
189. Ma D, Gulani V, Seiberlich N, Liu K, Sunshine JL, Duerk JL, et al. Magnetic resonance fingerprinting. Nature. 2013;495(7440):187-92.
190. De Boer R. Magnetization transfer contrast. Part. 1995;1:64-73.
191. Grossman RI, Gomori JM, Ramer KN, Lexa FJ, Schnall MD. Magnetization transfer: theory and clinical applications in neuroradiology. Radiographics. 1994;14(2):279-90.
192. Sui YV, Bertisch H, Goff DC, Samsonov A, Lazar M. Quantitative magnetization transfer and g-ratio imaging of white matter myelin in early psychotic spectrum disorders. Molecular Psychiatry. 2025:1-9.
193. Mancini M, Cercignani M. Magnetization transfer imaging in multiple sclerosis. Handbook of Imaging in Multiple Sclerosis: Elsevier; 2025. p. 191-205.
194. Gloor M, Andelova M, Gaetano L, Papadopoulou A, Burguet Villena F, Sprenger T, et al. Longitudinal analysis of new multiple sclerosis lesions with magnetization transfer and diffusion tensor imaging. European Radiology. 2024;34(3):1680-91.
195. Davies G, Altmann D, Hadjiprocopis A, Rashid W, Chard D, Griffin C, et al. Increasing normal–appearing grey and white matter magnetisation transfer ratio abnormality in early relapsing–remitting multiple sclerosis. Journal of neurology. 2005;252:1037-44.

196. Sartoretti T, Reischauer C, Sartoretti E, Binkert C, Najafi A, Sartoretti-Schefer S. Common artefacts encountered on images acquired with combined compressed sensing and SENSE. Insights into imaging. 2018;9:1107-15.
197. Pruessmann KP, Weiger M, Scheidegger MB, Boesiger P. SENSE: sensitivity encoding for fast MRI. Magnetic Resonance in Medicine: An Official Journal of the International Society for Magnetic Resonance in Medicine. 1999;42(5):952-62.
198. Cho S, Choi Y, Chung S, Lee J, Baek J. High-resolution MRI using compressed sensing-sensitivity encoding (CS-SENSE) for patients with suspected neurovascular compression syndrome: comparison with the conventional SENSE parallel acquisition technique. Clinical Radiology. 2019;74(10):817. e9-. e14.
199. Lustig M, Pauly JM. SPIRiT: iterative self-consistent parallel imaging reconstruction from arbitrary k-space. Magnetic resonance in medicine. 2010;64(2):457-71.
200. Smith AK, Dortch RD, Dethrage LM, Smith SA. Rapid, high-resolution quantitative magnetization transfer MRI of the human spinal cord. Neuroimage. 2014;95:106-16.
201. Battiston M, Grussu F, Ianus A, Schneider T, Prados F, Fairney J, et al. An optimized framework for quantitative magnetization transfer imaging of the cervical spinal cord in vivo. Magnetic resonance in medicine. 2018;79(5):2576-88.
202. Yarnykh VL. Actual flip-angle imaging in the pulsed steady state: a method for rapid three-dimensional mapping of the transmitted radiofrequency field. Magnetic Resonance in Medicine: An Official Journal of the International Society for Magnetic Resonance in Medicine. 2007;57(1):192-200.
203. Samson RS, Wheeler-Kingshott CA, Symms MR, Tozer DJ, Tofts PS. A simple correction for B1 field errors in magnetization transfer ratio measurements. Magnetic resonance imaging. 2006;24(3):255-63.
204. Wozniak M, Cieslik P, Marciniak M, Lenda T, Pilc A, Wieronska JM. Neurochemical changes underlying schizophrenia-related behavior in a modified forced swim test in mice. Pharmacol Biochem Behav. 2018;172:50-8.
205. Amitai N, Kuczenski R, Behrens MM, Markou A. Repeated phencyclidine administration alters glutamate release and decreases GABA markers in the prefrontal cortex of rats. Neuropharmacology. 2012;62(3):1422-31.
206. Fujikawa R, Yamada J, Jinno S. Subclass imbalance of parvalbumin-expressing GABAergic neurons in the hippocampus of a mouse ketamine model for schizophrenia, with reference to perineuronal nets. Schizophr Res. 2021;229:80-93.
207. Esclapez M, Tillakaratne NJ, Kaufman DL, Tobin AJ, Houser CR. Comparative localization of two forms of glutamic acid decarboxylase and their mRNAs in rat brain supports the concept of functional differences between the forms. J Neurosci. 1994;14(3 Pt 2):1834-55.
208. Hashimoto T, Volk DW, Eggan SM, Mirnics K, Pierri JN, Sun Z, et al. Gene expression deficits in a subclass of GABA neurons in the prefrontal cortex of subjects with schizophrenia. J Neurosci. 2003;23(15):6315-26.
209. Volk DW, Austin MC, Pierri JN, Sampson AR, Lewis DA. Decreased glutamic acid decarboxylase67 messenger RNA expression in a subset of prefrontal cortical gamma-

aminobutyric acid neurons in subjects with schizophrenia. Arch Gen Psychiatry. 2000;57(3):237-45.
210. Bojesen KB, Broberg BV, Fagerlund B, Jessen K, Thomas MB, Sigvard A, et al. Associations Between Cognitive Function and Levels of Glutamatergic Metabolites and Gamma-Aminobutyric Acid in Antipsychotic-Naive Patients With Schizophrenia or Psychosis. Biol Psychiatry. 2021;89(3):278-87.
211. Reddy-Thootkur M, Kraguljac NV, Lahti AC. The role of glutamate and GABA in cognitive dysfunction in schizophrenia and mood disorders - A systematic review of magnetic resonance spectroscopy studies. Schizophr Res. 2022;249:74-84.
212. Thompson M, Weickert CS, Wyatt E, Webster MJ. Decreased glutamic acid decarboxylase(67) mRNA expression in multiple brain areas of patients with schizophrenia and mood disorders. J Psychiatr Res. 2009;43(11):970-7.
213. Tavazzani E, Tritto S, Spaiardi P, Botta L, Manca M, Prigioni I, et al. Glutamic acid decarboxylase 67 expression by a distinct population of mouse vestibular supporting cells. Front Cell Neurosci. 2014;8:428.
214. de Jonge JC, Vinkers CH, Hulshoff Pol HE, Marsman A. GABAergic Mechanisms in Schizophrenia: Linking Postmortem and In Vivo Studies. Front Psychiatry. 2017;8:118.
215. Guidotti A, Auta J, Davis JM, Di-Giorgi-Gerevini V, Dwivedi Y, Grayson DR, et al. Decrease in reelin and glutamic acid decarboxylase67 (GAD67) expression in schizophrenia and bipolar disorder: a postmortem brain study. Arch Gen Psychiatry. 2000;57(11):1061-9.
216. Volk DW, Pierri JN, Fritschy JM, Auh S, Sampson AR, Lewis DA. Reciprocal alterations in pre- and postsynaptic inhibitory markers at chandelier cell inputs to pyramidal neurons in schizophrenia. Cereb Cortex. 2002;12(10):1063-70.
217. Dickinson D, Iannone VN, Wilk CM, Gold JM. General and specific cognitive deficits in schizophrenia. Biol Psychiatry. 2004;55(8):826-33.
218. Bast T, Pezze M, McGarrity S. Cognitive deficits caused by prefrontal cortical and hippocampal neural disinhibition. Br J Pharmacol. 2017;174(19):3211-25.
219. Lahti AC, Weiler MA, Holcomb HH, Tamminga CA, Carpenter WT, McMahon R. Correlations between rCBF and symptoms in two independent cohorts of drug-free patients with schizophrenia. Neuropsychopharmacology. 2006;31(1):221-30.
220. Wang Y, Yang Y, Xu W, Yao X, Xie X, Zhang L, et al. Heterogeneous Brain Abnormalities in Schizophrenia Converge on a Common Network Associated With Symptom Remission. Schizophr Bull. 2024;50(3):545-56.
221. Van Veen V, Carter CS. The timing of action-monitoring processes in the anterior cingulate cortex. J Cogn Neurosci. 2002;14(4):593-602.
222. Minzenberg MJ, Laird AR, Thelen S, Carter CS, Glahn DC. Meta-analysis of 41 functional neuroimaging studies of executive function in schizophrenia. Arch Gen Psychiatry. 2009;66(8):811-22.
223. Emsley R, Rabinowitz J, Medori R. Time course for antipsychotic treatment response in first-episode schizophrenia. Am J Psychiatry. 2006;163(4):743-5.
224. Andreasen NC, Carpenter WT, Jr., Kane JM, Lasser RA, Marder SR, Weinberger DR. Remission in schizophrenia: proposed criteria and rationale for consensus. Am J Psychiatry. 2005;162(3):441-9.

225. Edden RA, Puts NA, Harris AD, Barker PB, Evans CJ. Gannet: A batch-processing tool for the quantitative analysis of gamma-aminobutyric acid-edited MR spectroscopy spectra. J Magn Reson Imaging. 2014;40(6):1445-52.
226. Harris AD, Puts NA, Edden RA. Tissue correction for GABA-edited MRS: Considerations of voxel composition, tissue segmentation, and tissue relaxations. J Magn Reson Imaging. 2015;42(5):1431-40.
227. Bojesen KB, Ebdrup BH, Jessen K, Sigvard A, Tangmose K, Edden RAE, et al. Treatment response after 6 and 26 weeks is related to baseline glutamate and GABA levels in antipsychotic-naive patients with psychosis. Psychol Med. 2020;50(13):2182-93.
228. Edden RA, Puts NA, Barker PB. Macromolecule-suppressed GABA-edited magnetic resonance spectroscopy at 3T. Magn Reson Med. 2012;68(3):657-61.
229. Mikkelsen M, Barker PB, Bhattacharyya PK, Brix MK, Buur PF, Cecil KM, et al. Big GABA: Edited MR spectroscopy at 24 research sites. Neuroimage. 2017;159:32-45.
230. Mikkelsen M, Harris AD, Edden RAE, Puts NAJ. Macromolecule-suppressed GABA measurements correlate more strongly with behavior than macromolecule-contaminated GABA+measurements. Brain Res. 2018;1701:204-11.

Appendix

Here, we include the subject-by-subject voxel-wise and ROI-based.

Analysis. **Table A1** shows the voxel-wise results of ICC with confidence intervals (CI), p-values, Cohen's effect size d value, absolute value of bias (abs(bias)), and variability (Var.) in WM. The mean is the average over all subjects with the corresponding standard deviation (SD). Lower and upper bounds of limits of agreements in the Bland-Altman plots are shown in the LOA (lb, ub) format. **Table A2** presents the same R2*, QSM, and T1 maps analysis, excluding bias and variance results, which will be presented in **Table A3. Table A3** shows the subject-level abs (bias) and Var. results for R2*, QSM, and T1 maps in the selected ROIs.

The coefficient of variation (CV) % for each subject (pairwise CV) in the ROI-based analysis is shown in **Table A4** for the qMR maps. Each subject's average qMR value in each ROI is considered one data point, and the CV is calculated between the pair of scans and rescan values. An average over all subjects is also reported in this table.

Table A.1. F-map and MWF map in WM. CI is the confidence interval, and d is Cohen's effect size.

qMR map	ROI	WM		
	Metric	ICC [CI], r (p,d)	abs (Bias) LOA (lb,ub)	LOA Var. (ub-lb)
F	sub1	86 [76,91], 91 (<0.001,0.26)	0.013 (-0.06,0.03)	0.09
	sub2	92 [91.7,92], 93 (0.21,0.02)	0.001 (-0.03,0.04)	0.07
	sub3	89 [87,90], 90 (<0.001,0.1)	0.005 (-0.04,0.05)	0.09
	sub4	97 [96.7,97], 97 (<0.001,0.05)	0.002 (-0.02,0.02)	0.04
	sub5	94 [93,94], 95 (<0.001,0.06)	0.003 (-0.04,0.03)	0.07
	sub6	93 [90,94], 94 (<0.001,0.12)	0.006 (-0.03,0.04)	0.07
	sub7	95 [94.4,95], 95 (0.47,0.01)	0 (-0.03,0.03)	0.06
	sub8	94 [93.6,94], 94 (<0.001,0.02)	0.001 (-0.04,0.03)	0.07
	Mean ± SD	(92.5 ± 3.51, 93.63 ± 2.26)	0.004 ± 0.004	0.07 ± 0.02
MWF	sub1	82 [75,87], 85 (<0.001,0.23)	0.024 (-0.14,0.09)	0.23
	sub2	86 [84,87], 86 (0.42,0.04)	0.004 (-0.11,0.1)	0.21
	sub3	73 [67,78], 75 (<0.001,0.23)	0.022 (-0.15,0.11)	0.26
	sub4	81 [78,84], 82 (0.003,0.13)	0.011 (-0.11,0.09)	0.27
	sub5	77 [69,83], 81 (<0.001,0.25)	0.028 (-0.16,0.11)	0.27
	sub6	80 [75,84], 81 (<0.001,0.18)	0.02 (-0.15,0.11)	0.26
	sub7	85 [77,89], 88 (<0.001,0.22)	0.021 (-0.12,0.07)	0.19
	sub8	84 [83,86], 85 (0.17,0.06)	0.006 (-0.11,0.1)	0.21
	Mean ± SD	(81 ± 4.34, 82.88 ± 4.05)	0.017 ± 0.009	0.24 ± 0.03

Table A.2. R2*, QSM, and T1 map voxel-wise analysis in 4 ROIs: Caudate (Ca.), Putamen (Pu.), left hemisphere WM (lh-WM), and left hemisphere GM (lh-GM).

qMR map	ROI	Ca	Pu	lh-WM	lh-GM
	Metric	ICC [CI], r (p , d)	ICC [CI], r (p , d)	ICC [CI], r (p , d)	ICC [CI], r (p , d)
R2*	sub1	91[64,97], 96 (<0.001,0.36)	91 [89,92], 91 (0.5,0.05)	80 [74,83], 81 (<0.001,0.21)	75 [73,76], 75 (<0.001,0.12)
	sub2	95 [94,96], 96 (0.49,0.03)	90 [81,94], 93 (0.04,0.21)	85 [83,88], 86 (<0.001,0.14)	84 [83.5,85], 84 (<0.001,0.05)
	sub3	93 [92,95], 94 (0.02,0.09)	83 [74,89], 86 (<0.001,0.24)	85 [80,89], 87 (<0.001,0.21)	84 [83,84], 84 (<0.001,0.05)
	sub4	90 [75,95], 93 (<0.001,0.25)	55 [7,77], 82 (<0.001,0.73)	76 [75,78], 77 (<0.001,0.11)	81 [80,82], 81 (0.95,0.001)
	sub5	95 [94.5,96], 96 (0.5,0.04)	89 [80,93], 92 (<0.001,0.21)	69 [60,76], 74 (<0.001,0.35)	77 [76,78], 77 (0.02,0.04)
	sub6	75 [73,78], 81 (0.73,0.01)	56 [46,64], 65 (0.88,0.02)	68 [62,73], 72 (<0.001,0.25)	77 [76,77], 77 (<0.001,0.06)
	sub7	95 [92,97], 96 (0.004,0.13)	78 [58,87], 84 (0.003,0.34)	89 [88,90], 89 (<0.001,0.08)	88 [87.9,88.8], 88 (0.4,0.01)
	sub8	99 [98,99], 99 (0.78,0.01)	97 [96,97], 97 (0.29,0.06)	80 [79.5,81], 81 (0.27,0.01)	85 [85,86], 85 (0.3,0.01)
	Mean±SD (ICC, r)	(91.63 ± 7.27, 93.88 ± 5.49)	(79.88 ± 16.06, 86.25 ± 9.93)	(79 ± 7.6, 80.88 ± 6.22)	(81.38 ± 4.63, 81.38 ± 4.63)
QSM	sub1	91 [49,97], 96 (<0.001,0.32)	80 [50,90], 87 (<0.001,0.39)	94 [93,94], 94 (<0.001,0.04)	89 [89,90], 90 (<0.001,0.07)
	sub2	87 [85,89], 90 (0.02,0.09)	96 [95,97], 97 (0.91,0.01)	80 [76,83], 83 (<0.001,0.18)	78 [77,79], 79 (<0.001,0.07)
	sub3	88 [66,94], 92 (<0.001,0.3)	96 [52,99], 98 (0.43,0.23)	92 [91,92], 92 (<0.001,0.08)	88 [88,89], 89 (<0.001,0.06)
	sub4	90 [84,94], 93 (<0.001,0.19)	95 [94,95], 95 (0.42,0.04)	88 [87.6,88.5], 89 (<0.001,0.05)	85 [84.7,85.7], 87 (0.08,0.02)
	sub5	90 [89,92], 92 (0.06,0.09)	93 [91,95], 93 (0.68,0.04)	89 [88,90], 90 (<0.001,0.08)	76 [74,77], 76 (<0.001,0.07)
	sub6	70 [50,80], 77 (<0.001,0.39)	89 [74,94], 91 (0.01,0.25)	75 [71,77], 76 (<0.001,0.17)	68 [67,70], 69 (<0.001,0.11)
	sub7	91 [85,95], 93 (<0.001,0.18)	78 [5,92], 96 (<0.001,0.56)	92 [85,95], 94 (<0.001,0.19)	92 [90,94], 93 (<0.001,0.12)
	sub8	94 [93,95], 95 (0.08,0.09)	92 [74,96], 95 (0.01,0.24)	94 [93,95], 95 (<0.001,0.08)	90 [88,91], 91 (<0.001,0.09)
	Mean±SD (ICC, r)	(87.63 ± 7.42, 91 ± 5.95	(89.88 ± 7.12, 94 ± 3.59)	(88 ± 6.95, 89.13 ± 6.56)	(83.25 ± 8.4, 84.25 ± 8.56)

Table A.2-continued.

qMR map	ROI	Ca	Pu	lh-WM	lh-GM
	Metric	ICC [CI], r (p,d)	ICC [CI], r (p,d)	ICC [CI], r (p,d)	ICC [CI], r (p,d)
T1	sub1	95 [92,96], 95 (0.07,0.11)	82 [72,88], 85 (0.01,0.25)	91 [89,93], 93 (<0.001,0.14)	81 [80,82], 81 (0.01,0.05)
	sub2	90 [34,97], 97 (<0.001,0.34)	75 [66,81], 77 (<0.001,0.26)	80 [75,83], 84 (<0.001,0.19)	69 [60,75], 73 (<0.001,0.28)
	sub3	64 [35,78], 76 (<0.001,0.49)	53 [46,59], 54 (0.002,0.2)	89 [85,91], 90 (<0.01,0.16)	77 [75,78], 77 (<0.001,0.08)
	sub4	95 [90,97], 96 (0.02,0.14)	79 [74,83], 82 (0.015,0.16)	93 [92,94], 94 (<0.001,0.1)	86 [85,86], 86 (0.41,0.02)
	sub5	62 [4,82], 86 (<0.001,0.72)	88 [85,90], 88 (0.11,0.10)	86 [85,87], 86 (<0.001,0.08)	74 [67,79], 76 (<0.001,0.23)
	sub6	92 [91,94], 93 (0.39,0.05)	70 [54,79], 77 (0.002,0.33)	77 [69,82], 79 (<0.001,0.25)	79 [75,82], 80 (<0.001,0.17)
	sub7	94 [93,95], 95 (0.22,0.07)	89 [81,93], 91 (<0.001,0.2)	87 [81,90], 89 (<0.001,20)	83 [82,84], 83 (0.02,0.04)
	sub8	93 [85,96], 95 (0.004,0.19)	86 [83,88], 89 (0.03,0.12)	89 [87,90], 89 (<0.001,0.09)	73 [66,78], 76 (<0.001,0.25)
	Mean ± SD (ICC, r)	(85.63 ± 14.07, 91.63 ± 7.17)	(77.75 ± 11.95, 80.38 ± 11.88)	(86.5 ± 5.45, 88 ± 4.9)	(77.75 ± 5.63, 79 ± 4.28)

Table A.3. Subject by subject abs (bias) and (Var.) of R2*, QSM and T1 maps in voxel-wise analysis

qMR map	Metric	Bias, Var., (lb,ub)	Bias, Var., (lb,ub)	Bias, Var., (lb,ub)	Bias, Var., (lb,ub)
	ROI	Ca.	Pu.	lh-WM	lh-GM
R2* [1/s]	sub1	3.01, 10.11, (-2.05,8.06)	0.17, 5.83, (-2.75,3.08)	1.19, 13.63, (-5.62,8.01)	0.93, 21.14, (-9.64,11.5)
	sub2	0.33,14.53, (-6.94,7.59)	1.14, 8.53, (-3.13,5.4)	-0.99, 14.09, (-8.08,6.01)	-0.42, 18.94, (-9.89,9.05)
	sub3	0.64, 9.44, (-4.1,5.34)	0.8, 6.91, (-2.66,4.25)	1.24, 11.91, (-4.71,7.2)	0.44, 19.11, (-9.11,10)
	sub4	-1.67, 9.78, (-6.56,3.22)	-3.14, 13.12, (-9.7,3.42)	-0.56, 14.25, (-7.68,6.57)	-0.01, 22.02, (-11.02,11)
	sub5	0.59, 18.98, (-8.9,10.08)	1.43, 11.39, (-4.26,7.13)	2.52, 20.5, (-7.73,12.77)	0.31, 23.19, (-11.28,11.91)
	sub6	-0.2, 38.66, (-19.53,19.13)	-0.1, 25.59, (-12.9,12.69)	2.54, 30.36, (-12.64,17.72)	0.75, 34.78, (-16.64,18.14)
	sub7	-1.12, 9.97, (-6.11,3.86)	-0.96, 6.56, (-4.24,2.32)	-0.43, 9.51, (-5.18,4.33)	-0.08, 14.39, (-7.28,7.11)
	sub8	-0.12, 5.94, (-3.09,2.85)	0.22, 3.72, (-1.64,2.08)	-0.07, 13.1, (-6.62,6.48)	-0.11, 16.39, (-8.29,8.1)
	Mean ± SD abs (Bias), Var.	0.96 ± 0.97, 14.68 ± 10.45	1 ± 1, 10.21 ± 6.92	1.19 ± 0.92, 15.92 ± 6.61	0.38 ± 0.33, 21.25 ± 6.19
QSM [ppb]	sub1	8.6, 32.6, (-7.7,24.9)	3, 15.6, (-4.8,10.8)	-0.5, 17, (-9,8)	1.1, 26.3, (-12.1,14.2)
	sub2	1.5, 33.5, (-15.2,18.3)	0.1, 8.1, (-4,4.1)	1.6, 22.5, (-9.6,12.9)	1, 36.1, (-17.1,19)
	sub3	2.6, 14, (-4.4,9.6)	1.8, 5.7, (-1.1,4.6)	0.8, 16.3, (-7.3,9)	0.8, 25.1, (-11.8,13.3)
	sub4	2, 16.3, (-10.1,6.2)	0.2, 8.3, (-4.4,3.9)	-0.5, 21.1, (-11.1,10)	-0.3, 28, (-14.3,13.7)
	sub5	1.3, 24.4, (-13.5,10.9)	0.2, 8.6, (-4.5,4.1)	-0.8, 17.7, (-9.7,8)	-1, 39.8, (-20.9,18.9)
	sub6	5.4, 38, (-13.6,24.4)	2.5, 15.7, (-5.4,10.3)	2.2, 34.1, (-14.9,19.2)	1.8, 49.2, (-22.8,26.4)
	sub7	2.1, 17.1, (-6.4,10.7)	3.7, 11.5, (-2,9.5)	1.9, 13.1, (-4.7,8.4)	1.6, 19.6, (-8.2,11.4)
	sub8	1.4, 19.5, (-8.4,11.1)	1.3, 6.8, (-2.1,4.7)	0.8, 12.2, (-5.3,6.9)	1, 18.9, (-8.4,10.5)
	Mean ± SD abs (Bias), Var.	0.18 ± 1.4, 14.68 ± 10.45	1.6 ± 1.39, 10.04 ± 3.84	0.69 ± 1.17, 19.25 ± 6.95	0.75 ± 0.94, 30.38 ± 10.51

Table A.3-continued.

qMR map	Metric	Bias, Var., (lb,ub)	Bias, Var., (lb,ub)	Bias, Var., (lb,ub)	Bias, Var., (lb,ub)
	ROI	Ca.	Pu.	lh-WM	lh-GM
T1 [ms]	sub1	-28.01, 316.53, (-186.28,130.25)	15.29, 135.05, (-52.23,82.82)	28.55, 324.55, (-133.73,190.82)	20.96, 926.81, (-442.45,484.36)
	sub2	111.6, 377.96, (-300.58,77.38)	29.86, 309.86, (-125.07,184.79)	-43.79, 560, (-323.79,236.21)	114.41, 1189.44, (-709.13,480.31)
	sub3	-86.02, 522.66, (-347.35,175.31)	19.21, 366.36, (-163.97,202.39)	30.85, 334.76, (-136.53,198.23)	23.73, 807.47, (-380.01,427.46)
	sub4	47.94, 400.8, (-152.46,248.34)	-16.86, 258.2, (-145.96,112.24)	18.30, 262.65, (-113.02,149.63)	-5.13, 719.25, (-364.76,354.49)
	sub5	242.25, 891.54, (-688.02,203.52)	-13.34, 254.9, (-140.79,114.11)	21.29, 545.16, (-251.29,293.87)	-94.80, 1118.16, (-653.88,464.28)
	sub6	17.33, 526.48, (-245.91,280.57)	-35.37, 310.46, (-190.6,119.86)	56.22, 564.17, (-225.87,338.30)	62.94, 937.06, (-405.59,531.47)
	sub7	-15.35, 287.38, (-159.04,128.34)	25.56, 210.53, (-79.7,130.83)	35.82, 341.32, (-134.84,206.48)	-14.23, 827.16, (-427.81,399.35)
	sub8	-58.41, 409.32, (-263.07,146.25)	-17.66, 295.89, (-165.6,130.29)	21.11, 425.88, (-191.83,234.05)	-92.25, 1040.75, (-612.63,428.12)
	Mean±SD abs (Bias), Var.	(75.86±75.14, 466.58±191.76)	(21.64±7.79, 267.66±70.97)	(31.99±12.95, 419.81±121.54)	(53.56±42.82, 945.76±161.71)

Table A.4. Subject-level (pairwise) CV% of the average qMR values in ROI-based analysis and the mean over all subjects.

qMR map	Sub.	ROI			
		Ca.	Pu.	lh-WM	lh-GM
T1	sub1	1.24	0.87	1.8	0.91
	sub2	4.63	1.43	2.64	1.45
	sub3	3.77	1.02	2.13	1.09
	sub4	1.94	0.81	1.12	0.21
	sub5	9.13	0.74	1.29	4.15
	sub6	0.71	2.06	3.4	2.59
	sub7	0.69	1.27	2.34	0.6
	sub8	2.37	0.84	1.28	3.71
	Mean	3.06	1.13	2	2.21
R2*	sub1	5.24	0.33	2.31	2.09
	sub2	0.63	2.02	1.97	1.02
	sub3	1.32	1.52	2.3	1.01
	sub4	3.37	6.4	1.16	0.02
	sub5	1.1	2.13	4.57	0.66
	sub6	0.34	0.15	4.42	1.56
	sub7	2.02	1.65	0.79	0.19
	sub8	0.24	0.4	0.13	0.26
	Mean	1.78	1.83	2.21	0.85
QSM	sub1	18.85	26	2.4	9.87
	sub2	69.84	49.49	27.31	60.96
	sub3	33.12	31.67	15.93	26.05
	sub4	96.33	17.15	7.41	15.2
	sub5	40.47	8.35	13.38	54.76
	sub6	96.5	47.56	44.86	118.15
	sub7	1.67	74.18	102.6	51.66
	sub8	14.15	12.02	23.71	108.05
	Mean	46.37	33.3	29.65	55.59

Table A.4-continued. (CV %)

qMR map	Sub.	ROI
		WM.
F	sub1	7.31
	sub2	0.51
	sub3	2.64
	sub4	1.66
	sub5	1.76
	sub6	3.64
	sub7	0.22
	sub8	0.65
	Mean	2.3
MWF	sub1	8.24
	sub2	1.44
	sub3	8.14
	sub4	5.1
	sub5	11.48
	sub6	6.89
	sub7	8.19
	sub8	2.15
	Mean	6.45